CHALMERS
UNIVERSITY OF TECHNOLOGY

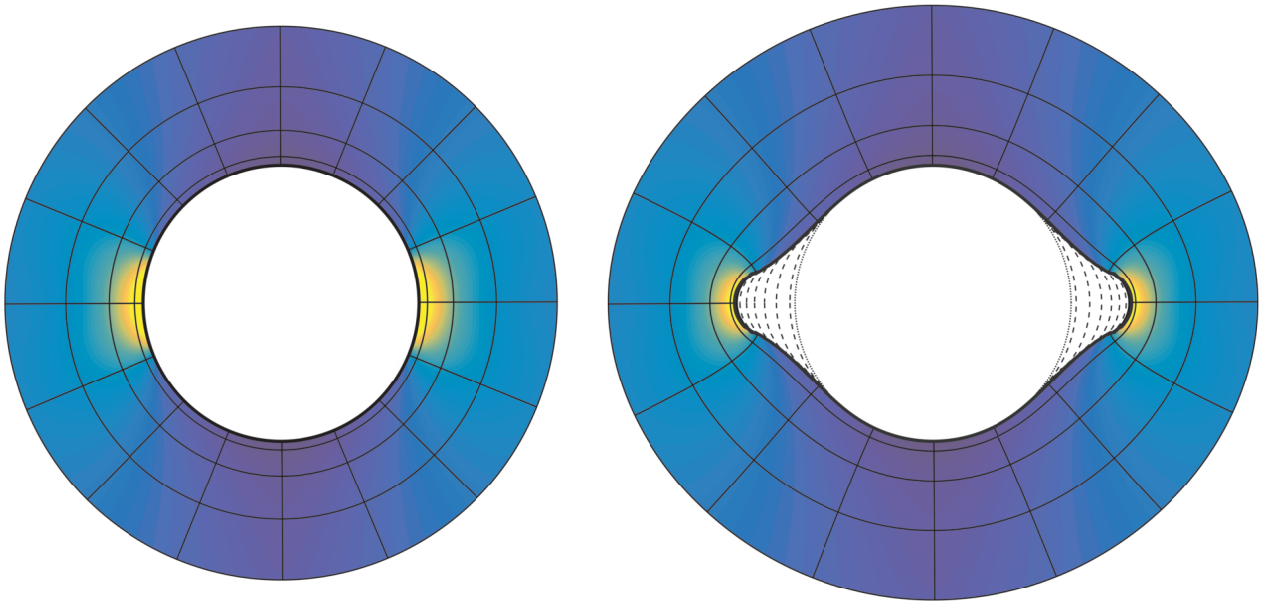

Borehole stability in brittle rock

A tool for evaluation of borehole breakouts and in-situ stress

Master's thesis in Infrastructure and Environmental Engineering

NILS-ERIK FELLDIN

Department of Architecture and Civil Engineering
Division of Geology and Geotechnics
Engineering Geology and Geotechnics
CHALMERS UNIVERSITY OF TECHNOLOGY
Gothenburg, Sweden 2019
Master's thesis ACEX30-19-113

MASTER'S THESIS ACEX30-19-113

Borehole stability in brittle rock

A tool for evaluation of borehole breakouts and in-situ stress

Master's thesis in Infrastructure and Environmental Engineering

NILS-ERIK FELLDIN

Department of Architecture and Civil Engineering
Division of Geology and Geotechnics
Engineering Geology and Geotechnics
CHALMERS UNIVERSITY OF TECHNOLOGY

Gothenburg, Sweden 2019

Borehole stability in brittle rock
A tool for evaluation of borehole breakouts and in-situ stress
NILS-ERIK FELLDIN

Master's thesis ACEX30-19-113
Department of Architecture and Civil Engineering
Division of Geology and Geotechnics
Engineering Geology and Geotechnics
Chalmers University of Technology
SE-412 96 Gothenburg
Sweden
Telephone: +46 (0)31-772 1000

Colophon:
The thesis was created using LaTeX 2_ε and `biblatex`. It was edited on `www.overleaf.com`. The text is set in Times New Roman. Graphs were created using MATLAB®. Figures were created using Ti*k*Z and INKSCAPE.

Cover:
Major principal stresses surrounding a simulated borehole with breakouts, represented in both the reference domain and problem domain. A grid around the exterior of a unit circle in the reference domain and its conformal mapping counterpart in the problem domain are overlaid the stresses. A few steps of the breakout progression are shown with dashed lines.

Chalmers Reproservice
Gothenburg, Sweden 2019

Borehole stability in brittle rock
A tool for evaluation of borehole breakouts and in-situ stress
Master's thesis in Infrastructure and Environmental Engineering
NILS-ERIK FELLDIN
Department of Architecture and Civil Engineering
Division of Geology and Geotechnics
Engineering Geology and Geotechnics
Chalmers University of Technology

ABSTRACT

This thesis deals with the simulation of progressive failures in boreholes, a phenomenon known as borehole breakouts. Borehole breakouts or spalling are common in holes and tunnels subject to large differential in-situ stresses. The aim was to produce a simulation tool in MATLAB using a conformal mapping method based on the work of Gerolymatou (2019).

An interactive graphical tool was coded to design a geometry and to evaluate its conformal mapping from a unit circle. A script was coded for determining stress distributions and checking for rock failure with the Mohr-Couloumb and Hoek-Brown failure criterion. Using this script it was also possible to iterate failure and generate new boundaries for simulating borehole breakouts.

By using the designed tool example mappings of several geometries are shown in an attempt to quantify the performance of the mapping method. The secondary stress state of a circular hole was compared to the Kirsch (1898) solution and the stresses around a tunnel geometry was compared to a MATLAB Finite Element Model (FEM). Finally, results of a few borehole breakout simulations are presented.

The mapping was shown to perform best for geometries defined by smooth continuous curves. The method of determining secondary stresses around symmetric regions is functional, however the FEM comparison of an asymmetric tunnel geometry demonstrated that the code needs further adaptation to correctly evaluate stresses around arbitrary geometries. Simulations of progressive borehole breakouts are possible if dealing with boundary oscillations stemming from the mapping. Oscillations are handled by using filters smoothing the boundary and optionally by also smoothing secondary stresses. A few ideas are presented on how the smoothing implementation can be improved to increase performance of breakout simulation.

As an example of how breakout simulation can be used to find in-situ stresses from measured real world breakouts, breakout depth and width from simulations are shown as functions of the in-situ stress. Such functions could potentially be used to match measured real world breakouts to the maximum in-situ stress, if the minor in-situ stress is determined by a method such as hydraulic fracturing and if the rock can be accurately modelled by a failure criterion.

Keywords: Borehole breakouts, Conformal mapping

CONTENTS

Abstract i

Contents iii

Preface xi

Nomenclature xiii

1 Introduction 1
1.1 Background . . . 1
1.2 Aim . . . 3
1.3 Limitations . . . 3
1.4 Method . . . 3

2 Theory 5
2.1 Stress states . . . 5
2.1.1 Primary stress . . . 6
2.1.2 Secondary stress . . . 10
2.1.3 Pore pressure gradients and operational stresses . . . 13
2.2 Brittle and ductile failure . . . 14
2.3 Failure criteria . . . 15
2.4 Borehole breakouts . . . 19
2.4.1 Measuring of breakouts . . . 20
2.4.2 Stress estimation from borehole breakouts . . . 22
2.5 Conformal mapping . . . 24

3 The computational tool 29
3.1 Evaluating mapping . . . 29
3.1.1 Defining a geometry . . . 31
3.1.2 Centering the geometry . . . 32
3.1.3 Sampling a polygon . . . 33
3.1.4 Geometry, sampling and mapping GUI-tool . . . 33
3.2 Evaluating the stress function . . . 36
3.3 From in-situ stress to borehole breakouts . . . 36
3.3.1 Sampling, mapping and region discretization . . . 38
3.3.2 Stresses and stress surface smoothing . . . 39
3.3.3 Defining a new boundary . . . 40
3.3.4 Boundary smoothing . . . 41

4 Examples 43
4.1 Mapping examples . . . 43

4.1.1 Mapped geometries . . . 43
4.1.2 Effect of corners . . . 55
4.1.3 Effect of number of series terms . . . 57
4.1.4 Effect of number of samples . . . 58
4.2 Stress function examples . . . 61
4.2.1 Borehole comparison to the Kirsch solution . . . 61
4.2.2 Asymmetric tunnel comparison to finite element analysis . . . 63
4.3 In-situ stress to borehole breakouts . . . 68
4.3.1 Tensile breakouts . . . 68
4.3.2 Shear breakouts . . . 71
4.3.3 Depth and width of example breakouts . . . 72

5 Discussion **75**
5.1 Defining a cavity geometry and mapping it . . . 75
5.2 Evaluating secondary stresses . . . 76
5.3 Simulating breakouts and the use of smoothing . . . 76
5.4 Designing an inverse model for finding in-situ stress from measured breakouts . . . 78

6 Conclusion **79**

References **81**

Appendix A Complex numbers **85**

List of Figures

2.1 A stress state described in two different coordinate bases. (a) Stresses described in the normal $x - y$ coordinate system. (b) Same stresses described in a coordinate system $x' - y'$, in this system the stresses are called principal. In the principal stress state all shear components are zero. 5

2.2 Graphical representation of Young's modulus on a stress σ vs. strain ε curve for a material. Youngs's modulus E is the slope of the curve as $E = d\sigma/d\varepsilon$. 7

2.3 Uniaxial compression on a sample resulting in strain in two directions. By measuring the strains the Poisson's ratio of a material can be calculated. 8

2.4 Orientation of the borehole local coordinate system $x - y - z$ defined through azimuth direction ϕ_a and dip angle γ_d from the global coordinate system $N - E - H$. On a map the borehole is heading in the direction of ϕ_a and has a slope angle of γ_d measured from the horizon. A negative slope angle is down. 9

2.5 Overview of variables used in the Kirsch secondary stress solution. (a) The borehole radius is a, the internal/support pressure p_0. In-situ normal stresses σ_{xx}, σ_{yy} and in-situ shear stress τ_{xy}. The secondary stress solution is calculated at a point measured at an angle θ and radius r from the origin. (b) Complement to the $x - y$ view showing out of plane in-situ stresses surrounding the borehole. Except those stresses shown in the $x - y$ plane there are a normal stress σ_{zz} in addition to τ_{xz} and τ_{yz} which are shear stresses. . 11

2.6 Tractions at a point along the boundary described in two different ways. (a) Normal stress σ and tangential shear stress τ acting on the boundary. The boundary normal is oriented at an angle α from the Ox-axis. (b) Internal support pressure p_0 acting normal to the boundary surface is broken up into two vector components for traction stresses f_x and f_y. The vectors are parallel to the x and y axes respectively. 12

2.7 Example of initial and equilibrium pore pressure gradients surrounding a borehole when the pore pressure is lower than the pressure of the drilling fluids. The borehole is outlined on the r scale. Pressure inside the borehole with a radius of a is p_0 and the formation pore pressure is p_f. The steady state pore pressure distribution is shown as $p(r)$. As r increases $p(r) \rightarrow p_f$. 14

2.8 Example of simplified ductile and brittle material behaviour in a stress, σ vs. strain ε, curve, drawn after Stüwe (2011). 15

2.9 Mohr-Couloumb failure envelope $\tau_f = f_{\text{MC}}(\sigma'_n)$ with a stress state represented through a Mohr's circle based on the minimum and maximum effective principal stresses σ'_3 and σ'_1. The failure envelope is defined by a cohesion constant c and a friction angle ϕ. Stress normal to the failure plane is σ'_n, the normal stress results in a shear stress τ. By comparing the stress τ to τ_f as in Equation (2.34) rock failure can be evaluated. 16

2.10 Mohr-Couloumb failure envelope with tension and compaction cutoff stresses implemented. Stress states drawn as Mohr's circles that fit within the green region will not fail according to this model. The linear part f_{MC} is the original Mohr-Coulomb criterion. The arcs near the tension cutoff σ_t and compaction cutoff p_c stem from the fact that no Mohr's circle can be drawn so that it is positioned outside of the arcs without first causing either a shear failure by passing f_{MC} or a tensile/compaction failure due to exceeding the cutoffs σ_t or p_c. 17
2.11 Hoek-Brown Failure criterion shown in plots of minor σ_3 and major σ_1 principal stresses. A certain stress state in this type of plot is represented as a single point in the plane. (a) The original Hoek-Brown criterion as a function $f_{\text{HB}}(\sigma_3)$. (b) The Hoek-Brown criterion with tension σ_t and compaction p_c cutoffs added. Rock with a stress state within the green region will not fail. 18
2.12 Breakouts in a granite. Drawing created after a photo from an experimental study by Haimson (2007). 19
2.13 Drawings of progressive borehole breakouts forming. Drawing created after photos and sketches by Zoback et al. (2003). 20
2.14 Breakout formed by compaction bands in a sandstone with high porosity. Drawing created after a photo by Haimson and Kovacich (2002). 21
2.15 Shear fractures surrounding a borehole as a result of hydrostatic loading. Drawing created after a photo from an experimental study by Meier, Rybacki, Reinicke, and Dresen (2013). 21
2.16 Major σ_1 and minor σ_3 principal secondary stresses around a borehole. The borehole is subject to an anisotropic in-situ stress state. The two in-situ stresses are related by a factor of 5 as $\sigma_H = 5 \cdot \sigma_h$, where $\sigma_H = 50$ MPa. In the direction of σ_H an area of tension occurs on the borehole wall whilst an increase of compressive stresses occurs in the direction of σ_h. 23
2.17 Visualization of the direction of shear, tensile and compaction failure zones for a circular hole subject to anisotropic in-situ stresses. The zones were determined on a borehole with in-situ stresses related as $\sigma_h/\sigma_H = 0.3$, rock properties for the failure criterion's were chosen arbitrarily. Sub-figure (a) shows a case of shear failure with Mohr-Coulomb's criterion and a tensile failure. Sub-figure (b) displays compaction failure. 24
2.18 The problem is defined in the w plane and is then translated into a simpler geometry in the z plane. In the simple reference domain z the problem is solved and the solution can then be mapped back onto the original problem geometry in w. 25
3.1 The unit circle in the reference domain and an arbitrary region in the problem domain. The varying radius of the arbitrary region is described as a function $r(\gamma)$ of the argument angle γ. In the reference domain the unit circle is described by the argument θ and a fixed radius of 1. 30
3.2 A curved segment of the geometry with the radius r_k between the two polygon vertex points (x_k, y_k) and (x_{k+1}, y_{k+1}). 31
3.3 A circular borehole in the problem domain sampled at 16 points with an equal angular interval $d\gamma$. 33
3.4 A snapshot of the boundary and mapping test tool, showing the geometry design tab. . 34

3.5 The boundary and mapping test tool showing the "sampling and mapping" tab. A boundary is sampled at 128 points, samples are notated by red marks around the boundary geometry. The geometry is centered with its centroid at the origin. By pressing the "Calculate mapping" button in the lower right corner a mapping of the sampled boundary using 100 series terms are evaluated. 34
3.6 The mapping results overview tab, showing the sampled section displayed with a thick black line and the mapped one in a thinner red line. Below, the residual/error is shown in a polar style plot to visualize where the largest oscillations of the mapped boundary are located. To the right, sampling and mapping settings are displayed together with mapping time, residual norm and residual mean. 35
3.7 The last tab, Residuals, showing the residuals along the boundary in more detail. . . . 35
3.8 Flowchart for determining borehole breakouts from in-situ stress. 37
3.9 Example of discretization using 32 angular nodes times 8 radial nodes in the reference domain (a), with its corresponding mapped discretization in the problem domain (b). During an actual simulation, the node density is much larger than shown in this example. 38
3.10 Breakouts generated without smoothing are shown in (a) and breakouts generated with boundary and stress smoothing enabled shown in (b). 39
3.11 Boundary stresses at iteration 10 for an angular segment of the boundary, highlighting stresses before and after stress surface smoothing using 64 angular samples and 32 radial. Mesh was set to 2048 nodes in the angular direction and 1024 in the radial. 40
3.12 Example of how the R_{cont} used in the smoothing is constructed. In this example $N = 5$ and the boundary is made up of 16 nodes. 41
4.1 Mapping of an equilateral triangle. 44
4.2 Residuals $e(\gamma)$ for the mapping of an equilateral triangle. 45
4.3 Mapping of an rectangle. 46
4.4 Residuals $e(\gamma)$ for the mapping of an rectangle. 47
4.5 Mapping of a shaft with smooth corners. 48
4.6 Residuals $e(\gamma)$ for the mapping of a smooth shaft. 49
4.7 Mapping of an asymmetric tunnel. 50
4.8 Residuals $e(\gamma)$ for the mapping of a asymmetric tunnel. 51
4.9 A geometry of a borehole with breakouts generated from a photo by Haimson (2007). The green dots mark polygon vertices obtained from the photo and the red line shows the boundary of the geometry used in the mapping. 52
4.10 Mapping of a measured borehole with breakouts. 53
4.11 Residuals $e(\gamma)$ for the mapping of a measured borehole with breakouts. 54
4.12 Four straight lines and two circle segments making up a smooth geometry with the exception of two corners with angles α. As α increases towards 180 degrees the geometry looks more and more like a normal circle. 55
4.13 Mapping the test geometry with two 15 degree corners returned a visibly distorted result. 56
4.14 Corner angles versus maximum and mean error. 56

4.15 Number of series terms versus maximum and mean error. The differences between different number of samples are very small, especially so between 1024 and 4096 samples which make them hard to distinguish between in this Figure. For the Max error in (a), 4096 samples has the largest error at start but the smallest at the end, whilst 256 samples has the lowest error at start and the largest error at the end. For the Mean error in (b), 4096 samples has the lowest mean error throughout the range of series terms and 256 samples the highest mean error. 57
4.16 Number of series terms versus mapping time. 58
4.17 Number of samples versus maximum and mean error. 59
4.18 Number of samples versus mapping time. 59
4.19 Stresses around a borehole with the medium settings. 60
4.20 Direction of principal stresses around borehole. 60
4.21 Comparing "Low" setting mapping solution to Kirsch for stresses around a circular borehole. 61
4.22 Comparing "Medium" setting mapping solution to Kirsch for stresses around a circular borehole. 62
4.23 Comparing "High" setting mapping solution to Kirsch for stresses around a circular borehole. 62
4.24 Stresses surrounding asymmetric tunnel "Low" settings 64
4.25 Direction of principal stresses surrounding the asymmetric tunnel using the "Low" mapping settings. 64
4.26 Conceptual setup of the finite element model. The length L was set to 160 times the maximum sampled boundary radius. 65
4.27 Comparing the Kirsch solution to the FEA for stresses around a circular borehole. . . . 65
4.28 Comparing conformal mapping solution with "Low" mapping settings to the FEM for principal stresses around a asymmetric tunnel. 66
4.29 Comparing conformal mapping solution with high mapping settings to the FEM for principal stresses around a asymmetric tunnel. 66
4.30 Comparing major principal boundary stress between the FEM, "Low" and "High" conformal mapping solutions. The y-axis is cropped to make small oscillations more visible. 67
4.31 Comparing minor principal boundary stress between the FEM, "Low" and "High" conformal mapping solutions. The y-axis is cropped to make small oscillations more visible. 67
4.32 Again comparing the conformal mapping solution with "High" mapping settings to the FEM for principal stresses around a asymmetric tunnel. This time the mapped boundary instead of the sampled is used in the FEM model. 68
4.33 Breakout progressions with the Mohr-Coulomb failure criterion, using a varying major in-situ stress σ_H whilst holding the minor in-situ stress fixed at $\sigma_h = 10$ MPa. 69
4.34 Breakout progressions with the Hoek-Brown failure criterion, using a varying major in-situ stress σ_H whilst holding the minor in-situ stress fixed at $\sigma_h = 10$ MPa. 70
4.35 Breakout progressions with the Mohr-Coulomb failure criterion, using a varying major in-situ stress σ_H whilst holding the minor in-situ stress fixed at $\sigma_h = 20$ MPa. 71
4.36 Breakout progressions with the Hoek-Brown failure criterion, using a varying major in-situ stress σ_H whilst holding the minor in-situ stress fixed at $\sigma_h = 20$ MPa. 72

4.37 Tensile breakout depth (a) and width (b), using the Mohr-Coulomb failure criterion with tensile cutoff. The minor in-situ stress was fixed at $\sigma_h = 10$ MPa whilst varying the major in-situ stress σ_H. 73
4.38 Tensile breakout depth (a) and width (b), using the Hoek-Brown failure criterion with tensile cutoff. The minor in-situ stress was fixed at $\sigma_h = 10$ MPa whilst varying the major in-situ stress σ_H. 73
4.39 Shear breakout depth (a) and width (b), using the Mohr-Coulomb failure criterion. The minor in-situ stress was fixed at $\sigma_h = 20$ MPa whilst varying the major in-situ stress σ_H. 74
4.40 Shear breakout depth (a) and width (b), using the Hoek-Brown failure criterion. The minor in-situ stress was fixed at $\sigma_h = 20$ MPa whilst varying the major in-situ stress σ_H. 74
A.1 Representation of complex number in 2D. 85

List of Tables

4.1 Summarized mapping test results for a equilateral triangle. 45
4.2 Summarized mapping test results for a rectangle. 47
4.3 Summarized mapping test results for a smooth shaft. 49
4.4 Summarized mapping test results for a asymmetric tunnel. 51
4.5 Summarized mapping test results for a measured borehole with breakouts. 54
4.6 Table showing mapping statistics for different corner angles. Mapping was evaluated with 100 coefficients and 1024 samples. 55

PREFACE

Since I first started my studies at Chalmers University of Technology my goal was set at specializing in rock. In this project I saw an opportunity to do just that and also evolve many of the skills acquired during my years at Chalmers. My interest was especially peaked by the chance of deepening my abilities in MATLAB.

The project consisted of working with a method of conformal mapping unitized by my examiner and supervisor Eleni Gerolymatou, and based on her work design an easy to use tool that could provide a simple and fast method of estimating the stress state around boreholes and tunnels.

I would like to thank Eleni Gerolymatou for excellent guidance and support. I am grateful for the opportunity of working with her conformal mapping method. My effort on this thesis has been arduous, which is why I would also like to thank my friends and family for their moral support throughout the project.

Gothenburg, September 16, 2019

Nils-Erik Felldin

Nomenclature

Greek letters

α	Boundary normal angle
β	Biot's constant
$\boldsymbol{\sigma}_r$	Radial secondary stress tensor
γ	w-plane argument angle
γ_d	Dip angle
λ	Ratio between horizontal/vertical in-situ stress
μ	Dynamic viscosity
ν	Poisson's ratio
ν_i	Rock grain Poisson's ratio
ϕ	Rock friction angle
ϕ_a	Azimuth angle
ρ	Density bulk
ρ_w	Density water
σ	Stress
σ_1	Major principal stress
σ_1'	Effective major principal stress
σ_2	Intermediate principal stress
σ_3	Minor principal stress
σ_3'	Effective minor principal stress
σ_B	Borehole in-situ stress tensor
σ_G	Global in-situ stress tensor
σ_H	Major horizontal in-situ stress
σ_h	Minor horizontal in-situ stress
σ_n'	Effective normal stress
σ_t	Tension cut off stress
σ_v	Vertical in-situ stress
$\sigma_{\theta\theta}$	Hoop stress component
σ_{ci}	Hoek-Brown unconfined compressive strength
$\sigma_{r\theta}$	r-θ plane shear stress component
σ_{rr}	Radial stress component
σ_{xx}	x-direction stress component
σ_{yy}	y-direction stress component
σ_{zz}	z-direction stress component
σ_z	z-direction stress component
τ	Shear Stress
τ_f	Shear stress failure limit
$\tau_{\theta z}$	θ-z plane shear stress component
τ_{hv}	In-situ shear stress component
$\tau_{r\theta}$	r-θ plane shear stress component
τ_{rz}	r-z plane shear stress component
τ_{xy}	x-y plane shear stress component
τ_{xz}	x-z plane shear stress component
τ_{yz}	y-z plane shear stress component
θ	Kirsch and complex z-plane argument angle
ε	Strain
ε_x	Strain in x direction
ε_y	Strain in y direction

Roman lower case letters

a	Hole radius
a_n	Goursat derivative series constants
b_n	Goursat derivative series constants
c	Rock cohesion
c_n	Fourier series coefficients
c_x	Arc center x-coordinate
c_y	Arc center y-coordinate
d	Distance
d_0	Initial distance
f_x	Traction component boundary
f_y	Traction component boundary
$f_{s,k}$	Sampled boundary point
g	Gravitational acceleration constant
i	Complex value ($\sqrt{-1}$) or index
j	Index
k	Permeability
l	Length
l_0	Initial length
m	Index
m_i	Hoek-Brown material constant
n	Index
n_f	Number of series terms
n_s	Number of samples
p	Pressure
p_0	Support pressure
p_c	Compressive cutoff stress
p_f	Formation pore pressure
p_m	Mapping series real part of coefficient

q	Fluid flow
q_m	Mapping series coefficient
q_n	Conformal mapping series constants
r	Radial distance
r_k	Arc segment radius
s_m	Mapping series imaginary part of coefficient
t_a	Arc parametrization start angle
t_b	Arc parametrization end angle
w	Problem domain complex number
x', y', z'	Principal stress coordinate axes
x, y, z	Coordinate axes
x_k	Vertex x-coordinate
y_k	Vertex y-coordinate
z	Reference domain complex number
z_d	Depth
z_w	Water depth
z_{dist}	Size of reference domain to use during mapping

Functions

$\chi(w)$	Goursat function
$\chi_r(z)$	Reference domain Goursat function
$\omega(w)$	Conformal mapping
$\phi(w)$	Goursat function
$\phi_r(z)$	Reference domain Goursat function
$\sigma_H(z)$	Horizontal in-situ stress estimate
$\sigma_r(r, \theta)$	Kirsch secondary stresses in radial coordinates
$\sigma_v(z)$	Vertical in-situ stress estimate
$e(\gamma)$	Boundary residual error from mapping
$f(z)$	Inverse conformal mapping
$f_{\mathrm{HB}}(\sigma_3)$	Hoek-Brown failure criterion
$f_{\mathrm{MC}}(\sigma'_n)$	Mohr-Coulomb failure criterion
$g(\theta)$	Squared boundary magnitude expressed in reference domain argument
$p(r)$	Radial pore pressure distribution
$r(\gamma)$	Boundary magnitude
$U(w)$	Stress function

Roman capital letters

$\hat{X}, \hat{Y}$	Polygon coordinates after translation
A	Polygon area
A_n	Goursat series constant
B_n	Goursat series constant
C_x	Polygon centroid x-coordinate
C_y	Polygon centroid y-coordinate
E	Young's modulus
E_h	Average horizontal Young's modulus of upper crust
E_i	Rock grain Young's modulus
F	Force
N	Number of moving average samples
N, E, H	Global coordinate base
P_1	Arc starting point
P_2	Arc ending point
R	Mapping constant/scale factor
R_b	Tensor transform matrix
R_{cont}	Boundary magnitude vector modified be continuous for the moving average filter
R_{mavg}	Boundary magnitude vector smoothed by moving average filter
X, Y	Polygon coordinates before translation

1 Introduction

Boreholes are drilled in rock for many different purposes, one of the first that might come to mind are the deep boreholes drilled to serve as oil wells. There are however many more uses for boreholes, for example, numerous homes are supplied with fresh water from wells drilled into the bedrock. Another borehole use for housings are geothermal heating wells, which is the most common type of geo-energy used for homes in Sweden (Erlström, Mellqvist, Schwarz, Gustafsson, & Dahlqvist, 2016). This is not only used on smaller properties but can also be applied to larger ones in a more industrial way. A recent example of such a project is mentioned in a trade magazine by Knutsson (2017), where the use of 135 drilled wells with a depth of ≈350 m supplies heating for 1100 apartments. Deep boreholes destined for nuclear byproduct storage are being investigated as a solution for a safe and long term solution to the problem (Odén, 2013). If also considering circular holes at a slightly larger scale, infrastructure tunnels drilled by massive tunnel boring machines can be included in the definition of boreholes. Tunnels can provide passage through difficult or precious terrain, be a means of mining minerals and even constitute the base of any underground facility. In conjunction to tunnels there might be raisebore shafts that either provide ventilation, a passage way of minerals for mines or as a water conduit in hydroelectric plants (Liu & Meng, 2015).

Some of the deepest holes are drilled for petroleum extraction, geothermal energy and nuclear waste storage. The stress in the bedrock before any construction, *in-situ stress*, increases with depth. It is common that the type of deep boreholes just mentioned is subject to high in-situ stresses. One of the problems with high in-situ stress is that the borehole walls can suffer brittle failure that progressively breaks loose pieces of rock until a stable geometry is achieved. This phenomenon that is known as borehole breakouts can cause many issues in the drilling process or in the future operation of the hole (Meng & Fuh, 2013).

The investment in deep boreholes can be costly both in time and money, which implies that delay due to technical difficulties from hole failures is an important aspect in the planning and construction process (Caenn, Darley, & Gray, 2017) (York et. al. 2009). If the extent of the failures can be modelled before excavation it can help in the design and construction of the structure. To be able to achieve a prediction of the extent of these failures, the in-situ stress state must be known or have a reasonable estimate. However, making these estimates is often difficult at larger depths (Odén, 2013). One possible way to identify the in-situ stress state is by analyzing borehole breakouts in existing holes (Brudy, Zoback, Fuchs, Rummel, & Baumgärtner, 1997).

This thesis deals with the modelling of progressive failure in boreholes and other cavities for prediction of breakout shape, breakout magnitude and secondary stress states. An attempt was also made to determine the largest of the in-situ stresses based on the shape of measured breakouts. The goal was to include these functions in a simple to use computational tool that could be of aid to engineers in the design and evaluation of boreholes and tunnels.

1.1 Background

From many borehole geometry measurements in Alberta and Texas made with mechanical 4-arm caliper probes Gough and Bell (1981) concluded that the borehole breakouts found likely was correlated to the regional stress state of the areas. Since then many studies have been performed to further increase the

understanding of how borehole breakouts form and what shape and orientation the breakout will take depending on rock type, material properties and the in-situ stress state. The connection to in-situ stress state is of interest due to its importance when planning for hole trajectories and choosing the drilling fluid density (Zoback et al., 2003). The drilling fluid, often referred to as mud, provides a support pressure that increases borehole stability. Choosing a proper density of the fluid is important not only for borehole stability but also for preventing fluids in the formation from entering the hole (Lake & Mitchell, 2006). As mentioned in the introductory part, there are many different applications to deep boreholes where this is applicable such as the petroleum industry, geothermal energy and nuclear waste depositories. How, why and when borehole breakouts are formed will be discussed more in depth under Section 2.4.

In the petroleum industry the Kirsch (1898) analytic solution for circular holes has often been the go-to solution when evaluating borehole stability. However, if the geometry is non-circular or when a borehole fails and a breakout forms, the Kirsch solution will not be applicable and engineers must resort to other methods of calculation (Aadnøy & Looyeh, 2010). A method that can be used when evaluating non-simple geometries is conformal mapping.

Conformal mapping is an angle preserving mathematical transformation that has been used in a wide range of engineering applications such as aerodynamics, vibrations, heat transfer, fluid flow and elasticity. Development of solutions to classical steady state problems, many defined by the Laplace equation, stems from the early 20th century (Kythe, 1998). The principle of conformal mapping is in short to map a difficult problem (by geometry or physical model) onto a domain in which the problem will be easier to solve. This method was especially useful before computers were available for calculating numerical solutions of non-simple geometries. Although finite element and finite difference methods have been favoured by the computational power of today, conformal mapping still has useful applications (Schinzinger & Laura, 1991).

In the domain of elasticity much of the conformal mapping methods originate from Russian mathematicians G.V. Kolosov and N.I. Muskhelishvili. The complex potential formula developed by the two has had great use in fracture mechanics when dealing with two-dimensional crack problems (Sun & Jin, 2012) although the method is also suitable for use on underground cavities such as tunnels or boreholes.

There are numerous modern examples where stress and displacements have been evaluated with the help of conformal mapping methods: Verruijt (1998) mapped a circular cavity in the elastic half plane onto a circular ring where a solution to elasticity problems could be evaluated; Zhou, Kong, and Liu (2016) found an elastic solution for an elliptical cavity with a uniform internal pressure by mapping it to the unit circle; Exadaktylos and Stavropoulou (2002) calculated stresses and displacement of a "D" shaped tunnel with the use of conformal mapping and verified the results with the numerical modelling software FLAC^{2D}.

For some of the practicalities involved with the implementation of numerical conformal mapping there has also been modern contributions such as an iterative method of Wegmann (1989) where he demonstrates the mapping of a unit disc onto regions with smooth boundaries. The mapping is simply achieved by making Fourier transforms in each iteration, which for near circular regions rapidly converges. Another numerical method for determining series coefficients was presented by Fornberg (1980). His method showed the mapping of the unit circle onto smooth curve boundaries with the help of fast Fourier transforms.

1.2 Aim

The aim of this project was to construct a simple to use computational tool based on conformal mapping for evaluation of boreholes and tunnels. The purpose of the tool was to aid in the prediction of shape and magnitude of borehole breakouts from a few given initial conditions such as in-situ stress, initial cavity geometry and the strength of the rock. Also, a solution for the inverse problem was to be explored so that information regarding the in-situ stress state could be obtained from measured borehole breakouts.

1.3 Limitations

During the design of the tool a few effects were not considered as listed below.

- Time dependency
- Thermal stresses
- Rock anisotropy
- Drilling/excavation induced damages to the rock

1.4 Method

The project begun with a literature study of various topics related to borehole breakouts, mainly on how and why breakouts form. It was relevant to find out how borehole breakouts currently are predicted and how their shape and orientations are measured for the estimation of in-situ stress. During this process studies containing experimental data regarding borehole breakouts were found, the idea was to later use the experimental studies as a comparison to breakout simulations. Many of the components that potentially could be included in the tool had to be investigated such as in-situ stress estimation and suitable failure criteria. Since it was decided that conformal mapping would be used for evaluating the stress distributions around the boreholes the subject was studied.

After the literature study the relevant required math was assembled and a schematic of the computational tool was drawn up to simplify the subsequent programming. Following the laid-out structure the tool was programmed in MATLAB with some of the mapping and stress functions provided by Gerolymatou (2019). When the code needed for computation was in place the different sub-parts: mapping, secondary stress evaluation and breakout simulation, were tested against several different input data. For geometry design and mapping, a Graphical User Interface (GUI) was programmed to simplify testing. To quantify mapping performance the mapped and original geometry was compared. The Kirsch (1898) solution for a circular hole was used to test if secondary stresses were evaluated correctly, additionally a Finite Element Model (FEM) was programmed to test if stresses were evaluated correctly around arbitrary cavity geometries. To stabilize the breakout simulations different implementations of boundary and stress smoothing was needed. After tweaking settings several breakout simulations were run and the width and depth of the breakout examples were obtained.

2 Theory

This chapter will cover some theory on borehole breakouts, borehole surveying methods and stress states. The mathematical groundwork surrounding conformal mapping and secondary stress calculations is also covered here before it is implemented in the next chapter. Since much of the math uses complex notation, Appendix A contains a brief overview on complex numbers for reference.

2.1 Stress states

In the design of any underground structure there are a few different stress states that are of interest for the analysis. The primary, secondary and operational or tertiary stress states will be introduced in this section along with methods of calculating or estimating them.

Stresses are measured in Pascals (Pa) and are defined as force in Newtons per unit area (Pa = N $\cdot$ m^{-2}). In a two dimensional case there are two stress components acting normal to a unit square and shear stresses acting along the square's border, see Figure 2.1a.

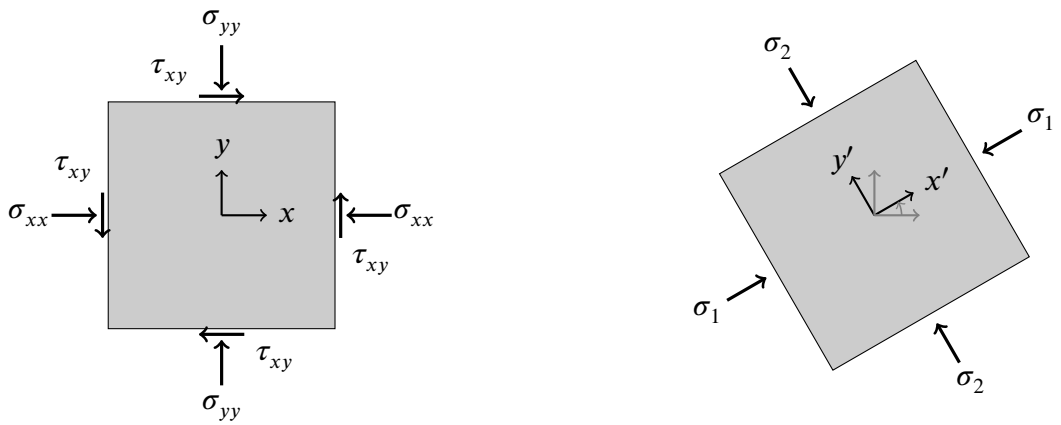

(a) A stress state.

(b) Principal stresses of case (a).

Figure 2.1: A stress state described in two different coordinate bases. (a) Stresses described in the normal $x - y$ coordinate system. (b) Same stresses described in a coordinate system $x' - y'$, in this system the stresses are called principal. In the principal stress state all shear components are zero.

In two dimensions as demonstrated in Figure 2.1a the stress at a certain location can be described with three individual components. For a three dimensional case the extra dimension results in a need of six different components in total. When describing stresses at a certain point in a three dimensional rock mass it is often represented as a stress tensor as shown in Equation (2.1).

$$\sigma = \begin{bmatrix} \sigma_{xx} & \tau_{xy} & \tau_{xz} \\ \tau_{xy} & \sigma_{yy} & \tau_{yz} \\ \tau_{xz} & \tau_{yz} & \sigma_{zz} \end{bmatrix} \tag{2.1}$$

By rotating the base of the coordinate system from which the stress components are measured, an orientation can be found in which there are no shear stresses. The tensor can then be represented through only three principal stresses σ_1, σ_2 and σ_3, see Figure 2.1b where the principle is shown for the two dimensional case. The largest of the principal stresses is denoted as σ_1 and the smallest as σ_3. In Equation (2.2) the principal stresses for a three dimensional case is shown in matrix form.

$$\sigma = \begin{bmatrix} \sigma_1 & 0 & 0 \\ 0 & \sigma_2 & 0 \\ 0 & 0 & \sigma_3 \end{bmatrix} \tag{2.2}$$

2.1.1 Primary stress

The primary stress state, also called the in-situ stress state, is before any excavation or alteration to the site has taken place. It is influenced by different factors such as topography, rock anisotropy, regional tectonics, rock density and major fractures (Ewy & Cook, 1990). Most often the vertical stress σ_{zz} is the largest due to the overburden of the rock. This in many cases makes it one of the principal stresses (Brudy et al., 1997). If then the coordinate system is rotated so that the horizontal axes aligns with the other two horizontal principal stresses it results in the principal stress tensor

$$\sigma = \begin{bmatrix} \sigma_H & 0 & 0 \\ 0 & \sigma_h & 0 \\ 0 & 0 & \sigma_v \end{bmatrix} \tag{2.3}$$

In this representation σ_H is the largest horizontal stress, σ_h the smallest horizontal stress and the vertical stress σ_v. When no major influencing factors such as large faults or regional tectonics are present it can be assumed that the stress state is transversely isotropic meaning $\sigma_H = \sigma_h$ (Maleki, Moradzadeh, Riabi, & Sadaghzadeh, 2014).

Estimating the primary stress state

The vertical stress σ_v can easily be estimated at different depths z_d from the surface by making use of the bulk density $\rho(z_d)$ of the rock mass as shown in Equation (2.4). In offshore applications Equation (2.5) can be used which also takes into account the effect of the water depth z_w and the water density ρ_w (Zoback et al., 2003). In a homogeneous rock mass the density of the rock can be assumed to be constant which leads to the simplification in Equation (2.4) (Aadnøy & Looyeh, 2010). However, in the offshore case of Equation (2.5) such simplifications are not recommended since rock and sand density at the bottom of the sea is low and then increases significantly with depth (Zoback et al., 2003).

$$\sigma_v(z_d) = g \int_0^{z_d} \rho(z_d) dz_d \approx g\rho z_d \tag{2.4}$$

$$\sigma_v(z_d) = g\rho_w z_w + g \int_{z_w}^{z_d} \rho(z_d) dz_d \tag{2.5}$$

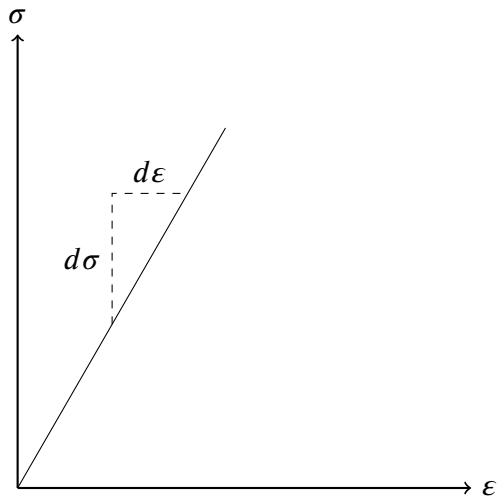

Figure 2.2: Graphical representation of Young's modulus on a stress σ vs. strain ε curve for a material. Youngs's modulus E is the slope of the curve as $E = d\sigma/d\varepsilon$.

Horizontal stresses are often not transversally isotropic in practice (Aadnøy & Looyeh, 2010) but it can serve as a first estimate to assume this. By using the ratio between horizontal and vertical stress λ and the Biot's constant β of the rock together with the vertical stress at a surface depth $\sigma_v(z_d)$ horizontal stresses $\sigma_H = \sigma_h$ can be estimated as shown in Equation (2.11) (Aadnøy & Looyeh, 2010).

Before the ratio λ and the Biot's constant is defined and used in estimating horizontal in-situ stresses the basic concept of strain, the Young's modulus and Poisson's ratio must be introduced. If a stress is applied to a material it will deform, the ratio between the deformation dl and the initial dimensions l_0 results in a dimensionless measure called strain denoted by ε, see Equation (2.6).

$$\varepsilon = \frac{l - l_0}{l_0} = \frac{dl}{l_0} \tag{2.6}$$

The Young's modulus E is a material parameter that defines the relationship between stress and strain in a material. It is calculated as shown in Equation (2.7), see Figure 2.2 for a graphical representation in a stress-strain curve.

$$E = \frac{\sigma}{\varepsilon} \tag{2.7}$$

The Poisson's ratio is a measure of how much a material deforms along two axes when applying uniaxial stress along one axis, see Equation (2.8) and Figure 2.3.

$$\nu = -\frac{\varepsilon_y}{\varepsilon_x} \tag{2.8}$$

The Biot's constant is a scaling factor of the pore pressure p_f and is calculated as shown in Equation (2.9). The Biot's constant is calculated from the elasticity modulus E and the Poisson's ratio of the bulk rock mass and from the same parameters E_i and ν_i of the rock grains in between the pore spaces. In most common rock the Biot's constant is between 0.8-1 (Aadnøy & Looyeh, 2010).

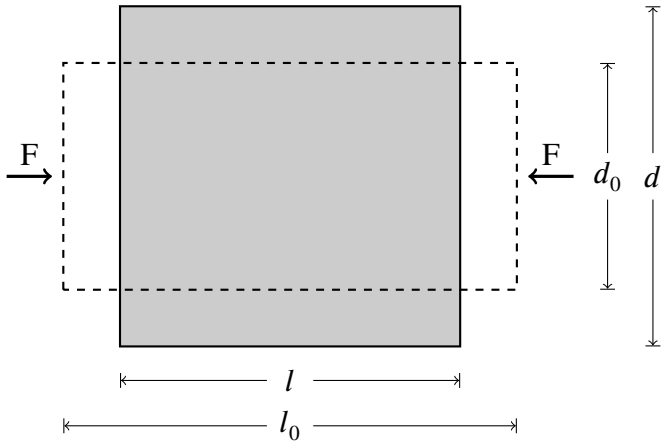

Figure 2.3: Uniaxial compression on a sample resulting in strain in two directions. By measuring the strains the Poisson's ratio of a material can be calculated.

$$\beta = 1 - \frac{E}{E_i}\frac{1-2\nu_i}{1-2\nu} \tag{2.9}$$

The ratio between horizontal and vertical stress λ can be modelled in several ways. A simple method by Terzhagi and Richart that assumes perfect elasticity was previously widely used but since it underestimates λ at shallow depths it is not as commonly used today. Another model by Sheorey was proposed in 1994 which better approximates λ (Hoek, n.d.). In the Sheorey model E_h is the average Young's modulus of the upper parts of the crust measured in the horizontal direction. Both the Terzhagi-Richart and Sheorey models are shown in Equation (2.10).

$$\lambda = \begin{cases} \frac{\nu}{1-\nu} & \text{Terzaghi and Richart (1952)} \\ 0.25 + 7E_h\left(0.001 + \frac{1}{z_d}\right) & \text{Sheorey (1994)} \end{cases} \tag{2.10}$$

Horizontal stresses can then be estimated through the following equation

$$\sigma_H(z_d) = \sigma_h(z_d) = \lambda\left(\sigma_v(z_d) - \beta p_f\right) + \beta p_f \tag{2.11}$$

Primary stress state transform for deviated boreholes

When describing the geometry and calculating stresses around a borehole or a tunnel, a local coordinate system that is aligned to the cavity can be used for simplicity. For vertical boreholes or shafts the global in-situ stress tensor will be aligned to the local coordinate system, in practice this is often not the case which calls for a method of transforming the global in-situ stresses so that they are expressed in terms of the local coordinate system of the cavity.

Let the in-situ stresses in the global coordinate system $X - Y - Z$ (alternatively North-East-Height) be defined as

$$\sigma_G = \begin{bmatrix} \sigma_X & \tau_{XY} & \tau_{XZ} \\ \tau_{XY} & \sigma_Y & \tau_{YZ} \\ \tau_{XZ} & \tau_{YZ} & \sigma_Z \end{bmatrix} \tag{2.12}$$

If the previously described simplified stress state is used or if the principal stresses are aligned to the global coordinate system the global stress tensor will become

$$\sigma_G = \begin{bmatrix} \sigma_H & 0 & 0 \\ 0 & \sigma_h & 0 \\ 0 & 0 & \sigma_v \end{bmatrix} \tag{2.13}$$

The borehole has an azimuth direction ϕ_a in the horizontal plane and an angle of dip γ_d in the vertical plane as shown in Figure 2.4. The transformation matrix R_b will be a function of the azimuth and dip , see Equation (2.14).

$$R_b = \begin{bmatrix} \cos\phi_a \cos\gamma_d & \sin\phi_a & \cos\phi_a \sin\gamma_d \\ \sin\phi_a \cos\gamma_d & -\cos\phi_a & \sin\phi_a \sin\gamma_d \\ \sin\gamma_d & 0 & -\cos\gamma_d \end{bmatrix} \tag{2.14}$$

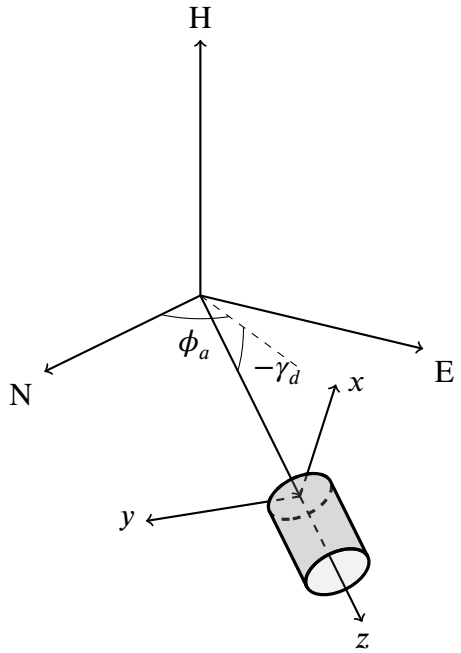

Figure 2.4: Orientation of the borehole local coordinate system $x - y - z$ defined through azimuth direction ϕ_a and dip angle γ_d from the global coordinate system $N - E - H$. On a map the borehole is heading in the direction of ϕ_a and has a slope angle of γ_d measured from the horizon. A negative slope angle is down.

In-situ stresses σ_b expressed in the local cavity coordinate system $x-y-z$ can then be found with the transformation matrix

$$\sigma_b = \begin{bmatrix} \sigma_{xx} & \tau_{xy} & \tau_{xz} \\ \tau_{xy} & \sigma_{yy} & \tau_{yz} \\ \tau_{xz} & \tau_{yz} & \sigma_{zz} \end{bmatrix} = R_b^T \sigma_G R_b \tag{2.15}$$

The components of the in-situ stress tensor σ_b is used in Section 2.1.2 when evaluating secondary stresses.

2.1.2 Secondary stress

When drilling or excavation takes place the stress state in the rock changes to accommodate the cavity which cannot transfer stress. The new stress state is called secondary stress. For boreholes, and any geometry that has the same 2D section along its extent, a plane strain assumption can be used during secondary stress calculations. The plane strain assumption means that along the extent of the z-axis, strain is assumed to be equal to zero. Below two different methods of calculating the secondary stress state for plane elasticity problems are shown. The first one by Kirsch (1898) is for strictly circular geometries and the second method by Airy (1862) can be used on general regions.

Kirsch solution for circular holes

For a circular opening Kirsch (1898) found a solution for the stress distribution analytically by using a special case of the theory of Airy. Kirsch's solution with a plane strain assumption expressed in radial coordinates $\boldsymbol{\sigma}_r = f(r,\theta)$ is shown in Equations (2.16) to (2.21) (Aadnøy & Looyeh, 2010). The solution uses the in-situ stress components in the plane of the hole as σ_{xx}, σ_{yy} and τ_{xy}. Along the hole axis components σ_{zz}, τ_{xz} and τ_{yz} are used as input. Internal pressure (from water or other support) is denoted p_0 and the hole radius is a, see Figure 2.5.

$$\sigma_{rr} = \frac{1}{2}(\sigma_{xx}+\sigma_{yy})\left(1-\frac{a^2}{r^2}\right) + \frac{1}{2}(\sigma_{xx}-\sigma_{yy})\left(1+3\frac{a^4}{r^4}-4\frac{a^2}{r^2}\right)\cos 2\theta + \tau_{xy}\left(1+3\frac{a^4}{r^4}-4\frac{a^2}{r^2}\right)\sin 2\theta + p_0\frac{a^2}{r^2} \tag{2.16}$$

$$\sigma_{\theta\theta} = \frac{1}{2}(\sigma_{xx}+\sigma_{yy})\left(1+\frac{a^2}{r^2}\right) - \frac{1}{2}(\sigma_{xx}-\sigma_{yy})\left(1+3\frac{a^4}{r^4}\right)\cos 2\theta - \tau_{xy}\left(1+3\frac{a^4}{r^4}\right)\sin 2\theta - p_0\frac{a^2}{r^2} \tag{2.17}$$

$$\sigma_z = \sigma_{zz} - 2\nu(\sigma_{xx}-\sigma_{yy})\frac{a^2}{r^2}\cos 2\theta - 4\nu\tau_{xy}\frac{a^2}{r^2}\sin 2\theta \tag{2.18}$$

$$\tau_{r\theta} = \left[\frac{1}{2}(\sigma_{xx}-\sigma_{yy})\sin 2\theta + \tau_{xy}\cos 2\theta\right]\left(1-3\frac{a^4}{r^4}+2\frac{a^2}{r^2}\right) \tag{2.19}$$

$$\tau_{rz} = (\tau_{xy}\cos\theta + \tau_{yz}\sin\theta)\left(1-\frac{a^2}{r^2}\right) \tag{2.20}$$

$$\tau_{\theta z} = (-\tau_{xz}\sin\theta + \tau_{yz}\cos\theta)\left(1+\frac{a^2}{r^2}\right) \tag{2.21}$$

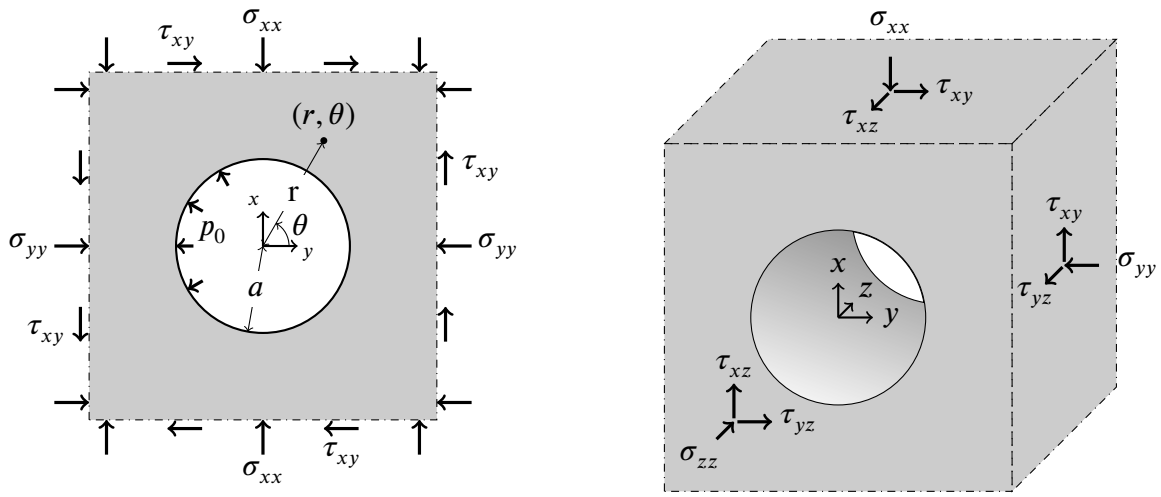

(a) Front view of $x - y$ plane.

(b) Perspective view of 3D in-situ stresses around the borehole.

Figure 2.5: Overview of variables used in the Kirsch secondary stress solution. (a) The borehole radius is a, the internal/support pressure p_0. In-situ normal stresses σ_{xx}, σ_{yy} and in-situ shear stress τ_{xy}. The secondary stress solution is calculated at a point measured at an angle θ and radius r from the origin. (b) Complement to the $x - y$ view showing out of plane in-situ stresses surrounding the borehole. Except those stresses shown in the $x - y$ plane there are a normal stress σ_{zz} in addition to τ_{xz} and τ_{yz} which are shear stresses.

Airy stress function in the complex plane

It was found by Airy (1862) that in plane elasticity problems, stresses can be expressed by a function U as shown in Equation (2.22).

$$\sigma_{xx} = \frac{\partial^2 U}{\partial y^2}, \qquad \sigma_{yy} = \frac{\partial^2 U}{\partial x^2}, \qquad \sigma_{xy} = -\frac{\partial^2 U}{\partial x \partial y} \tag{2.22}$$

For plane stress the function U is the solution to the fourth order partial differential Equation (2.23) which is called the biharmonic equation.

$$\nabla^4 U = \frac{\partial^4 U}{\partial x^4} + 2\frac{\partial^4 U}{\partial x^2 \partial y^2} + \frac{\partial^4 U}{\partial y^4} = 0 \tag{2.23}$$

Once a solution to the biharmonic equation is found the stresses can be calculated.

Goursat (1898) (Schinzinger & Laura, 1991) showed that a solution to the biharmonic equation can be found by the help of two complex analytic functions $\phi(w)$ and $\chi(w)$. The solution is shown in Equation (2.24).

$$U(x, y) = U(w) = \Re[\overline{w}\phi(w) + \chi(w)] \tag{2.24}$$

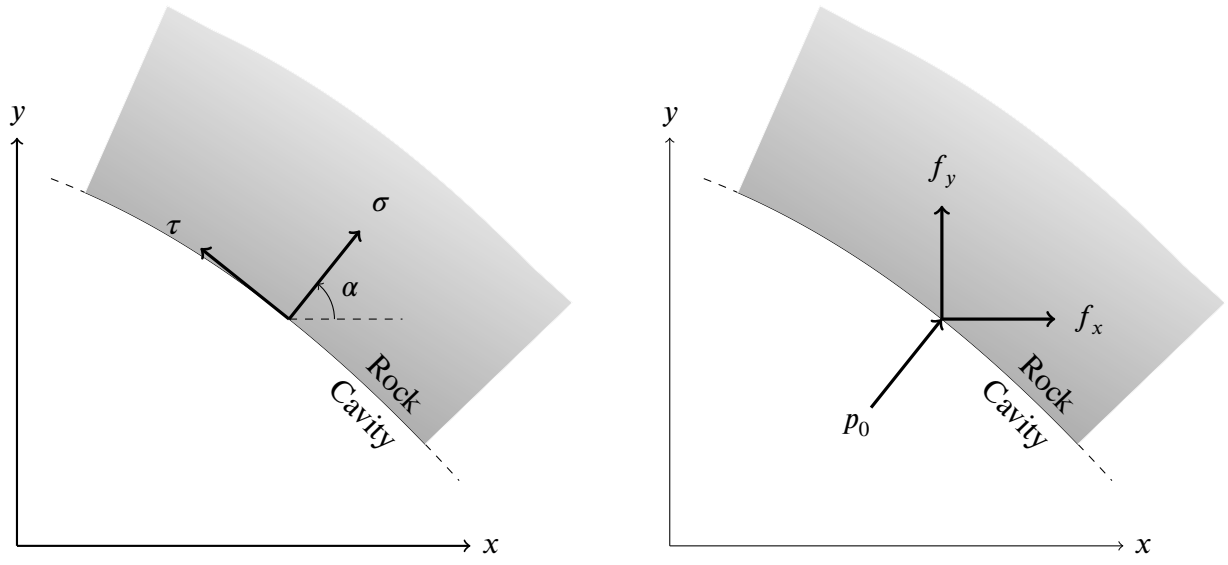

Figure 2.6: Tractions at a point along the boundary described in two different ways. (a) Normal stress σ and tangential shear stress τ acting on the boundary. The boundary normal is oriented at an angle α from the Ox-axis. (b) Internal support pressure p_0 acting normal to the boundary surface is broken up into two vector components for traction stresses f_x and f_y. The vectors are parallel to the x and y axes respectively.

Determining the functions ϕ and χ is accomplished by evaluating the boundary conditions at infinity and at the interior boundary. At the far field boundaries at infinity, in-situ stress is prevalent. For the interior boundary L the tractions can be expressed as

$$\sigma - i\tau = 2\Re[\phi'(w)] - e^{2i\alpha}[\overline{w}\phi'(w) + \chi(w)] \tag{2.25}$$

where σ are the tractions normal to the boundary and τ tangential to the boundary. The angle α is the angle of the boundary normal to the Ox axis, see Figure 2.6a.

The boundary tractions along the x and y axes can be denoted as f_x and f_y. For a boundary element of length ds the forces acting on the element will be the integral

$$i\int f_x + if_y ds$$

In the case of a uniform internal pressure p_0, it can be shown that the the resulting force on the boundary element equals

$$i\int f_x + if_y ds = p_0 w \tag{2.26}$$

When Equation (2.26) is combined with the derivative of Equation (2.24) which corresponds to forces, the following result is obtained

$$\phi(w) + w\overline{\phi'(w)} + \overline{\chi'(w)} = p_0 w \tag{2.27}$$

From the definition of the Airy stress function in Equation (2.22) and its solution in Equation (2.24) a few different stress relations can be found which are helpful when determining the Goursat's functions from the boundary conditions. These relations are shown in Equation (2.28).

$$\begin{aligned} \sigma_{xx} + \sigma_{yy} &= 4\Re[\phi'(w)] \\ \sigma_{yy} - \sigma_{xx} + 2i\sigma_{xy} &= 2[\overline{w}\phi''(w) + \chi'(w)] \end{aligned} \tag{2.28}$$

And in radial coordinates as

$$\sigma_{\theta\theta} - \sigma_{rr} + 2i\sigma_{r\theta} = [\sigma_{yy} - \sigma_{xx} + 2i\sigma_{xy}]e^{2i\theta} \tag{2.29}$$

When the geometry of the problem is simple this solution is straightforward to implement. However, this is often not the case. A method used to overcome the difficulties with complicated geometries is conformal mapping where the problem is transformed into a simpler geometry as shown in Section 2.5.

2.1.3 Pore pressure gradients and operational stresses

In sedimentary rock the pore water pressure p_f is the fluid pressure inside the pores of the rock formation (Aadnøy & Looyeh, 2010). At shallow depths and in rock with an open permeable pore system the pressure is often hydrostatic which is called a normal formation pressure. If the pore structure has a low permeability or if the rock is contained under a impermeable layer such as dense clay the pore water pressure can increase above hydrostatic. A pore pressure above hydrostatic is achieved by the lithostatic pressure and the ocean pressure driving a pore volume decrease of the underlying rock. Since the low permeability does not allow water to flow out of the formation fast enough the pore pressure rises. Formations like these are called geopressured, or abnormaly pressured, and typically consist of shales or rock contained by surrounding shale (Caenn et al., 2017).

An increased pore water pressure in a rock drastically reduces its strength (Waltham, 2009) and if the pressure inside the borehole p_0 is lower than the pore pressure, the pressure gradient can lead to fluid flow from the formation into the borehole. Such a flow can cause wellbore instability (Caenn et al., 2017). To prevent this problem the mud weight is chosen to provide a well pressure larger than the pore pressure to keep the flow gradient from the hole outward into the formation. Mud weight must however not be so large that it causes a new set of problems by fracturing the rock.

When the hole is first drilled, the pressure difference Δp between the borehole and its wall will be as shown in Equation (2.30).

$$\Delta p = p_0 - p_f \tag{2.30}$$

After some time the pore pressure surrounding the borehole will decrease or increase to equilibrium depending on the sign of Δp, creating a gradient over some distance into the surrounding rock, see Figure 2.7. This steady state pressure curve can be calculated for a circular hole according to Equation (2.31) (Caenn et al., 2017).

$$p(r) = \frac{\mu q}{2\pi k} \ln \frac{r}{2a} \tag{2.31}$$

Where the dynamic viscosity of the fluid is denoted μ, the fluid flow per unit of wellbore length q, the formation permeability k and the radius of the borehole a (Caenn et al., 2017).

During operation of a well the solution to the pressure distribution around the borehole will be transient depending on the rock permeability and the viscosity of the fluid.

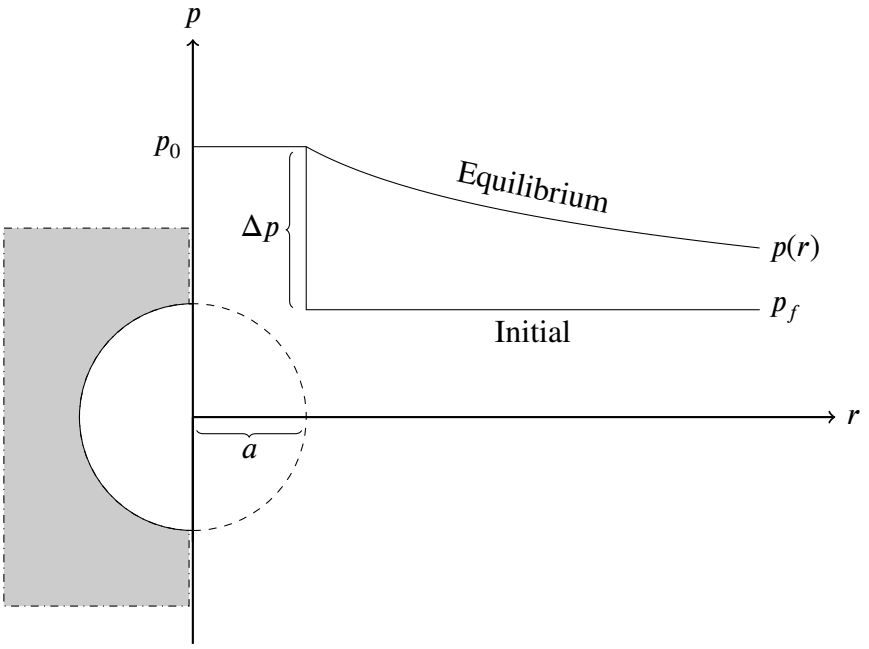

Figure 2.7: Example of initial and equilibrium pore pressure gradients surrounding a borehole when the pore pressure is lower than the pressure of the drilling fluids. The borehole is outlined on the r scale. Pressure inside the borehole with a radius of a is p_0 and the formation pore pressure is p_f. The steady state pore pressure distribution is shown as $p(r)$. As r increases $p(r) \rightarrow p_f$.

2.2 Brittle and ductile failure

The simplest way to demonstrate brittle behaviour is through breaking glass, when it breaks it shatters to pieces. Ductile behaviour on the other hand can be demonstrated by a dough, when stress is applied to it it will deform and change its shape. A brittle rock will, when it reaches its limiting strength, fracture and break whilst a ductile rock will yield and allow for more deformation before ultimately reaching failure (Marshak, 2011). In Figure 2.8 a simplified stress strain model for a brittle and ductile rock is shown.

If a material deforms in a brittle or ductile manner is partly a property of the material but it is also dependent of the temperature, pressure and rate of deformation. Low temperatures, low pressures and fast sudden deformations encourage brittle behaviour while the opposites encourage ductile behaviour. Rock typically behaves brittle from the surface down to depths of 10-15 km and ductile beyond those

depths. The reason for this is that pressure and temperature in the earth's lithosphere increase with increasing depth (Marshak, 2011).

Even though rock typically would behave ductile at depth the introduction of an opening by a borehole can allow the rock to fail in a brittle manner near the hole at depths where ductile deformation would be expected (Caenn et al., 2017).

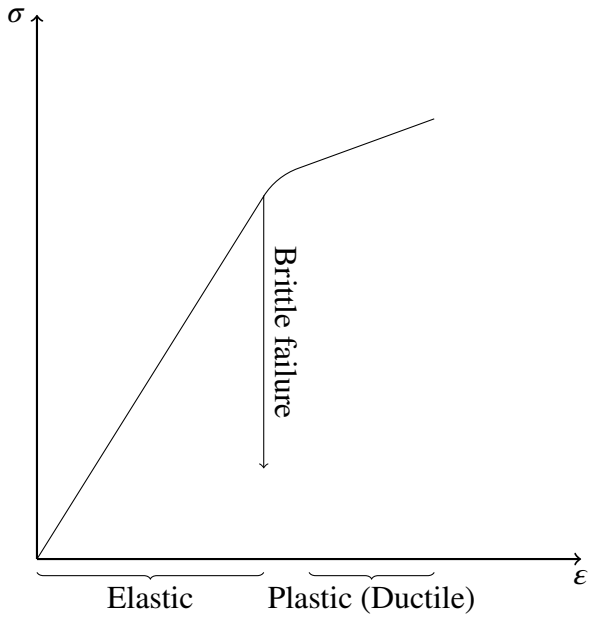

Figure 2.8: Example of simplified ductile and brittle material behaviour in a stress, σ vs. strain ε, curve, drawn after Stüwe (2011).

2.3 Failure criteria

Whether a certain stress state acting upon the rock will cause failure can be modelled with the help of failure criteria. A vast amount of different criteria which are suitable for different types of materials and failure mechanisms exist. Two failure criteria commonly used with rock, the Mohr-Couloumb and the Hoek-Brown, are described in this section.

Mohr-Couloumb

The Mohr-Coulomb failure criterion (MC) is a method that can be used for evaluating brittle shear failures in rock by using the largest and smallest of the principal stresses σ_1 and σ_3 acting on the rock. The method was created by combining the two older failure criteria of Mohr (1900) and Coulomb (1776), however it is not evident who was the first one to utilize this method (Holtz & Kovacs, 1981). The MC is commonly used as a failure criterion even though it underestimates rock strength (Aadnøy & Looyeh, 2010).

Equation (2.32) describes the shear strength of a material depending on a cohesion constant c, the internal friction angle ϕ and the effective normal stress σ'_n (Stüwe, 2011). The material constants can be

determined through triaxial tests of rock core samples (Waltham, 2009).

$$\tau_f = f_{\text{MC}}(\sigma'_n) = c + \sigma'_n \tan\phi \tag{2.32}$$

By use of Mohr's circle the effective stress normal to the failure surface and the accompanying shear stress can be calculated with Equation (2.33). A graphical representation is shown in Figure 2.9.

$$\begin{aligned} \tau &= \frac{1}{2}(\sigma_1 - \sigma_3)\cos\phi \\ \sigma'_n &= \frac{1}{2}(\sigma_1 + \sigma_3) - \frac{1}{2}(\sigma_1 - \sigma_3)\sin\phi - p_f \end{aligned} \tag{2.33}$$

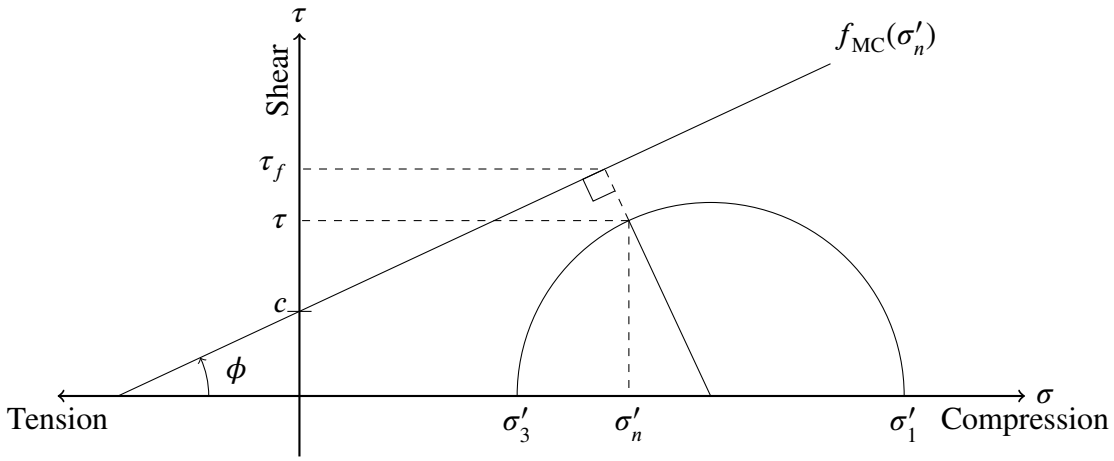

Figure 2.9: Mohr-Couloumb failure envelope $\tau_f = f_{\text{MC}}(\sigma'_n)$ with a stress state represented through a Mohr's circle based on the minimum and maximum effective principal stresses σ'_3 and σ'_1. The failure envelope is defined by a cohesion constant c and a friction angle ϕ. Stress normal to the failure plane is σ'_n, the normal stress results in a shear stress τ. By comparing the stress τ to τ_f as in Equation (2.34) rock failure can be evaluated.

Shear failure can then be controlled against Equation (2.34).

$$\begin{cases} f_{\text{MC}}(\sigma'_n) > \tau, & \text{No shear failure} \\ f_{\text{MC}}(\sigma'_n) \leq \tau, & \text{Shear failure} \end{cases} \tag{2.34}$$

Generally, the failure mode for rock is through shear (Waltham, 2009) but care must be taken when applying the MC if other failure mechanisms are possible (Aadnøy & Looyeh, 2010). To remedy this, tensile and compressive cutoffs on allowed principal stresses can be added which are based on the material's tensile and compressive strength. The use of a tensile cutoff stress σ_t with the MC was first made by Paul (1961, 2) and the implementation is simply that a tensile failure is reached if the minimal principal stress is tensile and larger than the cutoff σ_t. Compaction failure is assumed to occur when the largest principal stress reaches a limit p_c in compression. The MC failure envelope with tensile and

compaction cutoffs included is shown in Figure 2.10. In Equation (2.35) the tensile failure condition is shown and in Equation (2.36) the compaction failure condition is shown. Note that the definition of σ_3 in Equation (2.35) is that negative stress corresponds to tension.

$$\begin{cases} \sigma_3 > \sigma_t, & \text{No tensile failure} \\ \sigma_3 \leq \sigma_t, & \text{Tensile failure} \end{cases} \tag{2.35}$$

$$\begin{cases} p_c > \sigma_1, & \text{No compaction failure} \\ p_c \leq \sigma_1, & \text{Compaction failure} \end{cases} \tag{2.36}$$

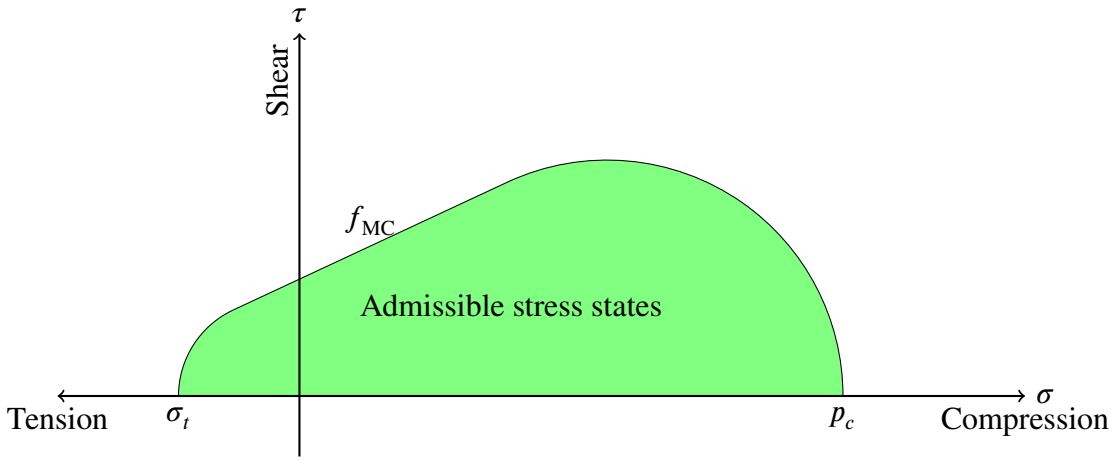

Figure 2.10: Mohr-Couloumb failure envelope with tension and compaction cutoff stresses implemented. Stress states drawn as Mohr's circles that fit within the green region will not fail according to this model. The linear part f_{MC} is the original Mohr-Coulomb criterion. The arcs near the tension cutoff σ_t and compaction cutoff p_c stem from the fact that no Mohr's circle can be drawn so that it is positioned outside of the arcs without first causing either a shear failure by passing f_{MC} or a tensile/compaction failure due to exceeding the cutoffs σ_t or p_c.

Hoek-Brown

The Hoek-Brown is an empirical criterion modelled to fit experimentally observed shear failures. It was devised by E. Hoek and E.T. Brown in 1980 as a method of designing underground excavations (Hoek & Martin, 2014). The criterion models brittle failure reasonably well but is not suitable for modelling ductile failure (Aadnøy & Looyeh, 2010). The criterion has also been expanded resulting in the *Generalized Hoek-Brown criterion* that better matches different rock masses, but since it requires additional inputs only the simpler original criterion for intact rock is used in this work. In Equation (2.37) the criterion is shown, it depends on the unconfined compressive strength σ_{ci} and a material constant m_i, both of which can be determined through triaxial tests.

$$\sigma_1 = f_{\text{HB}}(\sigma_3) = \sigma_3 + \sigma_{ci}\sqrt{m_i \frac{\sigma_3}{\sigma_{ci}} + 1} \tag{2.37}$$

Failure with the Hoek-Brown criterion can be checked against the following

$$\begin{cases} f_{\mathrm{HB}}(\sigma_3) > \sigma_1, & \text{No shear failure} \\ f_{\mathrm{HB}}(\sigma_3) \leq \sigma_1, & \text{Shear failure} \end{cases} \tag{2.38}$$

During the time Hoek and Brown developed the method there was little interest in tensile failures, for the most part tensile strength was assumed to be zero (Hoek & Martin, 2014). Since tensile strength generally is overestimated in Hoek-Brown criterion a tensile cutoff is used in more recent implementations of the criterion. The tensile cutoff is determined from the constants σ_{ci} and m_i, see Equation (2.39) (Hoek, n.d.).

$$\sigma_t = -\frac{\sigma_{ci}}{m_i} \tag{2.39}$$

Whether tensile failure will occur or not can be controlled in Equation (2.35) using σ_t of Equation (2.39). An example of the criterion without the tensile cutoff included is presented graphically in Figure 2.11a.

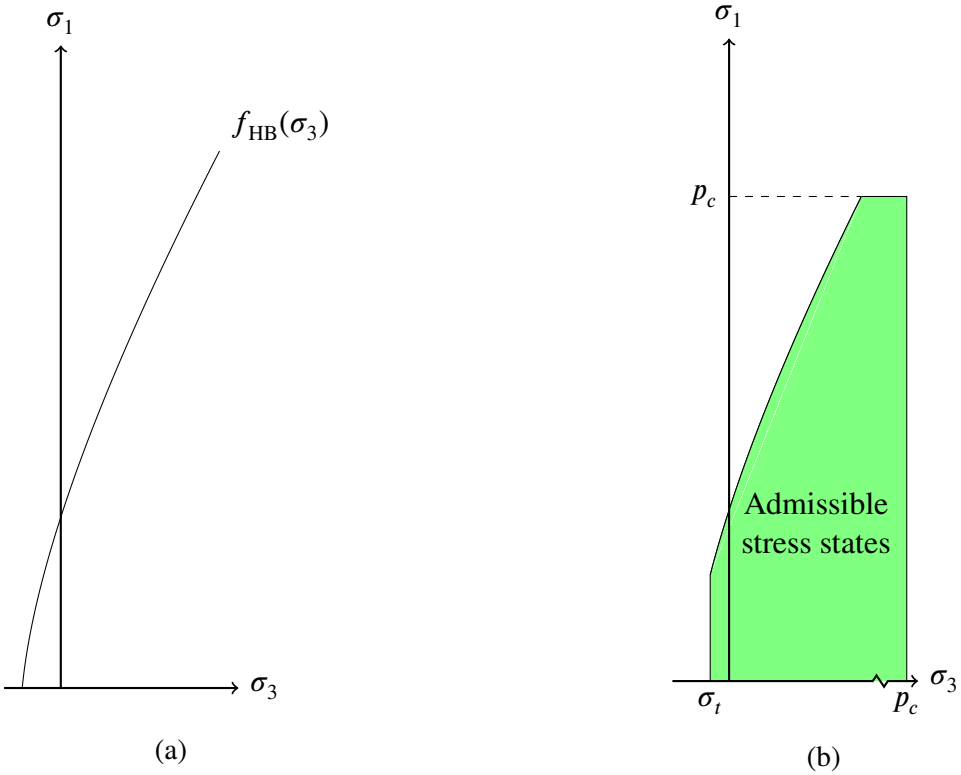

Figure 2.11: Hoek-Brown Failure criterion shown in plots of minor σ_3 and major σ_1 principal stresses. A certain stress state in this type of plot is represented as a single point in the plane. (a) The original Hoek-Brown criterion as a function $f_{\mathrm{HB}}(\sigma_3)$. (b) The Hoek-Brown criterion with tension σ_t and compaction p_c cutoffs added. Rock with a stress state within the green region will not fail.

Due to the fact that the Hoek-Brown was designed to handle shear failures, the criterion does not reflect upon compaction failure. To also take into account this type of failure a limit on maximum compressive stress p_c can be used, see Equation (2.36).

2.4 Borehole breakouts

Borehole breakouts, or spalling in tunnels, is a phenomenon where the cavity breaks apart into a geometry in which the rock strength is sufficient to bear the in-situ stress surrounding it. The main prerequisite for the formation of aligned breakouts is horizontal stresses of considerable unequal magnitude acting on the cavity (Gough & Bell, 1981). If the stresses are sufficient for the rock to fail, breakouts will form in the direction of minimum principal stress as seen in Figure 2.12. Drilling induced tensile fractures may also form in the direction of the maximum horizontal stress but will be small in the range of milli- to centimetres (Zoback et al., 2003). Breakouts form progressively over a period of time, a schematic of this is shown in Figure 2.13.

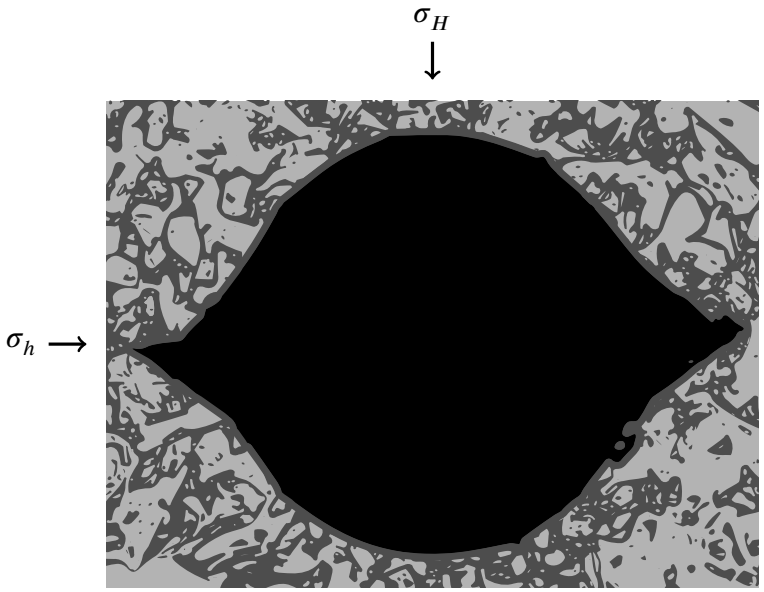

Figure 2.12: Breakouts in a granite. Drawing created after a photo from an experimental study by Haimson (2007).

The ratio between the horizontal stresses determines the magnitude of the breakout for vertical boreholes. If the difference between lithostatic pressure and hydrostatic pressure decreases, the required ratio between the horizontal stresses needed for breakout will be lower (U.S. National Committee for Rock Mechanics, Geotechnical Board, and National Research Council, 1993). The vertical stress acting along the hole axis is believed to have little effect on the formation of breakouts. This conclusion was drawn during experiments on breakouts in the rock Lac du Bonnet granite by Lee and Haimson (1993).

The size and geometry of the hole/cavity also plays a role in its resilience against failure. Several studies have noted that a small hole diameter requires higher stresses for breakouts to form (U.S. National Committee for Rock Mechanics, Geotechnical Board, and National Research Council, 1993) (Cuss, Rutter, & Holloway, 2003). If the cavity is excavated to the shape of what would have otherwise been formed by breakouts or spalling it is suggested that it would be inherently stable with little need for support (Ewy & Cook, 1990) (Ewy, Kemeny, Zheng, & Cook, 1987).

The process of failure and the resulting breakout shape differs between rock and rock class. In granite the process starts inside the borehole wall with densely spaced extensile cracks forming almost normal

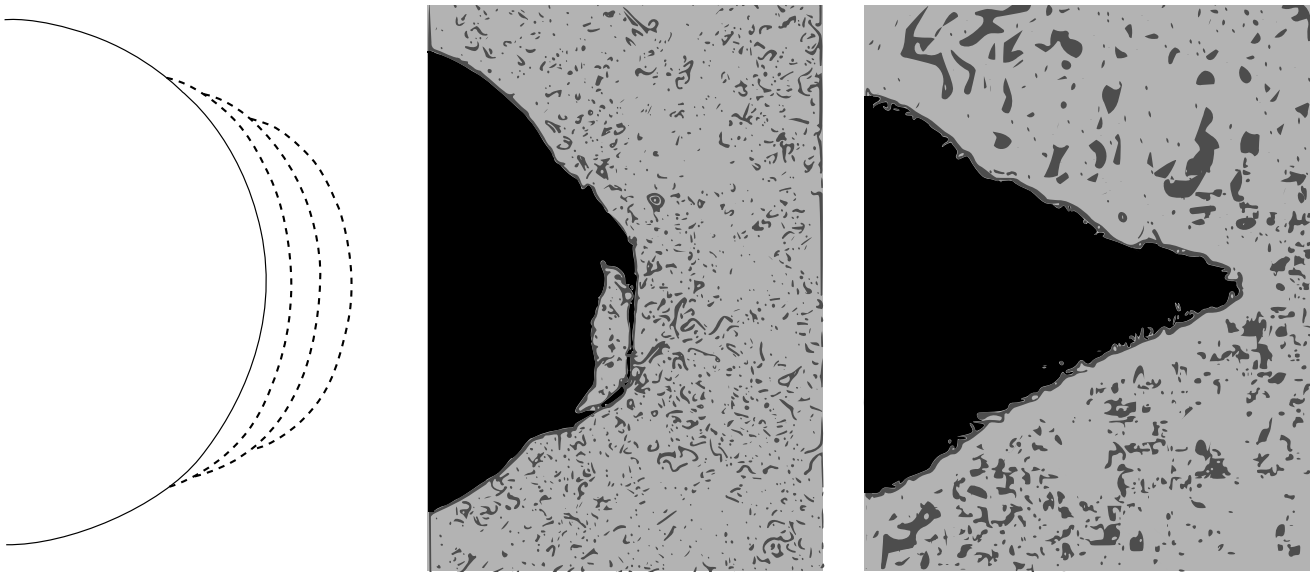

Figure 2.13: Drawings of progressive borehole breakouts forming. Drawing created after photos and sketches by Zoback et al. (2003).

to the direction of minimum principal stress. The thin pieces of rock between the cracks cannot support the high tangential stress which results in the pieces buckling and falling out. This process leads to dog-ear/V-shape breakouts as seen in Figure 2.12 (Haimson, 2007) (Lee & Haimson, 1993).

In sedimentary rock such as sandstones, porosity plays a part in the process but more importantly how well cemented the grains are. This was shown by Haimson and Lee (2004) when two sandstones of similar porosity but with different degrees of cementation were compared. The well cemented sandstone produced dog-ear breakouts in a way similar to granite. In the softer sandstone tested by Haimson and Lee (2004) the breakouts took a more fracture like slit shape as seen in Figure 2.14 through a phenomenon known as compaction bands. At the direction of minimum horizontal principal stress, the secondary stresses reach a level which causes the void ratio of the sandstone to lower due to compaction. By the circulation of water in the borehole, grains from the compacted bands start to loosen and a slit shape forms (Haimson & Lee, 2004). The width of the slit is governed by grain size and material parameters (Haimson & Kovacich, 2002). Experiments with Indiana limestone also showed dog-ear breakouts but through a process of shear failures (Haimson, 2007).

In an experimental study by Meier, Rybacki, Reinicke, and Dresen (2013) on shale, it was shown that failure during hydrostatic in-situ stresses will be shear dominated, resulting in a shear plane pattern as shown in Figure 2.15. They also found that the shape of the failure plane could be modelled with the Mohr-Couloumb failure criterion and as previously mentioned, smaller size boreholes can endure higher loads.

2.4.1 Measuring of breakouts

For any borehole logging dependent on the azimuth, such as the measurement of breakouts, the orientation of the measuring equipment must be recorded. The orientation data is often recorded against the earth's magnetic field through magnetometers and accelerometers (Prensky, 2015). Such measuring equipment

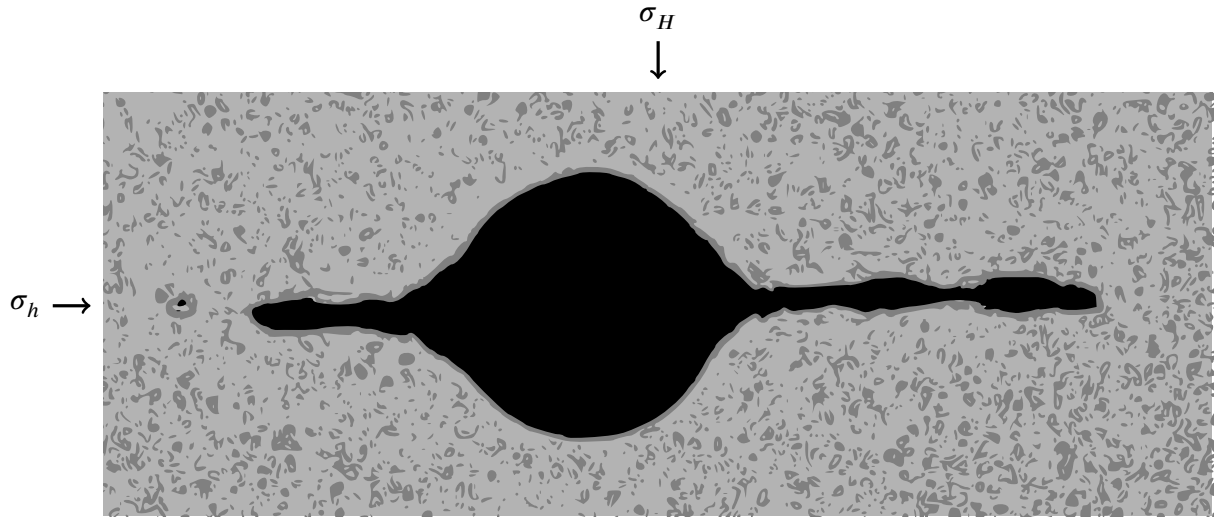

Figure 2.14: Breakout formed by compaction bands in a sandstone with high porosity. Drawing created after a photo by Haimson and Kovacich (2002).

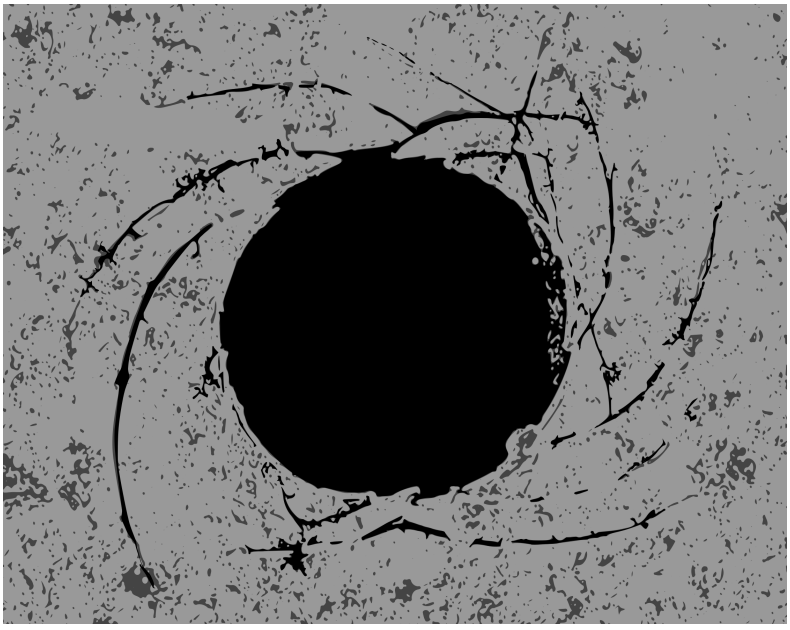

Figure 2.15: Shear fractures surrounding a borehole as a result of hydrostatic loading. Drawing created after a photo from an experimental study by Meier, Rybacki, Reinicke, and Dresen (2013).

in the oil industry generally has an azimuth accuracy of $\pm 3°$ and $\pm 0.3°$ for the tilt angle (Ren, Wang, Wang, Wu, & Wei, 2014).

One of the most basic measurement tools for logging breakouts and hole geometry is the 4- (or more) arm caliper. The spring loaded caliper arms extend to the interior hole wall and the tool then logs the radial distances in the different arm directions along the hole depth (U.S. National Committee for Rock Mechanics, Geotechnical Board, and National Research Council, 1993) (Zoback, 2007). Larger openings such as tunnels can be measured directly by optical methods such as 3D-scanners or total stations.

For boreholes the drilling fluid or mud is not always transparent which limits the usage of optical tools. Instead ultrasonic and resistivity televiewers are used to create images of the borehole wall. The ultrasonic sensor reliably creates image logs by emitting acoustic signals from the probe which reflect from the borehole wall returning radial distance and acoustic reflectivity (Zoback, 2007). The images can when interpreted reveal the condition of the borehole wall and in combination with drill cores the interpretation can be expanded to include e.g. fracture apertures and erosion effects. Resistivity measurements create images by measuring the electrical resistivity in the rock formation. The resistivity images can help to distinguish the type of rock structure and reveal fractures filled with fluid (U.S. National Committee for Rock Mechanics, Geotechnical Board, and National Research Council, 1993).

Acoustic logs can be used to estimate elastic modulus, shear strength and Poisson's ratio. Even though there are some difficulties with measuring the static elastic modulus through acoustics the method can still give an indication of the distribution of mechanical properties along the hole depth (U.S. National Committee for Rock Mechanics, Geotechnical Board, and National Research Council, 1993), as cited in (Paillet and Morin, 1988, Tarif et al., 1988).

A good way to estimate the smallest principal stress is hydraulic fracturing or leak off tests (Zoback et al., 2003). Leak off tests (LOT) are based on pumping water at a constant rate into a segment of a well closed off by packers. Eventually the pressure in the section will be high enough for the rock to fracture which leads to a noticeable pressure drop due to the increase in well volume. Since the fracture will extend perpendicular to the direction of smallest principal stress, the logged leak off point will be an approximation of said principal stress.

2.4.2 Stress estimation from borehole breakouts

With a variety of different rock types studies such as Haimson and Lee (2004) and Ewy and Cook (1990) have been conducted on borehole breakouts. Even though the failure process differs depending on rock type and its composition most of the studies find that the dimensions of the borehole breakout are related to the in-situ stress state.

The procedure of determining the maximum horizontal stress through breakout orientation and magnitude and the minimum horizontal stress through other means is suggested by several studies (Zoback et al., 2003); Lee and Haimson, 1993).

Since the in-situ stress state is sensitive to faults and fractures in the rock mass the breakout orientation and the mode of failure may change locally. For a clear indication of the general in-situ stress state it is preferable for analysis that the breakouts are aligned in the same direction over some length and through different types of formations. Analysis is still possible although care must be taken before drawing conclusions from the breakouts. Rock anisotropy and non circular geometries may also be of concern since it can have an effect on the breakout formation (Ewy & Cook, 1990). Deviated wells increase the complexity due to drilling induced tensile fractures and are often ignored when attempting to determine

the in-situ stress (Zoback, 2007).

Determining the in-situ stress state was made in practice by Brudy et al. (1997) in the KTB (Kontinentales Tiefbohrprogramm der Bundesrepublik Deutschland) scientific borehole. Finding the in-situ stress state was achieved by LOT, hydraulic fracturing and analysis of borehole breakouts.

To demonstrate the relation of borehole breakouts to in-situ stress and the rock properties, a secondary stress state for a borehole has been plotted in Figure 2.16. The secondary stress state was determined with the Kirsch (1898) solution from Section 2.1.2. In conjunction, the rock was assumed to obey the Mohr-Coulomb's criterion that was described in Section 2.3, see Figure 2.17. The horizontal in-situ stresses σ_h and σ_H acting on the borehole are related by a ratio of 5, where $\sigma_H = 50$ MPa. In Figure 2.16 the secondary stress distribution displays an area of tensile stress in the direction of the largest horizontal in-situ stress and an area of increased compressive stresses in the direction of the minor horizontal in-situ stress. When testing the secondary stress state with the failure criterion in Figure 2.17, zones of shear failures appear toward the minor horizontal in-situ stress. Although all variables for the rock strength in this case were chosen arbitrarily, the example shows that the theory is consistent with real world observations of breakouts. During the creation of this example different in-situ stress ratios and rock strength parameters were tested. The tests made it obvious that the shape of the failure zones are highly dependent on the failure criterion and in-situ stresses. A conclusion that can be drawn from this observation is that, when determining in-situ stresses from existing breakouts, knowing the properties of the rock and the failure mechanism is required. These two components will be essential if trying to recreate the breakout shape and through that pinpoint the in-situ stresses.

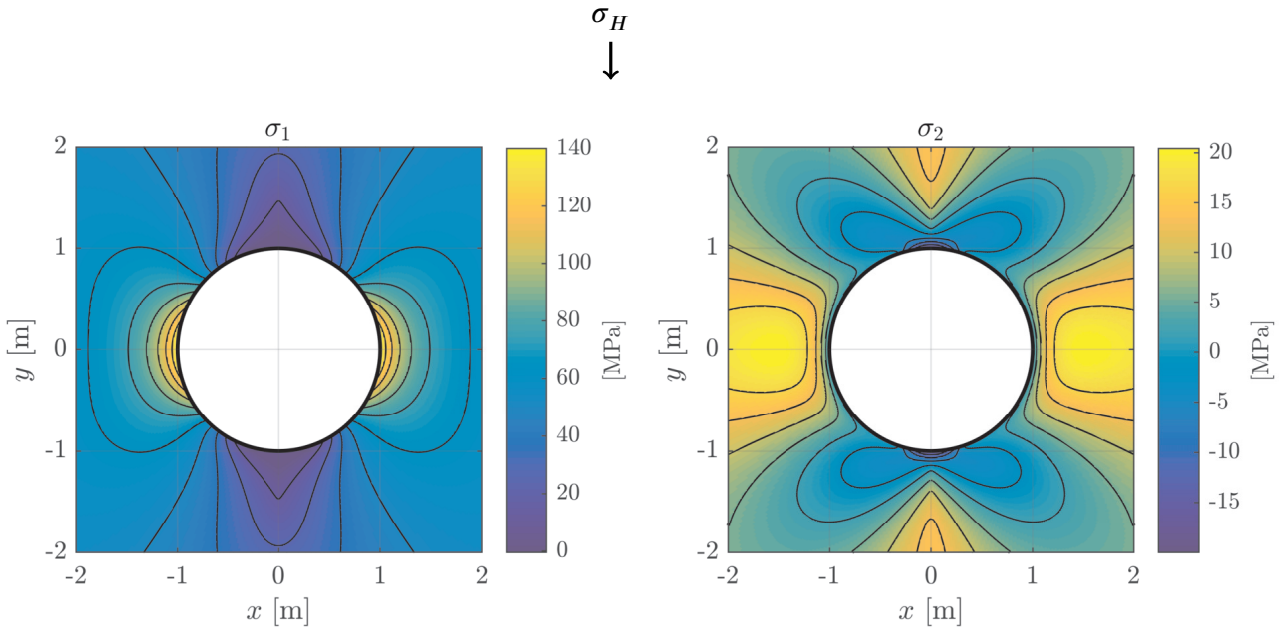

Figure 2.16: Major σ_1 and minor σ_3 principal secondary stresses around a borehole. The borehole is subject to an anisotropic in-situ stress state. The two in-situ stresses are related by a factor of 5 as $\sigma_H = 5 \cdot \sigma_h$, where $\sigma_H = 50$ MPa. In the direction of σ_H an area of tension occurs on the borehole wall whilst an increase of compressive stresses occurs in the direction of σ_h.

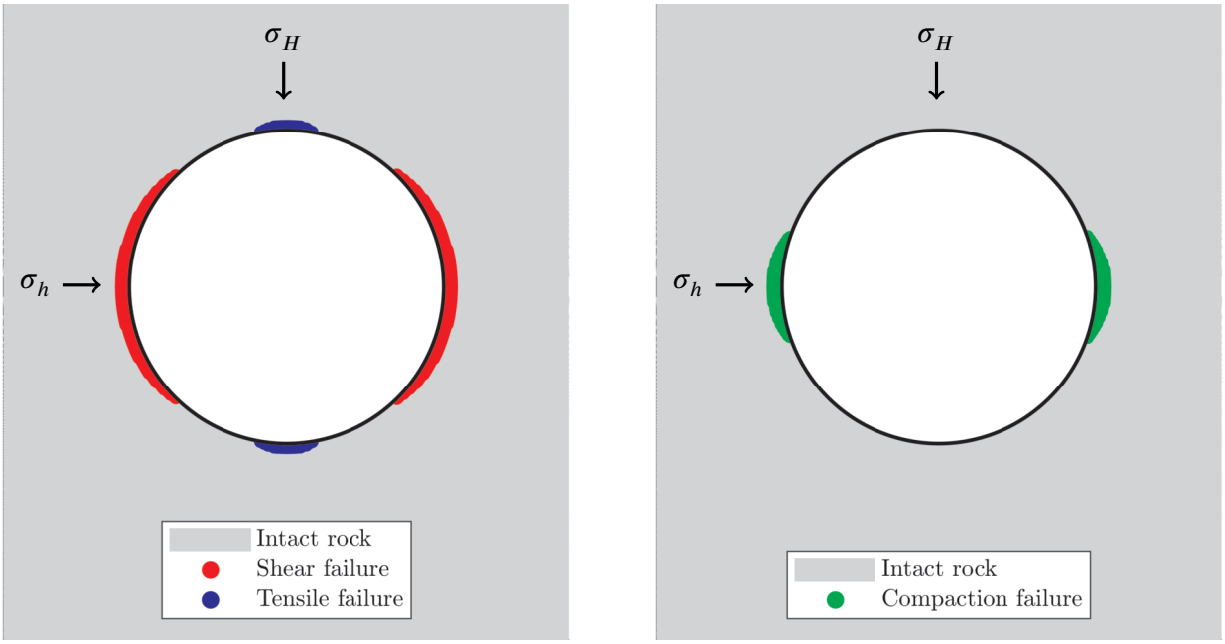

(a) (b)

Figure 2.17: Visualization of the direction of shear, tensile and compaction failure zones for a circular hole subject to anisotropic in-situ stresses. The zones were determined on a borehole with in-situ stresses related as $\sigma_h/\sigma_H = 0.3$, rock properties for the failure criterion's were chosen arbitrarily. Sub-figure (a) shows a case of shear failure with Mohr-Coulomb's criterion and a tensile failure. Sub-figure (b) displays compaction failure.

2.5 Conformal mapping

The goal is to find the stress distribution around an arbitrary shaped cavity/borehole. The problem is described in a complex plane $w = a + ib$ which will be referred to as the problem domain. In another complex plane $z = x + iy$ called the reference domain, the stress distribution will be solved under a simpler geometry such as the unit circle. For this solution to be of any use it is required to find a function $f(z) = w$ that maps the solution from the reference domain onto the problem domain w. First the problem must be translated to the reference domain z by transforming the boundary conditions through another mapping $z = \omega(w)$. See Figure 2.18.

The mapping functions $\omega(w)$ and $f(z)$ must be found and one way to do this is by assuming that the functions can be expanded as power series (Schinzinger & Laura, 1991). Power series work well for geometries that are near circular in shape. If this is not the case many terms of the series will be required to achieve an acceptable approximation. In Equation (2.40) the power series of $f(z)$ that maps the exterior of the unit circle onto the exterior of an arbitrary geometry is shown.

$$w = f(z) = \sum_{n=0}^{\infty} q_n z^{1-n} \tag{2.40}$$

Depending on the nature of the problem many different methods for finding mapping functions other

than the power series expansion exist e.g. bilinear and Schwarz-Cristoffel transforms.

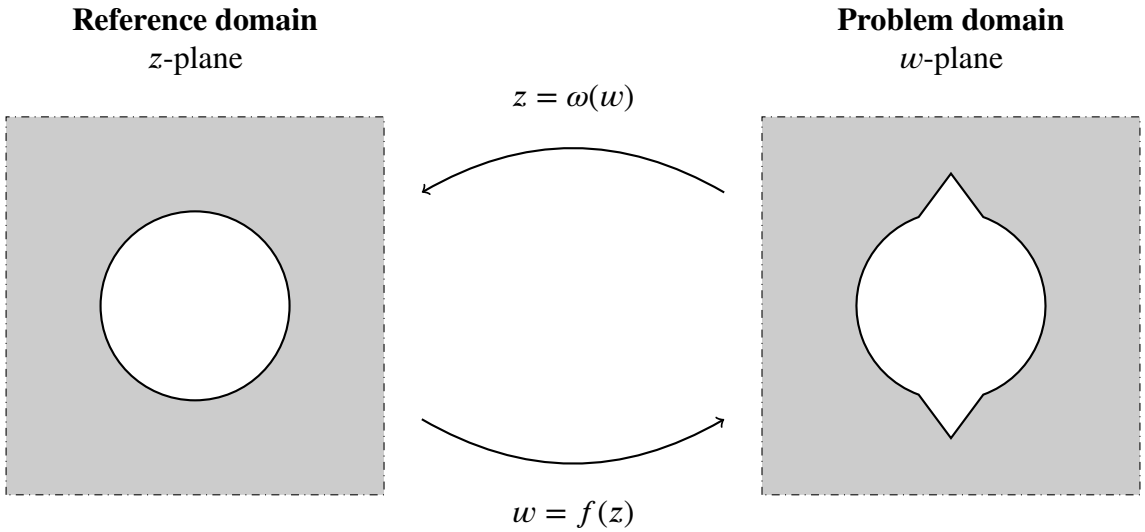

Figure 2.18: The problem is defined in the w plane and is then translated into a simpler geometry in the z plane. In the simple reference domain z the problem is solved and the solution can then be mapped back onto the original problem geometry in w.

Mapping of the Airy stress function - Kolosov and Muskhelishvili solution

In Section 2.1.2 a solution for the secondary stress state was found expressed in terms of the problem domain w. The goal is now to express the problem domain solution in terms of the simpler reference domain z. The method used by Muskhelishvili (1977) is to first set up a notation to accommodate working with the two domains. To separate the two domains the stress functions ϕ and χ for the reference domain have subscripts so that the notation is

$$\phi_r(z), \quad \chi_r(z), \quad \phi_r'(z), \quad \chi_r'(z)$$

to emphasize that these functions belong to the reference domain. The problem domain keeps the notation from Section 2.1.2 as shown in Equation (2.41).

$$\phi(w), \quad \chi(w), \quad \phi'(w), \quad \chi'(w) \tag{2.41}$$

Through the assumption that the conformal maps in Equation (2.42) exist the stress functions of the problem domain can be expressed in terms of the reference domain, see Equation (2.43).

$$\begin{aligned} z &= \omega(w) \\ w &= f(z) \end{aligned} \tag{2.42}$$

$$\phi(w) = \phi_r(z) = \phi_r\big(\omega(w)\big), \quad \chi(w) = \chi_r(z) = \chi_r\big(\omega(w)\big) \tag{2.43}$$

By applying the chain rule and the inverse function theorem the derivatives of the transformed stress functions can be found as shown in Equation (2.44).

$$\begin{aligned}\phi'(w) = \phi_r'(z) = \frac{d\phi_r\big(\omega(w)\big)}{dw} = \frac{d\phi_r}{dz}\frac{dz}{dw} = \frac{\phi_r'(z)}{f'(z)}\\ \chi'(w) = \chi_r'(z) = \frac{d\chi_r\big(\omega(w)\big)}{dw} = \frac{d\chi_r}{dz}\frac{dz}{dw} = \frac{\chi_r'(z)}{f'(z)}\end{aligned} \tag{2.44}$$

Similarly the same method can be used for finding the second derivative of $\phi(w)$

$$\begin{aligned}\phi''(w) = \phi_r''(z) = \frac{d^2\phi_r''}{dz^2}\left(\frac{dz}{dw}\right)^2 + \frac{\phi_r}{dz}\frac{d^2z}{dw^2} = \frac{\phi_r''(z)}{f'(z)^2} + \phi_r'(z)\cdot\left(\frac{-f''(z)}{f'(z)^3}\right) \Rightarrow\\ \phi''(w) = \frac{\phi_r''(z)f'(z) - \phi_r'(z)f''(z)}{f'(z)^3}\end{aligned} \tag{2.45}$$

Now the solution to the problem in w can be given as the solution in the reference domain z as shown below.

$$\sigma_{xx} + \sigma_{yy} = 4\mathfrak{R}[\phi'(w)] = 4\mathfrak{R}\left[\frac{\phi_r'(z)}{f'(z)}\right] \tag{2.46}$$

$$\sigma_{yy} - \sigma_{xx} + 2i\sigma_{xy} = 2[\overline{w}\phi''(w) + \chi'(w)] = 2\left[\overline{f(z)}\frac{\phi_r''(z)f'(z) - \phi_r'(z)f''(z)}{f'(z)^3} + \frac{\chi_r'(z)}{f'(z)}\right] \tag{2.47}$$

And in radial coordinates as

$$\sigma_{\theta\theta} - \sigma_{rr} + 2i\sigma_{r\theta} = [\sigma_{yy} - \sigma_{xx} + 2i\sigma_{xy}]e^{2i\theta} \tag{2.48}$$

The relation for the interior boundary stated in Equation (2.27) becomes

$$\begin{aligned}\phi(w) + w\overline{\phi'(w)} + \overline{\chi'(w)} = p_0 w \Rightarrow\\ \phi_r(z) + f(z)\frac{\overline{\phi_r'(z)}}{\overline{f'(z)}} + \frac{\overline{\chi_r'(z)}}{\overline{f'(z)}} = p_0 f(z)\end{aligned}$$

Which when simplified gives

$$\overline{f'(z)}\phi_r(z) + f(z)\overline{\phi_r'(z)} + \overline{f'(z)\chi_r'(z)} - p_0 f(z)\overline{f'(z)} = 0 \tag{2.49}$$

For this solution to be of any use the function for the conformal mapping of $w = f(z)$ must be found. To achieve this the power series shown in Equation (2.40) that maps the exterior of the unit circle to the exterior of an arbitrary cavity is used.

Since ϕ_r and χ_r are finite valued they can be expanded as power series as

$$\begin{aligned}\phi_r(z) &= \sum_{n=0}^{\infty} A_n z^{1-n} = Az + \sum_{n=1}^{\infty} A_n z^{1-n} \\ \chi_r(z) &= \sum_{n=0}^{\infty} B_n z^{1-n} = Bz + \sum_{n=1}^{\infty} B_n z^{1-n}\end{aligned} \tag{2.50}$$

With corresponding derivatives

$$\begin{aligned}\phi_r'(z) &= A + \sum_{n=1}^{\infty}(1-n)A_n z^{-n} = A + \sum_{n=1}^{\infty} a_n z^{-n} \\ \chi_r'(z) &= B + \sum_{n=1}^{\infty}(1-n)B_n z^{-n} = B + \sum_{n=1}^{\infty} b_n z^{-n}\end{aligned} \tag{2.51}$$

The terms A_1 and B_1 equal 0 since rigid body displacements and rotations are restricted. For finding the first coefficients A and B in the series, the in-situ stress $\sigma_{xx} = \sigma_h$ and $\sigma_{yy} = \sigma_v$ can be applied through Equation (2.46). This results in the following

$$\sigma_h + \sigma_v = 4\Re\left[\frac{\phi_r'(z_\infty)}{f'(z_\infty)}\right]$$

$$\frac{\sigma_h + \sigma_v}{4} = \Re\left[\frac{A + \sum_{n=1}^{\infty} A_n z_\infty^{-n}}{f'(z_\infty)}\right]$$

$$\frac{\sigma_h + \sigma_v}{4} = \Re\left[\frac{A}{f'(z_\infty)}\right]$$

$$A = \frac{\sigma_h + \sigma_v}{4} f'(z_\infty)$$

The derivative of Equation (2.40) evaluated at infinity, $f'(z_\infty)$ results in a single constant that here is denoted as R. By using this scale factor R, the first coefficient A is

$$A = \frac{\sigma_h + \sigma_v}{4} R \tag{2.52}$$

The coefficient B can be found by using Equation (2.47). When concluding that $\phi_r''(z_\infty) \to 0$ and $f''(z_\infty) \to 0$ it results in

$$B = \left(\frac{\sigma_v - \sigma_h}{2} + i\tau_{hv}\right) R \tag{2.53}$$

The rest of the coefficients in the power series will be determined in Section 3.1 through Equation (2.49).

3 The computational tool

This chapter explains the design of the computational tool programmed in MATLAB. The first section, 3.1 describes how the conformal mapping power series constants are determined and how an arbitrary geometry is defined and sampled before the mapping. Section 3.2 shows how the power series coefficients of the stress functions are evaluated. The last section of the chapter, Section 3.3 describes the workflow of the main application of the tool which is simulating borehole breakouts given in-situ stress and a failure criterion of the rock. The section also explains how smoothing is used to stabilize the iterative process of simulating progressive rock failure.

3.1 Evaluating mapping

The previously assumed power series transform

$$w = f(z) = \sum_{n=0}^{\infty} q_n z^{1-n}$$

will now be found with the goal of mapping the exterior of the unit circle in the reference domain onto the exterior of the cavity in the problem domain. A technique that achieves this is the method of simultaneous equations by Kantorovich (1933) (Schinzinger & Laura, 1991). The method begins with expressing the boundary as an implicit function $h(z)$ with the assumption that it can be estimated as a Fourier series. For near circular holes with breakouts a possible way of describing the boundary mathematically is through the circle equation with a varying radius r depending on the reference domain argument angle θ. Denote the interior boundaries of z and w in polar form

$$z = e^{i\theta} \tag{3.1}$$

$$w = r(\gamma)e^{i\gamma} \tag{3.2}$$

In the reference domain z the boundary consist of the unit circle with a radius of 1. The problem domain boundary w has a varying radius $r(\gamma)$ depending on the argument angle γ in the problem domain, see Figure 3.1.

In complex numbers the circle equation that represents the boundary is

$$w \cdot \overline{w} = r(\gamma)^2 \tag{3.3}$$

Let $g(\theta) = r(\gamma)^2$. By inserting this into Equation (3.3) the following is obtained

$$w \cdot \overline{w} = g(\theta) \tag{3.4}$$

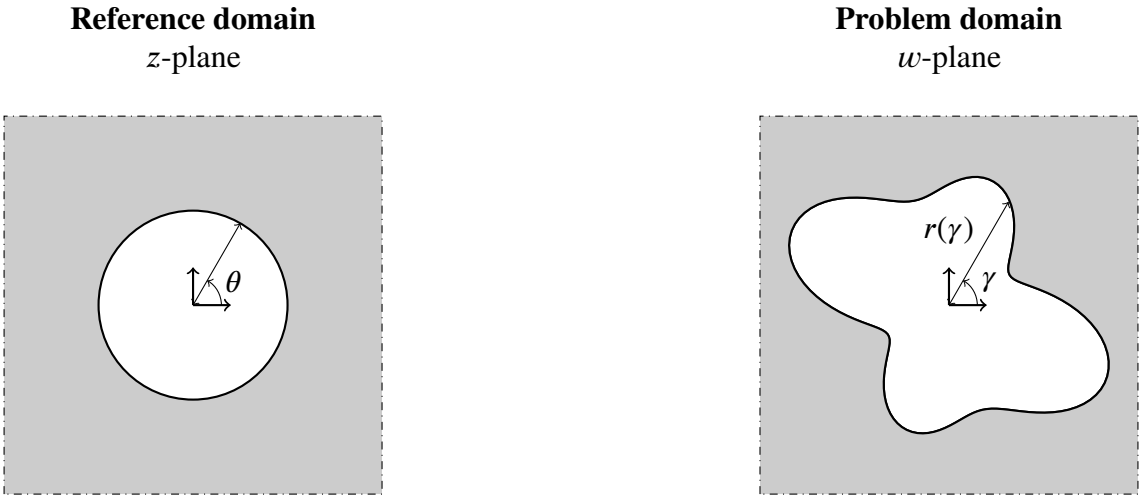

Figure 3.1: The unit circle in the reference domain and an arbitrary region in the problem domain. The varying radius of the arbitrary region is described as a function $r(\gamma)$ of the argument angle γ. In the reference domain the unit circle is described by the argument θ and a fixed radius of 1.

The function $g(\theta)$ can then be expanded as a Fourier series approximation which can be calculated through Fast Fourier Transform (FFT)

$$g(\theta) \approx \sum_{n=-k}^{k} c_n e^{in\theta} \tag{3.5}$$

Equations 3.5, 3.4 and 2.40 are combined into

$$\sum_{n=-1}^{k} q_n e^{i(1-n)\theta} \sum_{m=-1}^{k} q_m e^{i(1-n)\theta} = \sum_{n=-k}^{k} c_n e^{in\theta} \tag{3.6}$$

When simplifying Equation (3.6) its found that

$$\sum_{n=0}^{k} \sum_{m=n}^{k} q_{m-n} \cdot \overline{q}_m e^{in\theta} + \sum_{n=0}^{k} \sum_{m=n}^{k} q_m \overline{q}_{m-n} \cdot e^{-in\theta} = \sum_{n=-k}^{k} c_n e^{in\theta} + \overline{c_n} e^{-in\theta} \tag{3.7}$$

If terms of the same exponents in Equation (3.6) are equated it results in a system of equations as seen below.

$$\sum_{m=n}^{k} q_{m-n} \cdot \overline{q}_m = c_n, \qquad n \in \{0, 1, \dots, k\} \tag{3.8}$$

Since the coefficients are of the complex form $q_m = p_m + is_m$ Equation (3.8) can be rewritten into

$$\begin{aligned}\sum_{m=n}^{k}(p_{m-n}p_m + s_{m-n}s_m) &= \mathfrak{R}[c_n] \\ \sum_{m=n}^{k}(s_{m-n}p_m - s_m p_{m-n}) &= \mathfrak{I}[c_n]\end{aligned} \tag{3.9}$$

The system of equations that describe the coefficients can then be calculated using the Newton-Raphson method with an relaxation parameter. Algorithms for finding the FFT's of a sampled geometry and its mapping were provided by Gerolymatou (2019). These functions were left unchanged except for a part of the mapping function that enforced symmetry in the mapping by setting every second term of the mapping constants to zero. With the ambition to evaluate mappings of any arbitrary polygon geometry in this thesis, functions to define a geometry and sample it were coded for use prior to the FFT and the mapping algorithm.

3.1.1 Defining a geometry

First a polygon had to be defined as a list of vertex coordinates x and y. Additionally every vertex was accompanied by a radius value r, describing the radius of a curve from the current vertex to the next one in the list, see Figure 3.2 for an graphical example.

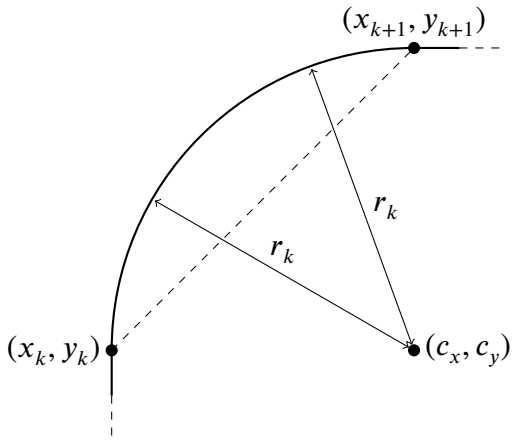

Figure 3.2: A curved segment of the geometry with the radius r_k between the two polygon vertex points (x_k, y_k) and (x_{k+1}, y_{k+1}).

To simplify plotting and sampling of the arc segments, they are estimated as polygonal chains using 1000 vertexes per arc segment. Combining the original polygon with the polygonal chain estimates of the arc segments, an arbitrary geometry can be created for further use in the tool. Using linear algebra the coordinates of a curved segment between two vertices can be calculated. First define the vertex points as

$$P_1 = \begin{bmatrix} x_k \\ y_k \end{bmatrix}, \quad P_2 = \begin{bmatrix} x_{k+1} \\ y_{k+1} \end{bmatrix} \tag{3.10}$$

The distance between the points d, the two possible arc centers $C_{1,2}$ and the interval t_a to t_b that describes the arc are defined as

$$\begin{aligned} d &= \sqrt{(x_{k+1} - x_k)^2 + (y_{k+1} - y_k)^2} \\ C_{1,2} &= \begin{bmatrix} c_x \\ c_y \end{bmatrix} = \frac{1}{2}(P_2 + P_1) \pm \frac{1}{d}\sqrt{r^2 - \frac{d^2}{4}} \begin{bmatrix} 0, -1 \\ 1, 0 \end{bmatrix} (P_2 - P_1) \\ t_a &= \arctan \frac{y_{k+1} - c_y}{x_{k+1} - c_x} \\ t_b &= \arctan \frac{y_k - c_y}{x_k - c_x} \end{aligned} \tag{3.11}$$

Some logic is necessary in the MATLAB implementation to choose either of the two possible arc centers $C_{1,2}$, the tool was designed so that a negative radius would mean a "left" turn of the curve and a positive radius a "right" turn. The radius r must also be larger or equal to $d/2$. With the results from Equation (3.11) the arc is thus parametrized as

$$\left.\begin{aligned} x(t) &= c_x + r\cos t \\ y(t) &= c_y + r\sin t \end{aligned}\right\} \quad t_a \leq t \leq t_b \tag{3.12}$$

The dense set of vertices from the arcs are then added to the initial polygon coordinate list. After sorting vertices in MATLAB the geometry is ready for further processing before mapping it.

3.1.2 Centering the geometry

The center of gravity and area of the polygon is then calculated as seen in Equation (3.13) (Bourke, 1988). The polygon area is also used as a break criterion when producing breakouts from in-situ stress, see more in Section 3.3.

$$\begin{aligned} A &= \frac{1}{2}\sum_{i=0}^{k-1}(x_k y_{k+1} - x_{k+1} y_k) && \text{Gauss's area formula} \\ C_x &= \frac{1}{6A}\sum_{i=0}^{k-1}(x_k + x_{k+1})(x_k y_{k+1} - x_{k+1} y_k) && \text{Centroid } x\text{-coordinate} \\ C_y &= \frac{1}{6A}\sum_{i=0}^{k-1}(y_k + y_{k+1})(x_k y_{k+1} - x_{k+1} y_k) && \text{Centroid } y\text{-coordinate} \end{aligned} \tag{3.13}$$

The coordinates of the polygon are then translated so that its center of gravity is positioned at the origin $(0, 0)$, see Equation (3.14). Vertex coordinates before the translation are denoted (X_k, Y_k) and the new coordinates after translation $(\hat{X}_k, \hat{Y}_k)$. Translation is performed since the points along the boundary are sampled as the distance from the origin. This will make sure that the designed geometry is surrounding the origin and that it is positioned in a favourable way for the sampling process.

$$\begin{bmatrix} \hat{X}_k \\ \hat{Y}_k \end{bmatrix} = \begin{bmatrix} X_k \\ Y_k \end{bmatrix} - \begin{bmatrix} C_x \\ C_y \end{bmatrix} \tag{3.14}$$

3.1.3 Sampling a polygon

Before the provided functions can be used and a mapping evaluated, the polygon geometry must be sampled at an evenly spaced angular interval, see Figure 3.3.

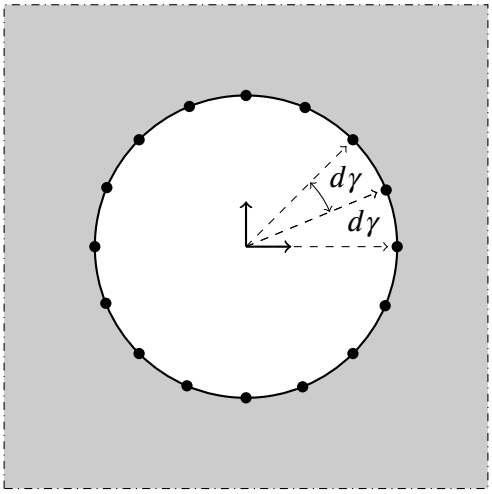

Figure 3.3: A circular borehole in the problem domain sampled at 16 points with an equal angular interval $d\gamma$.

The number of samples n, is first chosen. A vector of $n+1$ sample angles t ranging from 0 to 2π radians are created, the last sample $n+1$ in the vector is then removed to avoid sampling the initial point twice. At the angles specified by the vector of linearly spaced angles, samples are collected from the polygon geometry. The algorithm finds the vertex k with an argument angle smaller than the current sample angle, and the vertex $k+1$ with a larger argument angle. It can then be derived that the sample value $f_{s,k}$ that lies between the two vertices is calculated as

$$\begin{aligned} \alpha_k &= \arctan \frac{y_{k+1} - y_k}{x_{k+1} - x_k} \\ f_{s,k} &= \frac{x_k \sin \alpha_k - y_k \cos \alpha_k}{\cos t_k \sin \alpha_k - \sin t_k \cos \alpha_k} \end{aligned} \tag{3.15}$$

3.1.4 Geometry, sampling and mapping GUI-tool

To simplify the process of designing, sampling, and mapping a geometry and evaluating the mapping performance, a simple interactive tool was coded using the GUI Layout Toolbox by Sampson (2019) in MATLAB. When designing a geometry the GUI tool accepts x and y coordinates of a boundary polygon and a radius for curving a line segment between two coordinate points, see Figure 3.4. When a boundary has been constructed the tool can sample the geometry at any preferred number of sample points. During the sampling process the center of gravity of the initial geometry is determined so the geometry can be translated to the origin before sample points are collected. The geometry is translated so that it always centers at a favourable point for sampling and mapping. Once the geometry is sampled it can be mapped, see Figure 3.5. As a variable when evaluating the mapping, the number of series terms to use in the evaluation can be set to any positive integer value.

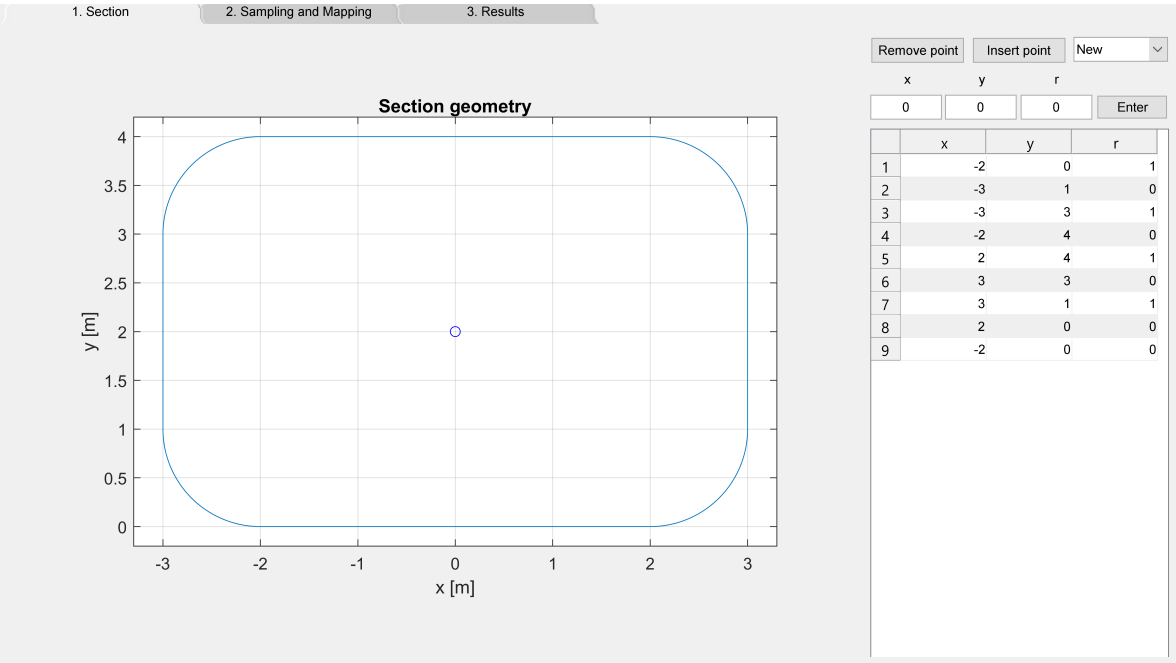

Figure 3.4: A snapshot of the boundary and mapping test tool, showing the geometry design tab.

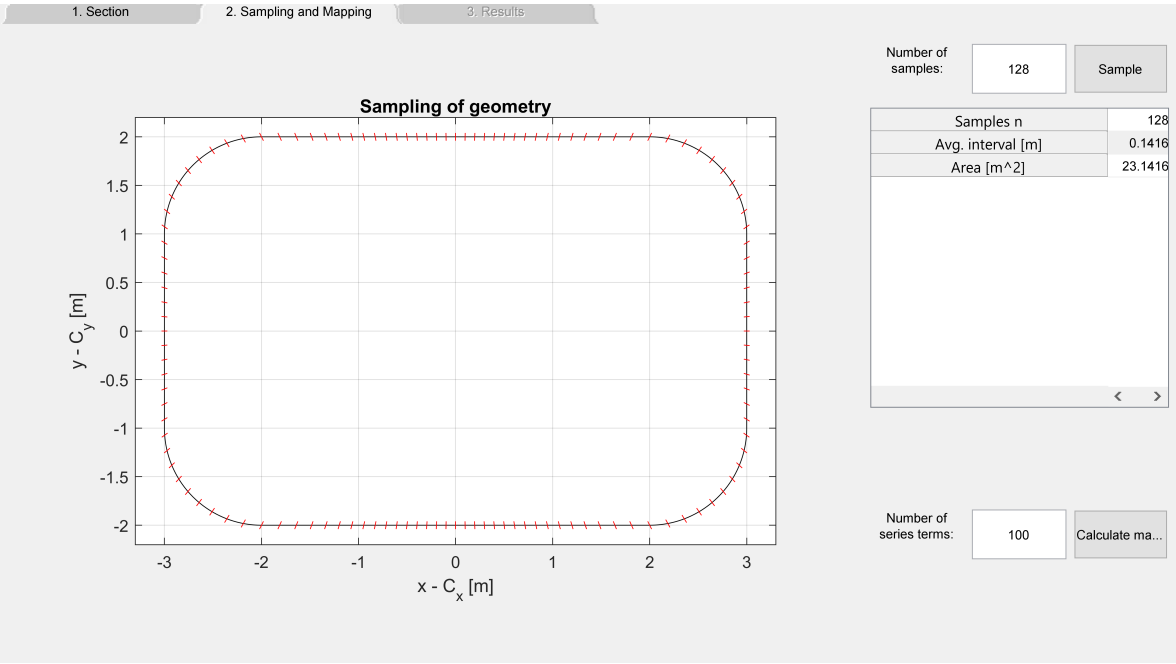

Figure 3.5: The boundary and mapping test tool showing the "sampling and mapping" tab. A boundary is sampled at 128 points, samples are notated by red marks around the boundary geometry. The geometry is centered with its centroid at the origin. By pressing the "Calculate mapping" button in the lower right corner a mapping of the sampled boundary using 100 series terms are evaluated.

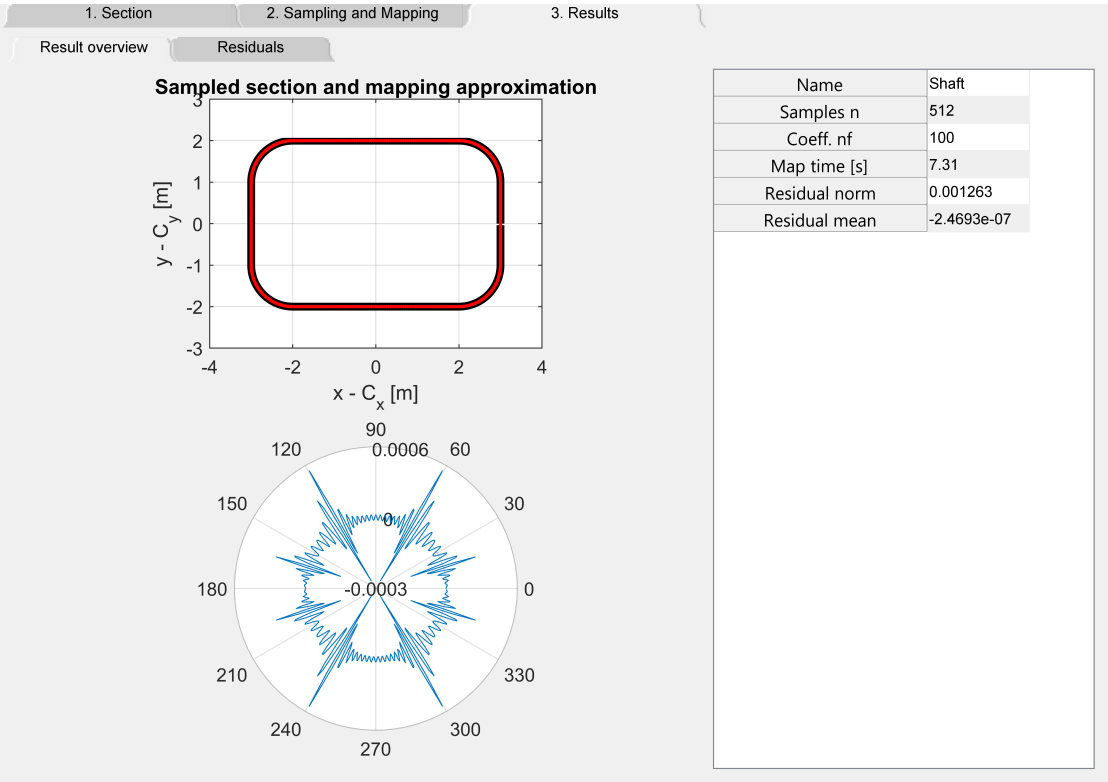

Figure 3.6: The mapping results overview tab, showing the sampled section displayed with a thick black line and the mapped one in a thinner red line. Below, the residual/error is shown in a polar style plot to visualize where the largest oscillations of the mapped boundary are located. To the right, sampling and mapping settings are displayed together with mapping time, residual norm and residual mean.

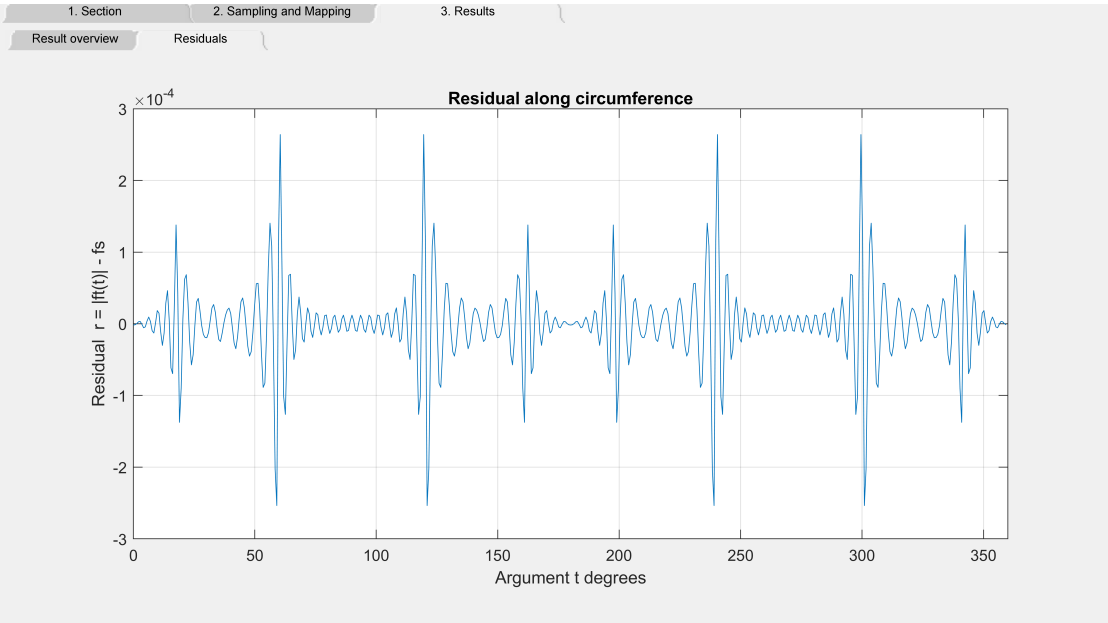

Figure 3.7: The last tab, Residuals, showing the residuals along the boundary in more detail.

After mapping, an overview of the results can be presented, see Figure 3.6. Residuals around the boundary can also be shown in detail, see Figure 3.7. The metrics seen in the result parts of the tool are described in more detail under Section 4.1, where examples of different mappings are presented. A geometry designed in the tool can be saved in .mat format for later import into the script described in Section 3.3 that simulates borehole breakouts.

3.2 Evaluating the stress function

The power series coefficients A_n and B_n of the stress functions ϕ_r and χ_r must be determined before the secondary stress state can be calculated. In Section 2.5 the first coefficients A and B were found using the boundary conditions at infinity and $A_1 = B_1 = 0$ from the fact that there are no displacements at infinity. All the remaining coefficients will be calculated through the boundary condition at the cavity interior by making use of Equation (2.49). The power series approximations of $f'(z)$, $\phi_r(z)$, $f(z)$, $\phi'(z)$ and $\chi_r(z)$ from Equations 2.40, 2.50 and 2.51 are inserted into Equation (2.49). After some simplifications it yields Equation (3.16) (Gerolymatou, 2019).

$$
\begin{aligned}
&\overline{f'(z)}\phi_r(z) + \quad f(z)\overline{\phi_r'(z)} + \overline{f'(z)\chi_r'(z)} - \quad p_0 f(z)\overline{f'(z)} = 0 \Rightarrow \\
&\sum_{n=2}^{k}\sum_{m=0}^{k}(1-m)A_n\overline{q}_m e^{i(1-n+m)\theta} + \sum_{m=0}^{k}(1-m)A_0\overline{q}_m e^{i(1+m)\theta} \\
&+\sum_{n=2}^{k}\sum_{m=0}^{k}(1-n)\overline{A}_n q_m e^{i(1-m+n)\theta} + \sum_{m=0}^{k}A_0 q_m e^{i(1-m)\theta} \\
&+\sum_{n=2}^{k}\sum_{m=0}^{k}(1-m)\overline{B}_n\overline{q}_m e^{i(m+n-1)\theta} + \sum_{m=0}^{k}(1-m)B_0\overline{q}_m e^{i(-1+m)} \\
&=p_0\sum_{n=0}^{k}\sum_{m=0}^{k}(1-m)q_n\overline{q}_m e^{i(1-n+m)}
\end{aligned}
\tag{3.16}
$$

If equating the exponents of equal order in the Equation (3.16) the linear system is over-constrained and can simply be solved numerically in MATLAB. The code for doing this in MATLAB was provided by Gerolymatou (2019).

3.3 From in-situ stress to borehole breakouts

This section will describe the process of simulating borehole breakouts from a certain in-situ stress using a chosen failure criterion. To begin with, the overall work flow and the layout of the algorithm that iterates until finding breakout shape is presented.

According to the flowchart in Figure 3.8 the geometry and stress distribution of a failed borehole are determined. Initial data of the hole geometry, the in-situ stresses and the failure criterion definition are inputted. If another geometry than a circular hole is subjected to analysis the geometry design tool described in Section 3.1.4 can be used to prepare a geometry. Geometries saved in the GUI tool can

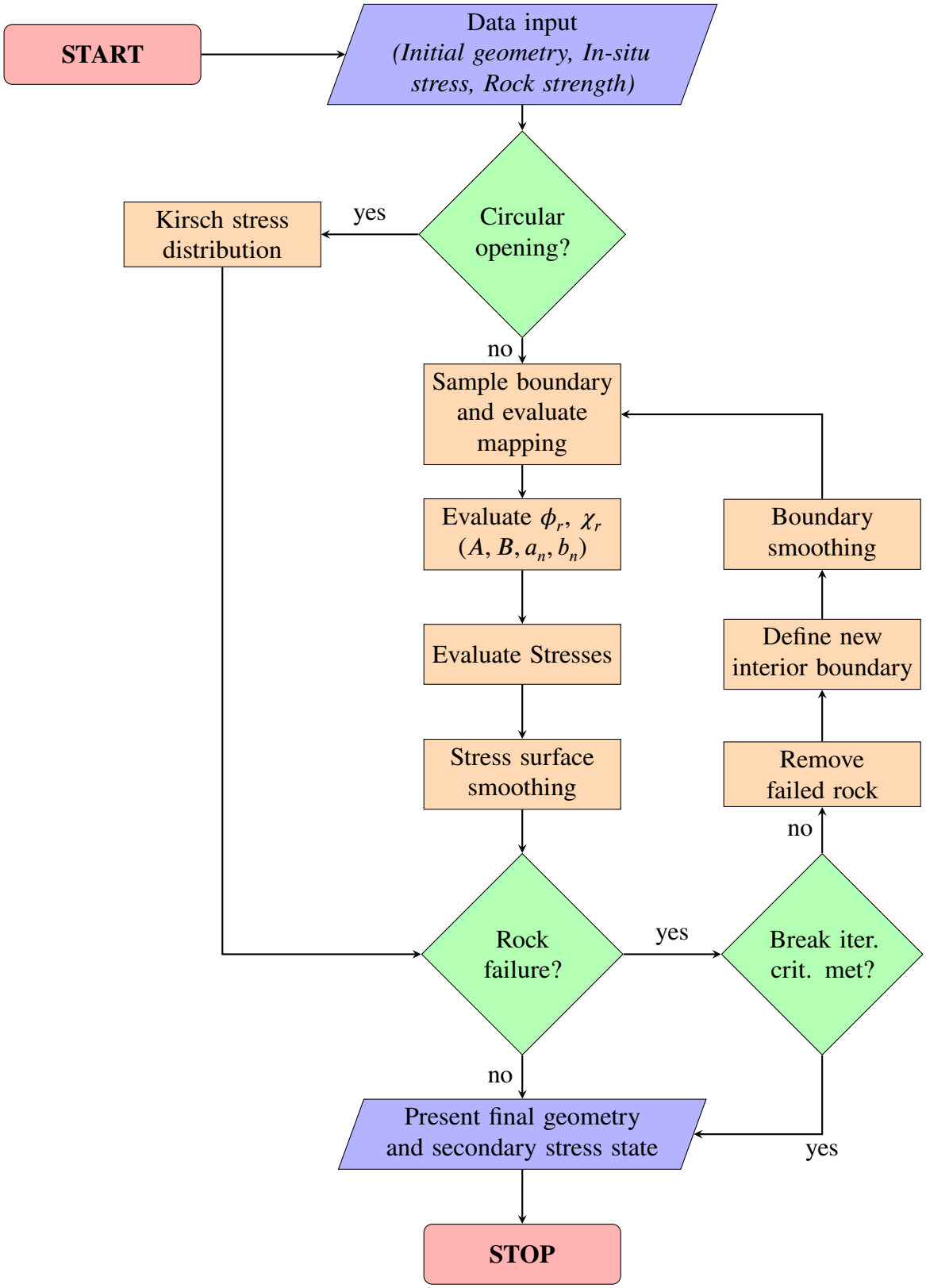

Figure 3.8: Flowchart for determining borehole breakouts from in-situ stress.

then be read directly by the script. Subsequently, stresses and failure can be evaluated around arbitrary regions other than circles. Depending on whether the initial hole geometry is circular or not the Kirsch solution or the Airy function by conformal mapping is used. In the case of a non circular geometry first the mapping function for the geometry is evaluated according to Section 3.1 followed by the evaluation of the stress functions from Section 3.2. When a secondary stress state is determined stresses can optionally be smoothed. From the smoothed stresses rock failure is controlled through the chosen failure criterion. If there is a failure, the failed nodes in the discretization are removed and a new interior boundary is defined. From this point the boundary is smoothed using a moving average filter before a new mapping and stress distribution is evaluated once more for the new boundary. The process is repeated until there are no more failures or if any break iteration criteria are fulfilled. Break criteria can be maximum number of iterations or if the failure area is below a set limit. When there are no failures or if the break criteria are met, the final geometry and secondary stresses are presented.

3.3.1 Sampling, mapping and region discretization

Non-circular geometries are sampled and the mapping constants are evaluated as described in Section 2.5. Following the angular direction around the unit circle boundary in the reference domain, a set number of angular nodes are placed. The same number of angular nodes are again placed at a log spaced interval by increasing the radius, making up a chosen number of radial node layers outside the unit circle, ranging from $r = [1, 1 + z_{dist}]$. The variable z_{dist} is most often sufficiently set to 1, but if stresses at some distance away from the boundary are of interest z_{dist} must be set to a higher value. After mapping the reference domain nodes to the problem domain, the corresponding problem domain meshgrid outside the initial geometry is created, see Figure 3.9 for an example.

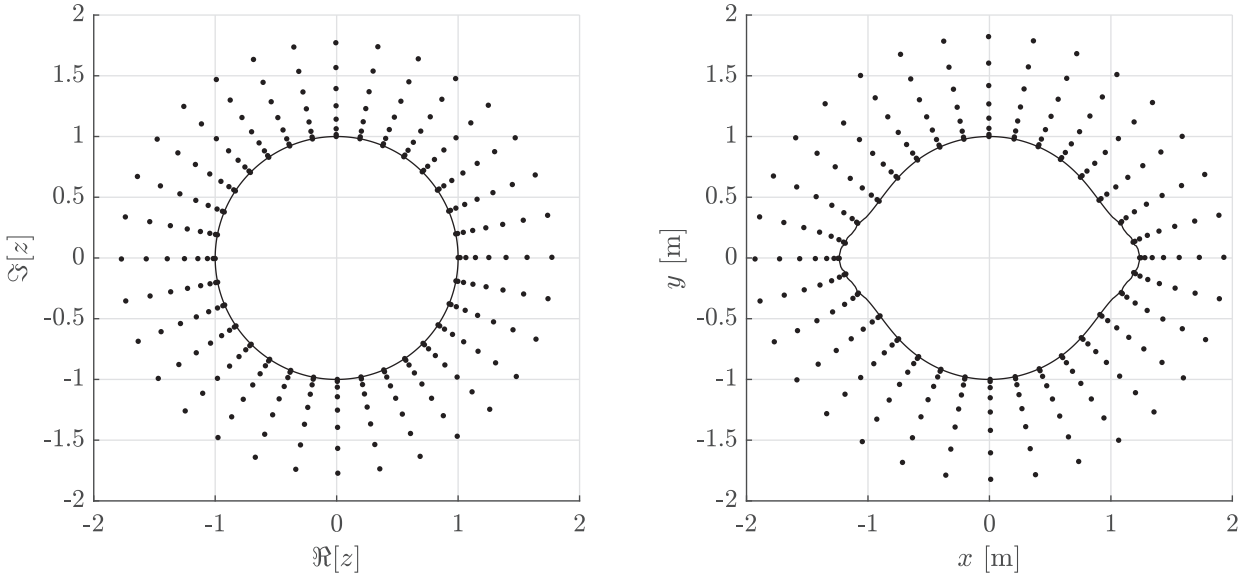

(a) Reference domain

(b) Problem domain

Figure 3.9: Example of discretization using 32 angular nodes times 8 radial nodes in the reference domain (a), with its corresponding mapped discretization in the problem domain (b). During an actual simulation, the node density is much larger than shown in this example.

If a circular borehole is used on the first iteration the mesh simply scales from the reference domain unit circle to the correct radius of the circular hole in the problem domain.

3.3.2 Stresses and stress surface smoothing

Stresses are evaluated either by using the Kirsch solution on circular geometries or by using the stress function series as shown in Section 3.2. When the stresses are evaluated they are returned as 2D tensor components. Secondary principal stresses are determined to simplify stress plotting, visual interpretation and to use the failure criterion definitions stated in Section 2.3. Principal stresses are calculated through the eigenvalues of stresses at every node, the direction of the largest principal stress is also calculated from the corresponding eigenvector.

During the iterative process of simulating progressive failure, the boundary oscillations and subsequent stress fluctuations stemming from the mapping can quickly destabilize the breakout simulation, see Figure 3.10.

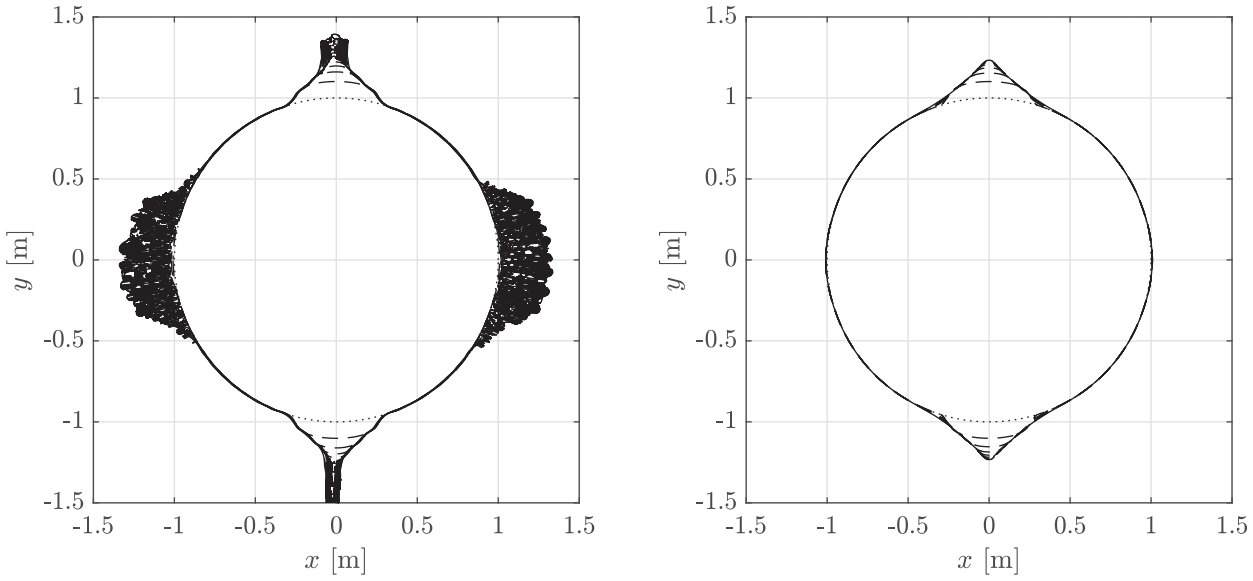

(a) Without smoothing

(b) With smoothing

Figure 3.10: Breakouts generated without smoothing are shown in (a) and breakouts generated with boundary and stress smoothing enabled shown in (b).

Even a small boundary oscillation leads to stress fluctuations at the boundary. When evaluating the failure criterion such stress fluctuations may potentially create irregularities in the redefined geometry. In the following iteration, both compressive and tensile stresses concentrate near the irregularities, causing additional larger irregularities in proximity to the initially small boundary oscillations. Gerolymatou (2019) used a moving average filter to smooth the boundary and achieve a more stable model. Since testing was performed on several boundaries with sharp corners which created plenty of boundary oscillations, a gentle smoothing of the stress surface in both angular and radial directions was also included. The stress smoothing helped alleviate some of the fluctuations stemming from non-smooth geometries and especially softened stress peaks at corners or irregularities in the geometry. The effect of

the stress surface smoothing can be seen in when comparing stresses before and after smoothing, see Figure 3.11.

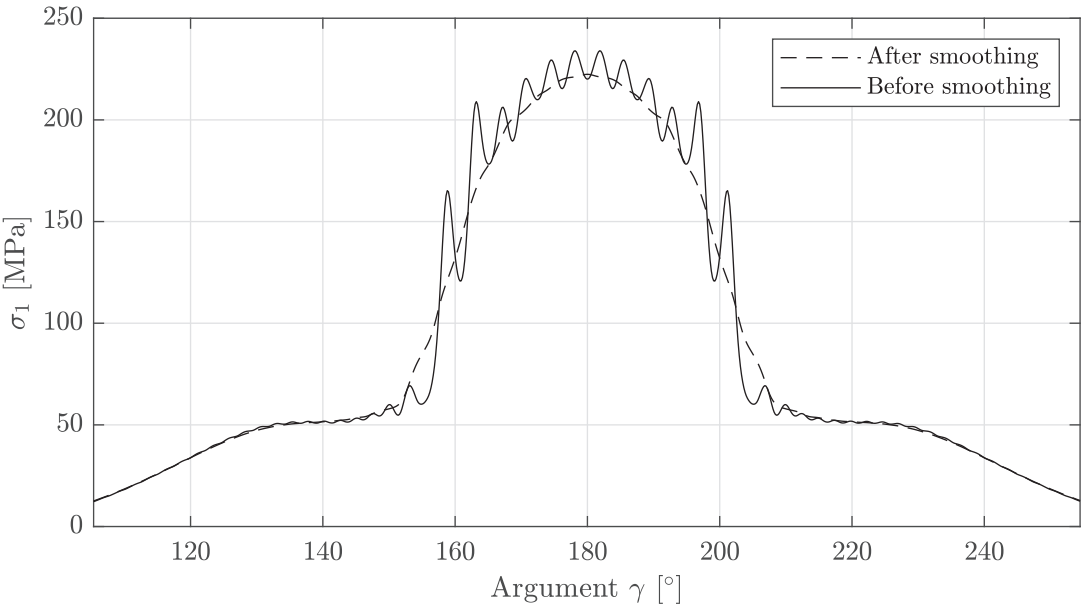

Figure 3.11: Boundary stresses at iteration 10 for an angular segment of the boundary, highlighting stresses before and after stress surface smoothing using 64 angular samples and 32 radial. Mesh was set to 2048 nodes in the angular direction and 1024 in the radial.

Smoothing in the radial direction was achieved with the MATLAB built in `smooth` function of the curve fitting toolbox. For smoothing in the angular direction a custom periodic moving average was used. The custom function was mainly programmed to smooth the boundary whilst taking account of the matrix edge between 2π and 0 radian, but the function was also applicable to the stress smoothing. The custom function to perform moving average smoothing across the 2π and 0 radian edge is described more in Section 3.3.4.

3.3.3 Defining a new boundary

Depending on the chosen failure criterion, either Mohr-Couloumb or Hoek-Brown as described in Section 2.3, each node is checked against the failure criterion, returning either shear, tensile or compaction failure in a matrix of the same size as the meshgrid.

When defining a new boundary all three failure matrices are combined into a single logical matrix which states if the corresponding node has failed or not. The MATLAB function `bwboundaries` is then used to find failed regions of nodes. Each of the defined regions are then checked against a few criteria: regions that are not connected to the boundary are discarded, and regions of less than a chosen number of nodes are also discarded to prevent very small failures inducing oscillations in the boundary during subsequent mapping.

By tracing the nodes constituting the previous boundary and the outer nodes of the failed regions, a new boundary polygon is created from the mesh discretization. The new boundary polygon can then be resampled and mapped for use in the following iteration.

3.3.4 Boundary smoothing

A custom moving average filter was programmed which can smooth a vector describing a periodic function such as the boundary. The function was programmed to achieve the correct smoothing at the start and end of the vector describing the boundary. For example, since the boundary is circular the end of the vector should be smoothed by also averaging points from the start of the vector, and vice versa.

The filter uses an odd number of N samples, if N is inputted as an even number, one extra sample is added to make it odd. Let $\boldsymbol{R}$ be a vector defining the boundary containing as many nodes as the mesh in the angular direction. The moving average radius $\boldsymbol{R}_{mavg}$ for each boundary node j in the vector $\boldsymbol{R}$ can be calculated using the continuous $\boldsymbol{R}_{cont}$ vector that includes the periodic mirror of $(N-1)/2$ samples on the start and end of the vector $\boldsymbol{R}$, see Figure 3.12 for an example.

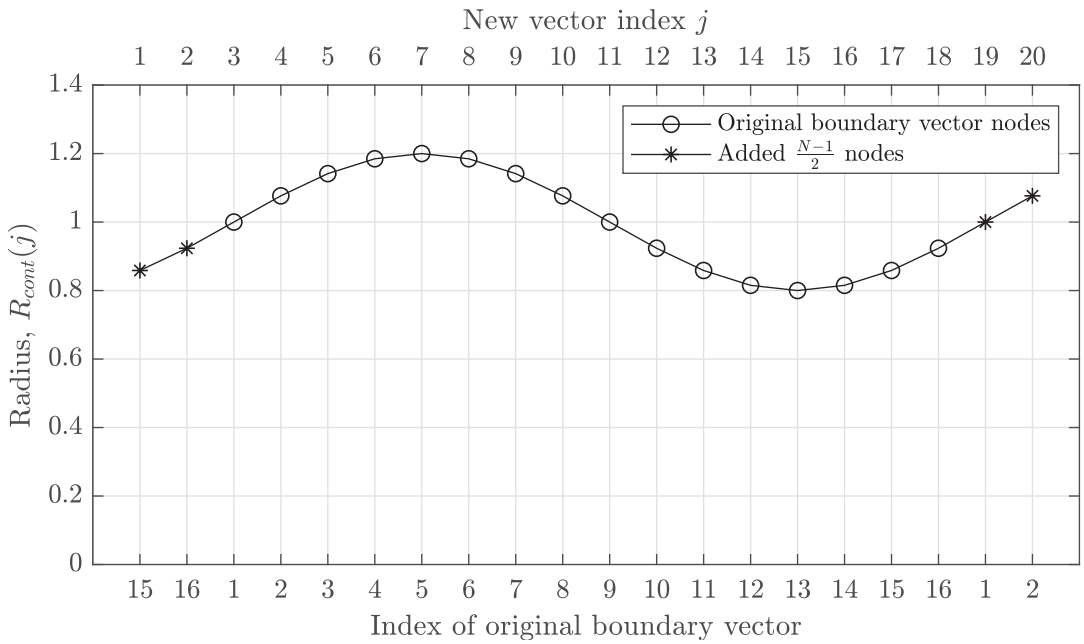

Figure 3.12: Example of how the $\boldsymbol{R}_{cont}$ used in the smoothing is constructed. In this example $N = 5$ and the boundary is made up of 16 nodes.

By using the $\boldsymbol{R}_{cont}$ vector, moving average filtering is successfully calculated with Equation (3.17) on a vector describing a single period of a periodic function.

$$R_{mavg}(j) = \frac{1}{N} \sum_{k=j}^{j+N-1} R_{cont}(k) \tag{3.17}$$

4 Examples

In this chapter different parts of the tool described are showcased. The mapping and stress functions are evaluated for different geometries in an attempt to quantify how well the method performs. Borehole breakouts are simulated for different in-situ stresses and rock properties. The depth and width of the simulated breakouts are then shown.

4.1 Mapping examples

The mapping algorithm was tested with different shapes of triangles, rectangles, tunnel sections, shafts and boreholes with breakouts. As expected the method worked best for smooth geometries described by continuous functions. When the geometry included sharp corners such as those in a square or a triangle the Gibbs phenomena of the Fourier series became evident. The number of terms in the series expansion n_f was as a baseline set to 100 although as few terms as 5 was enough to map a reasonable geometry. Using even more terms than 200 resulted only in small gains on the precision of the mapping.

The mapping goodness of fit was evaluated with the residuals $e(\gamma)$ along the boundary by taking the radius of the mapping versus the radius of the initial geometry as

$$e(\gamma) = r_{\text{map}}(\gamma) - r_{initial}(\gamma) \tag{4.1}$$

To quantify the goodness of fit a few different statistics were calculated, the Mean Error (ME), the Mean Absolute Error (MAE) and the maximum error. To allow goodness of fit comparison between boundaries of different sizes the MAE was normalized by the mean boundary radius, the normalized MAE denote NMAE. The goodness of fit values were calculated as

$$\frac{\sum_{i=1}^{n} e(\gamma_i)}{n} \quad \text{Mean Error (ME)} \tag{4.2}$$

$$\frac{\sum_{i=1}^{n} |e(\gamma_i)|}{n} \quad \text{Mean Absolute Error (MAE)} \tag{4.3}$$

$$\frac{1}{r_{mean}} \frac{\sum_{i=1}^{n} |e(\gamma_i)|}{n} \quad \text{Normalized Mean Absolute Error (NMAE)} \tag{4.4}$$

$$\max\left\{|e(\gamma_1)|, \ldots, |e(\gamma_n)|\right\} \quad \text{Max error} \tag{4.5}$$

Mapping time was also recorded during testing to see how it was affected by different settings. All tests were performed on a personal computer equipped with an 3.3 GHz Intel I7 5820K.

4.1.1 Mapped geometries

To improve readability when referencing different mapping settings in figures and graphs, the "Low settings" represent 256 samples and 25 series terms, the "Medium settings" has 1024 samples and 100 terms and finally the "High settings" uses 4096 samples and 200 terms.

Equilateral triangle

An equilateral triangle has the same length of all its sides and its corners are all 60 degrees. Figure 4.1 shows the mapping with medium and low settings against the original geometry, in Figure 4.2 the residuals between original and mapped geometry are shown.

Although the residuals oscillate around zero it's evident that corners have an impact on accuracy as each of the three corners gives an increased amplitude of the residual oscillation. Table 4.1 shows all tested settings and the results.

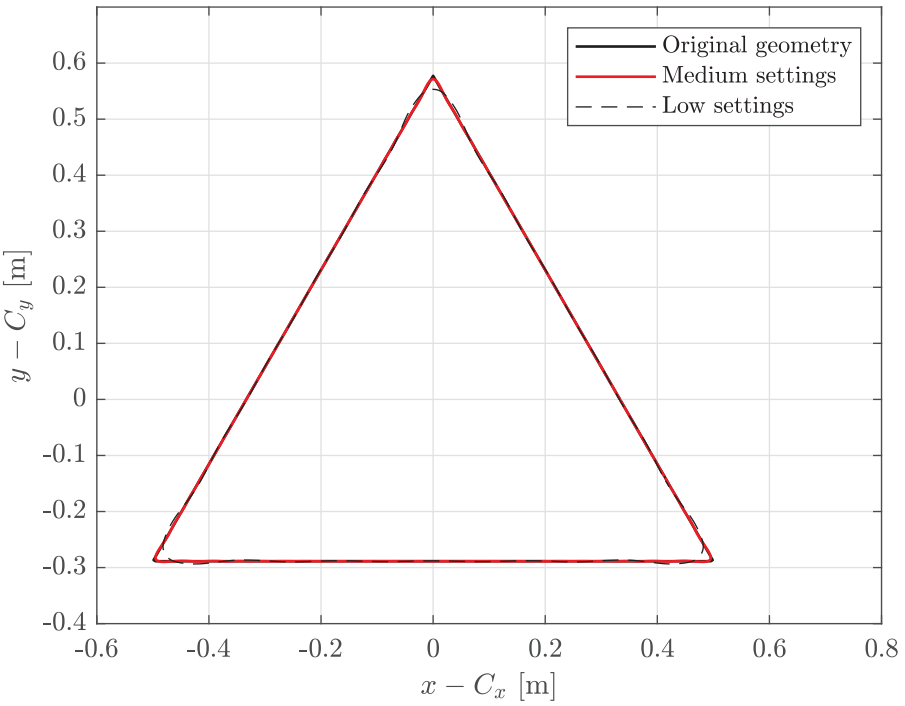

Figure 4.1: Mapping of an equilateral triangle.

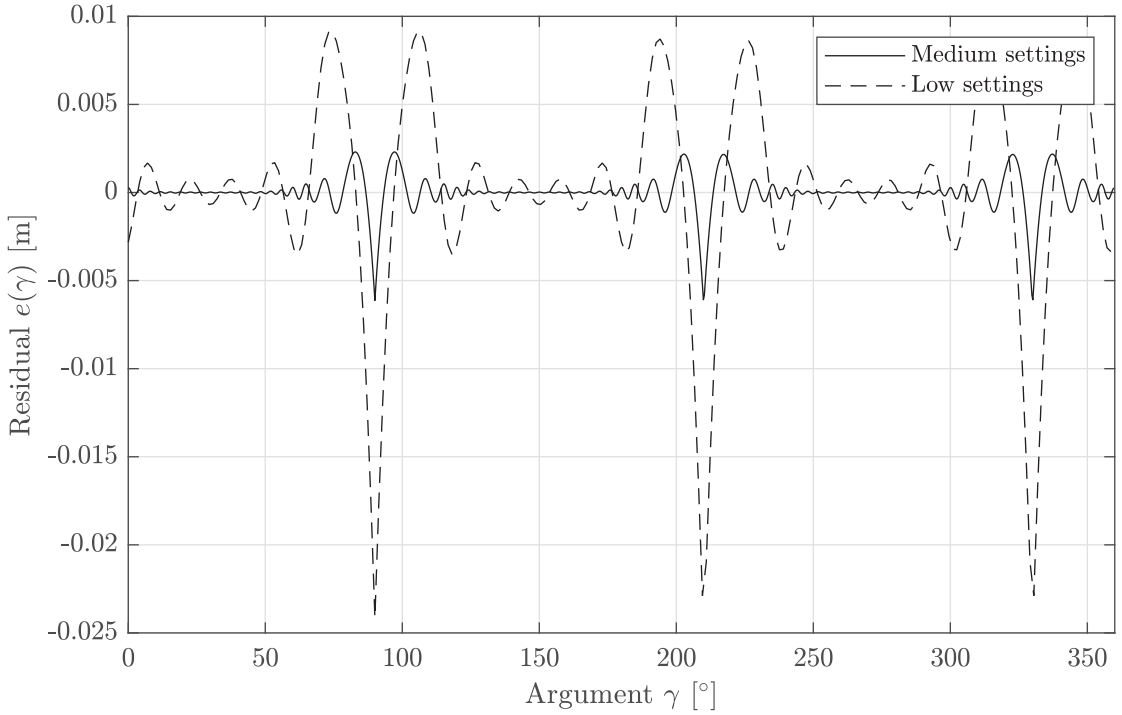

Figure 4.2: Residuals $e(\gamma)$ for the mapping of an equilateral triangle.

Table 4.1: Summarized mapping test results for a equilateral triangle.

Samples n_s	Fourier n_f	Map time [s]	ME [m]	MAE [m]	NMAE [-]	Max error [m]
256	25	1.5	6.89×10^{-5}	3.53×10^{-3}	9.74×10^{-3}	2.41×10^{-2}
256	100	5.7	6.02×10^{-5}	6.05×10^{-4}	1.67×10^{-3}	6.05×10^{-3}
256	200	18.2	-1.43×10^{-5}	1.01×10^{-3}	2.78×10^{-3}	9.11×10^{-3}
1024	25	2.6	4.99×10^{-5}	3.53×10^{-3}	9.72×10^{-3}	2.49×10^{-2}
1024	100	11.9	7.04×10^{-6}	5.15×10^{-4}	1.42×10^{-3}	6.13×10^{-3}
1024	200	31.4	4.94×10^{-6}	1.87×10^{-4}	5.16×10^{-4}	3.07×10^{-3}
4096	25	7.9	4.87×10^{-5}	3.53×10^{-3}	9.72×10^{-3}	2.49×10^{-2}
4096	100	37.0	4.82×10^{-6}	5.14×10^{-4}	1.42×10^{-3}	6.32×10^{-3}
4096	200	88.1	1.77×10^{-6}	1.85×10^{-4}	5.10×10^{-4}	3.17×10^{-3}

Rectangle

A rectangle was also set up for testing, Figure 4.3 shows the geometry and the mapping results, Figure 4.4 shows the residuals. In Table 4.2 results from all tested settings are summarized.

Again, the mapped boundary oscillates around corners. The rectangle geometry also has a larger error than the triangle.

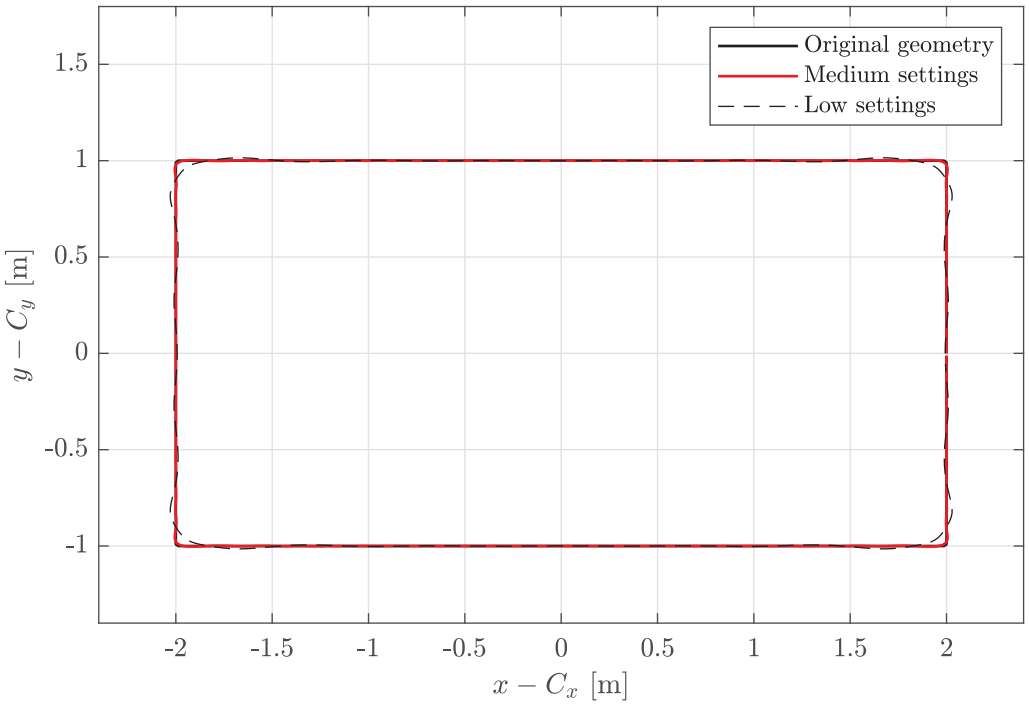

Figure 4.3: Mapping of an rectangle.

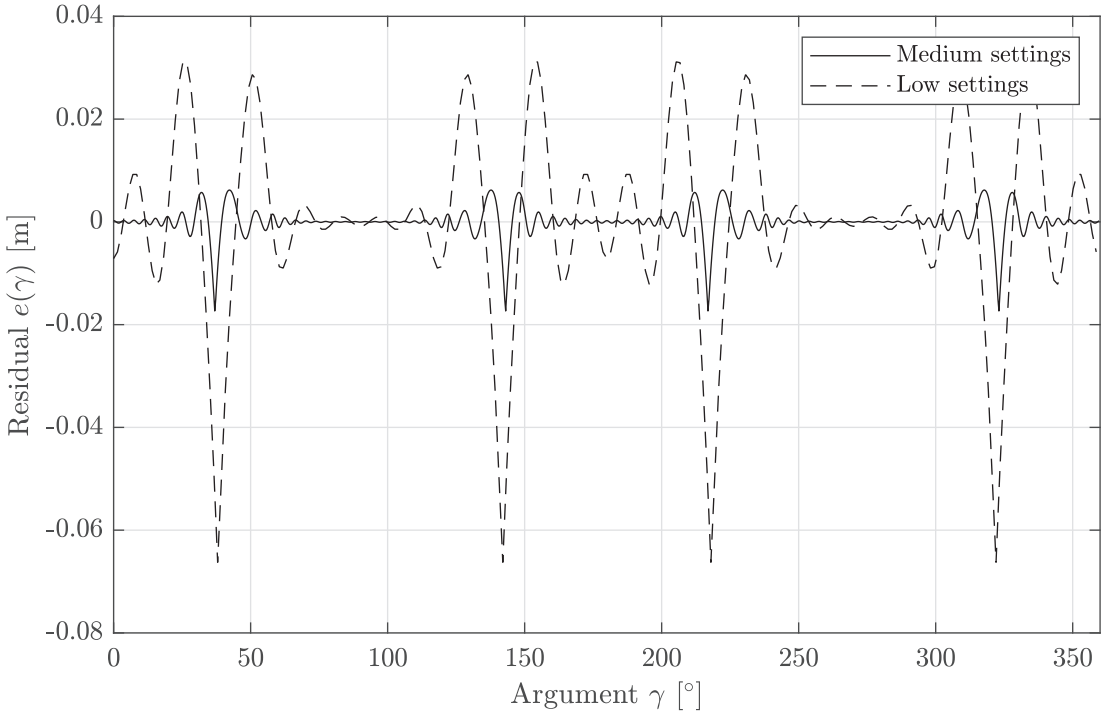

Figure 4.4: Residuals $e(\gamma)$ for the mapping of an rectangle.

Table 4.2: Summarized mapping test results for a rectangle.

Samples n_s	Fourier n_f	Map time [s]	ME [m]	MAE [m]	NMAE [-]	Max error [m]
256	25	1.6	2.00×10^{-4}	1.19×10^{-2}	7.78×10^{-3}	6.63×10^{-2}
256	100	5.8	4.14×10^{-4}	1.76×10^{-3}	1.15×10^{-3}	1.17×10^{-2}
256	200	17.9	1.08×10^{-3}	3.73×10^{-3}	2.43×10^{-3}	1.35×10^{-2}
1024	25	2.7	-9.11×10^{-6}	1.19×10^{-2}	7.74×10^{-3}	6.70×10^{-2}
1024	100	11.6	-1.96×10^{-5}	1.43×10^{-3}	9.32×10^{-4}	1.73×10^{-2}
1024	200	31.9	-2.96×10^{-5}	4.85×10^{-4}	3.17×10^{-4}	8.66×10^{-3}
4096	25	7.8	4.39×10^{-6}	1.19×10^{-2}	7.74×10^{-3}	6.94×10^{-2}
4096	100	37.3	6.51×10^{-6}	1.44×10^{-3}	9.38×10^{-4}	1.73×10^{-2}
4096	200	90.0	2.48×10^{-6}	4.99×10^{-4}	3.26×10^{-4}	8.88×10^{-3}

Smooth shaft

A smooth geometry without sharp corners should give smaller errors, therefore a smooth shaft geometry was designed. The shaft with its mapping results can be seen in Figure 4.5 and the residuals in Figure 4.6. Again, all tested settings are summarized in a table, see Table 4.3.

As both the residuals in Figure 4.6 and Table 4.3 show, the errors are smaller as expected. There are however still some oscillations, mainly near the transitions between the straight lines and the corner arcs. Although it should be noted that the residuals show errors in millimeters, looking at the low settings residuals in Figure 4.6 the error is around 2.5 mm at the most.

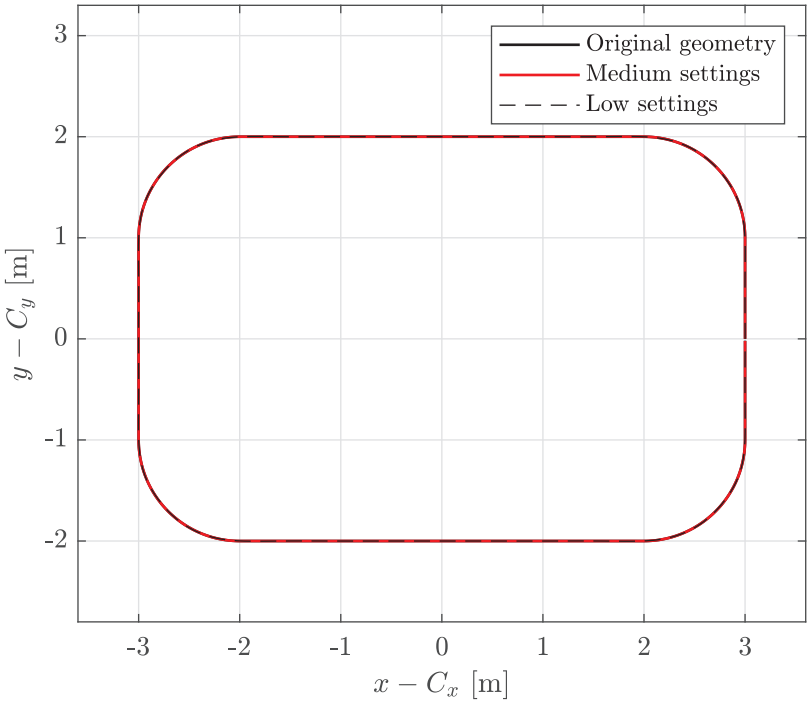

Figure 4.5: Mapping of a shaft with smooth corners.

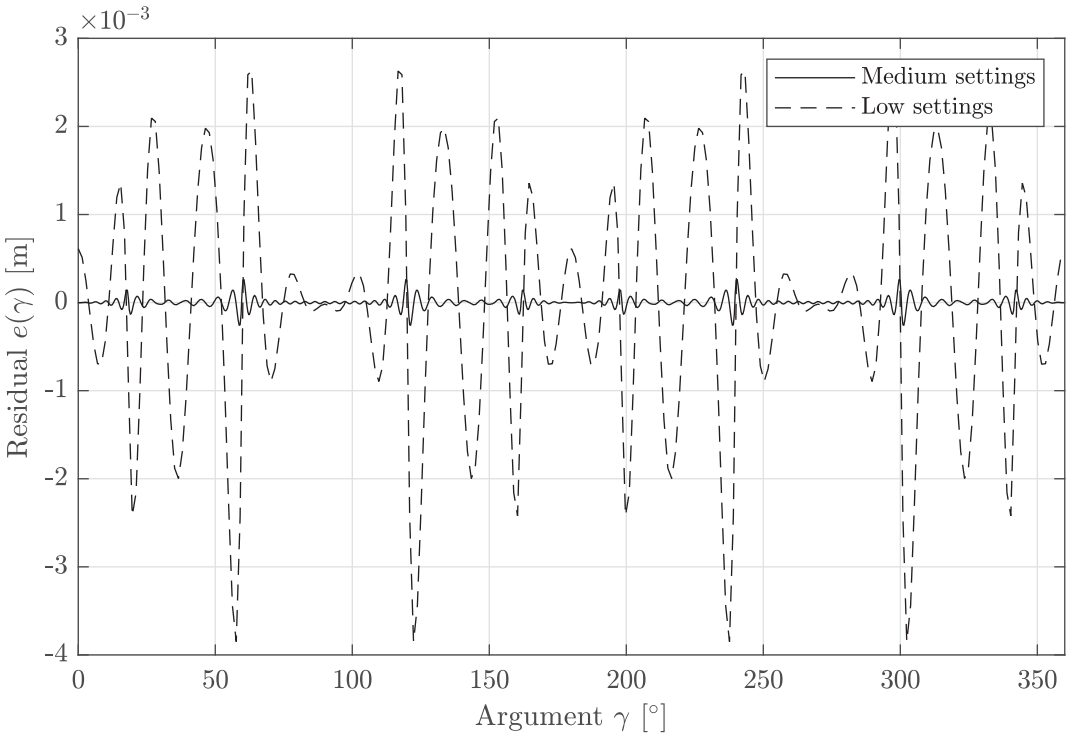

Figure 4.6: Residuals $e(\gamma)$ for the mapping of a smooth shaft.

Table 4.3: Summarized mapping test results for a smooth shaft.

Samples n_s	Fourier n_f	Map time [s]	ME [m]	MAE [m]	NMAE [-]	Max error [m]
256	25	1.3	-5.42×10^{-6}	1.05×10^{-3}	3.94×10^{-4}	3.85×10^{-3}
256	100	4.8	-1.47×10^{-6}	3.34×10^{-5}	1.25×10^{-5}	3.13×10^{-4}
256	200	15.6	-1.55×10^{-5}	2.18×10^{-4}	8.14×10^{-5}	9.60×10^{-4}
1024	25	2.4	-4.18×10^{-6}	1.05×10^{-3}	3.91×10^{-4}	3.87×10^{-3}
1024	100	10.1	-1.20×10^{-7}	3.37×10^{-5}	1.26×10^{-5}	2.61×10^{-4}
1024	200	23.9	-1.15×10^{-7}	5.15×10^{-6}	1.92×10^{-6}	6.19×10^{-5}
4096	25	6.9	-4.14×10^{-6}	1.05×10^{-3}	3.91×10^{-4}	3.87×10^{-3}
4096	100	32.7	-6.61×10^{-8}	3.34×10^{-5}	1.25×10^{-5}	2.71×10^{-4}
4096	200	80.6	-5.67×10^{-8}	5.11×10^{-6}	1.91×10^{-6}	6.68×10^{-5}

Asymmetric tunnel shape

When attempting to map a more complex geometry, an asymmetrical tunnel was drawn with several different curved segments of different radii. See Figure 4.7 for the geometry with its base and low setting mappings and Figure 4.8 for the corresponding residuals. As with all previous geometries the results are also summarized, see Table 4.4.

The geometry was designed to have smooth transitions between the curved segments. As a result, residual errors are quite small with the exception of the surroundings of the two sharp corners at the tunnel floor.

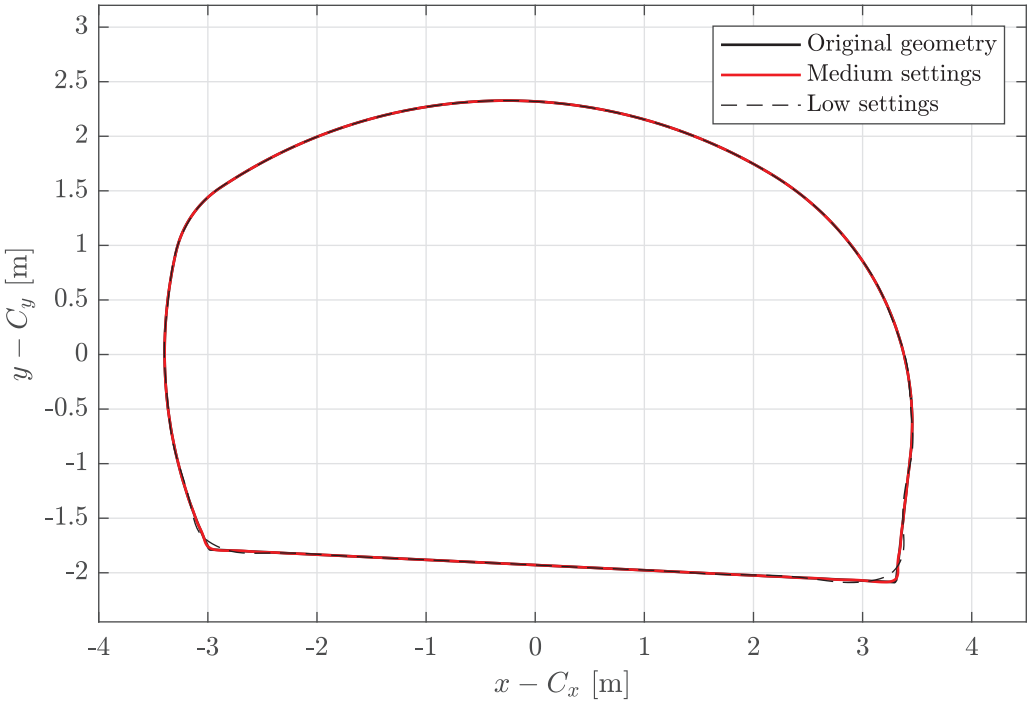

Figure 4.7: Mapping of an asymmetric tunnel.

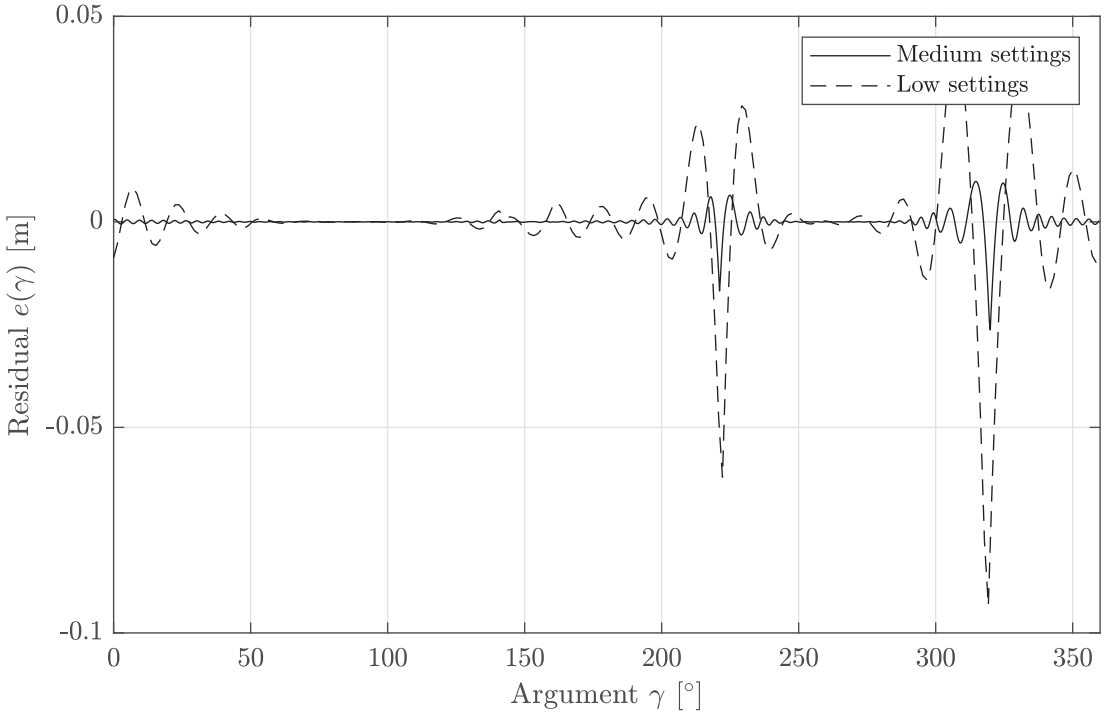

Figure 4.8: Residuals $e(\gamma)$ for the mapping of a asymmetric tunnel.

Table 4.4: Summarized mapping test results for a asymmetric tunnel.

Samples n_s	Fourier n_f	Map time [s]	ME [m]	MAE [m]	NMAE [-]	Max error [m]
256	25	1.3	2.63×10^{-4}	6.99×10^{-3}	2.51×10^{-3}	9.34×10^{-2}
256	100	4.7	4.00×10^{-4}	1.26×10^{-3}	4.51×10^{-4}	1.69×10^{-2}
256	200	15.7	3.98×10^{-4}	3.15×10^{-3}	1.13×10^{-3}	2.12×10^{-2}
1024	25	2.7	3.81×10^{-5}	6.92×10^{-3}	2.49×10^{-3}	1.03×10^{-1}
1024	100	10.6	5.00×10^{-6}	8.86×10^{-4}	3.18×10^{-4}	2.63×10^{-2}
1024	200	29.2	3.69×10^{-6}	3.05×10^{-4}	1.10×10^{-4}	1.20×10^{-2}
4096	25	6.9	3.73×10^{-5}	6.92×10^{-3}	2.49×10^{-3}	1.05×10^{-1}
4096	100	32.3	4.23×10^{-6}	8.86×10^{-4}	3.18×10^{-4}	2.76×10^{-2}
4096	200	78.4	1.85×10^{-6}	3.04×10^{-4}	1.09×10^{-4}	1.38×10^{-2}

Measured borehole with breakouts

Before proceeding to other tests, the mapping of a borehole with breakouts was evaluated. The borehole geometry used in the test is extracted from Haimson's photo of experimental borehole breakouts shown in Figure 2.12 (a). From Haimson's photo a boundary outlining the borehole wall was generated in MATLAB as shown in Figure 4.9.

With a generated polygon to work with, the same tests as previously shown were carried out, see Figure 4.10, Figure 4.11 and Table 4.5.

Although the residuals seem to show very small errors, it should be noted that the geometry itself is small with an diameter of about 20 mm. When looking at the NMAE it shows that the mapping is on par with the triangle or rectangle previously shown. One reason are the sharp tips of the breakouts but some of the error accumulates from around the geometry due to the roughness of the polygon that was created from the photo.

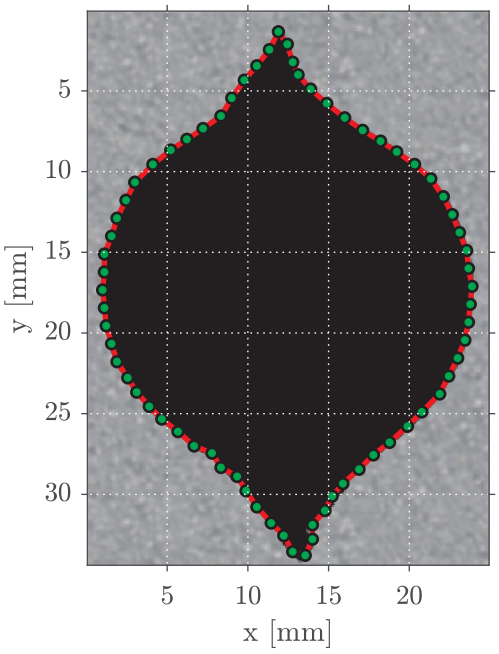

Figure 4.9: A geometry of a borehole with breakouts generated from a photo by Haimson (2007). The green dots mark polygon vertices obtained from the photo and the red line shows the boundary of the geometry used in the mapping.

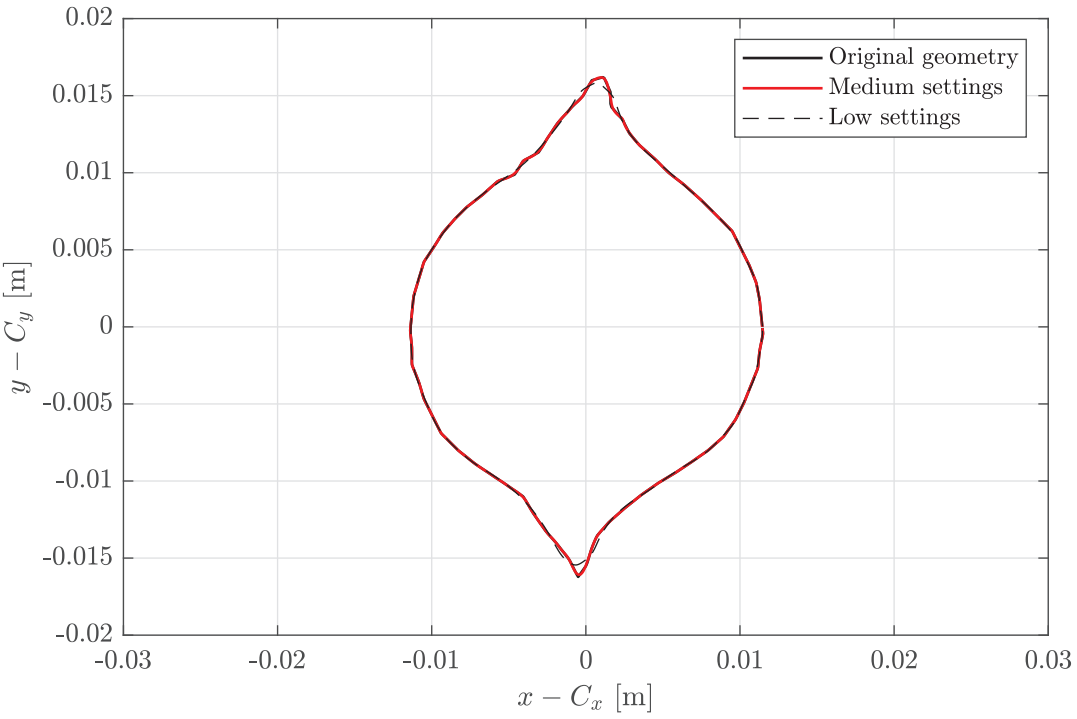

Figure 4.10: Mapping of a measured borehole with breakouts.

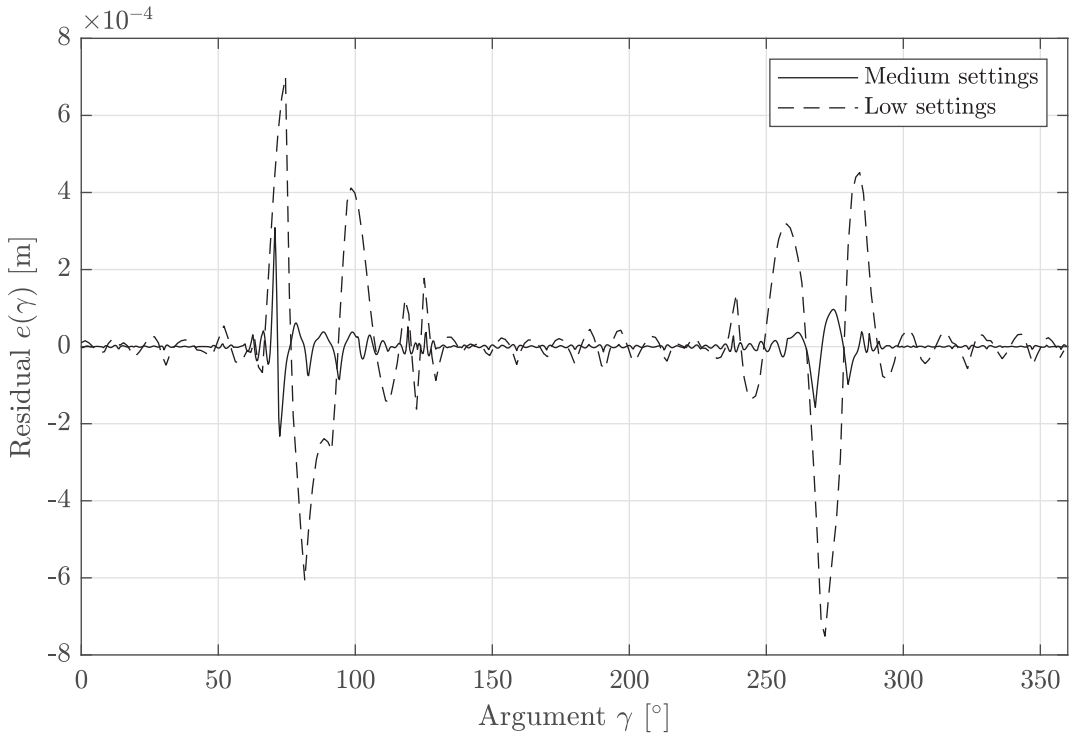

Figure 4.11: Residuals $e(\gamma)$ for the mapping of a measured borehole with breakouts.

Table 4.5: Summarized mapping test results for a measured borehole with breakouts.

Samples n_s	Fourier n_f	Map time [s]	ME [m]	MAE [m]	NMAE [-]	Max error [m]
256	25	1.5	2.52×10^{-6}	9.32×10^{-5}	7.93×10^{-3}	7.52×10^{-4}
256	100	4.8	3.41×10^{-6}	1.28×10^{-5}	1.09×10^{-3}	2.95×10^{-4}
256	200	15.9	1.12×10^{-6}	2.45×10^{-5}	2.08×10^{-3}	2.63×10^{-4}
1024	25	2.4	8.86×10^{-7}	9.39×10^{-5}	7.99×10^{-3}	8.06×10^{-4}
1024	100	10.6	2.41×10^{-7}	1.19×10^{-5}	1.01×10^{-3}	3.09×10^{-4}
1024	200	28.8	1.48×10^{-7}	6.08×10^{-6}	5.18×10^{-4}	2.37×10^{-4}
4096	25	6.3	8.10×10^{-7}	9.39×10^{-5}	7.99×10^{-3}	8.15×10^{-4}
4096	100	28.4	1.15×10^{-7}	1.19×10^{-5}	1.01×10^{-3}	3.07×10^{-4}
4096	200	83.1	-2.83×10^{-8}	5.98×10^{-6}	5.09×10^{-4}	2.37×10^{-4}

4.1.2 Effect of corners

Since it was evident that sharp corners had an effect on precision of the mapping, an additional geometry made up of a circular segment and two circular tangent segments was used to test how well the mapping could fit corners of different angles α. In Figure 4.12 an example of the geometry is given.

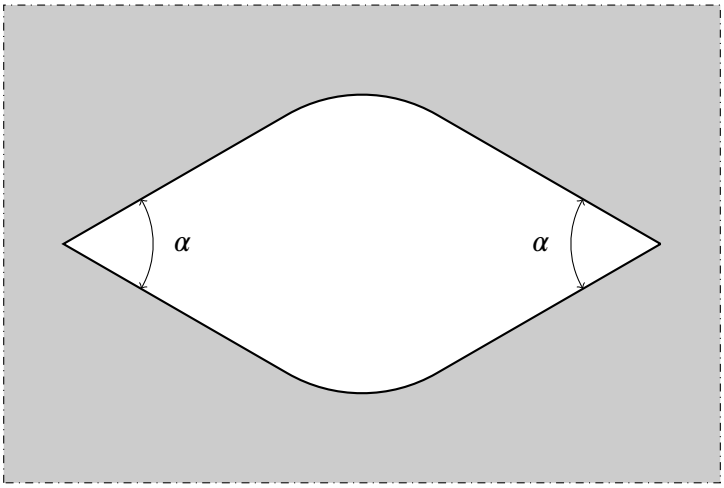

Figure 4.12: Four straight lines and two circle segments making up a smooth geometry with the exception of two corners with angles α. As α increases towards 180 degrees the geometry looks more and more like a normal circle.

Corner angles between 20 and 160 degrees was tested, results for the different corners are shown in Table 4.6. When attempting to map the geometry with corners below 20 degrees the mapping failed as can be seen in Figure 4.13 where a the mapping of a 15 degree corner geometry was attempted.

Table 4.6: Table showing mapping statistics for different corner angles. Mapping was evaluated with 100 coefficients and 1024 samples.

Corner angle α [°]	Map time [s]	ME [m]	MAE [m]	NMAE [-]	Max error [m]
20	9.9	1.59×10^{-3}	2.44×10^{-2}	1.47×10^{-2}	1.98×10^{-1}
40	9.8	2.31×10^{-4}	4.19×10^{-3}	3.16×10^{-3}	4.89×10^{-2}
60	9.9	6.55×10^{-5}	1.33×10^{-3}	1.14×10^{-3}	2.11×10^{-2}
80	9.8	2.25×10^{-5}	5.25×10^{-4}	4.83×10^{-4}	1.12×10^{-2}
100	9.7	9.05×10^{-6}	2.34×10^{-4}	2.25×10^{-4}	6.75×10^{-3}
120	9.7	2.96×10^{-6}	1.11×10^{-4}	1.09×10^{-4}	4.01×10^{-3}
140	10.0	1.13×10^{-6}	4.55×10^{-5}	4.53×10^{-5}	2.45×10^{-3}
160	9.8	2.55×10^{-8}	1.18×10^{-5}	1.18×10^{-5}	9.72×10^{-4}

As expected the sharper the corner the larger the error. Increasing the number of samples and series terms allows to map somewhat sharper corners as the graphs in Figure 4.14 show. However, when going below 60 degree corners even a high number of samples and series terms cannot keep the maximum error from increasing.

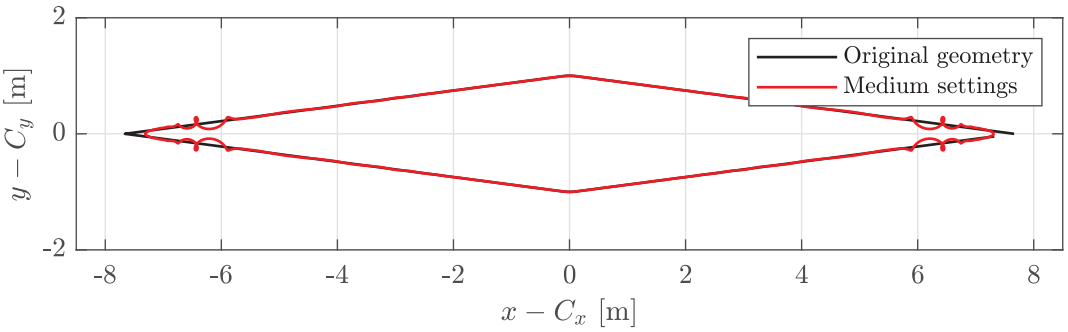

Figure 4.13: Mapping the test geometry with two 15 degree corners returned a visibly distorted result.

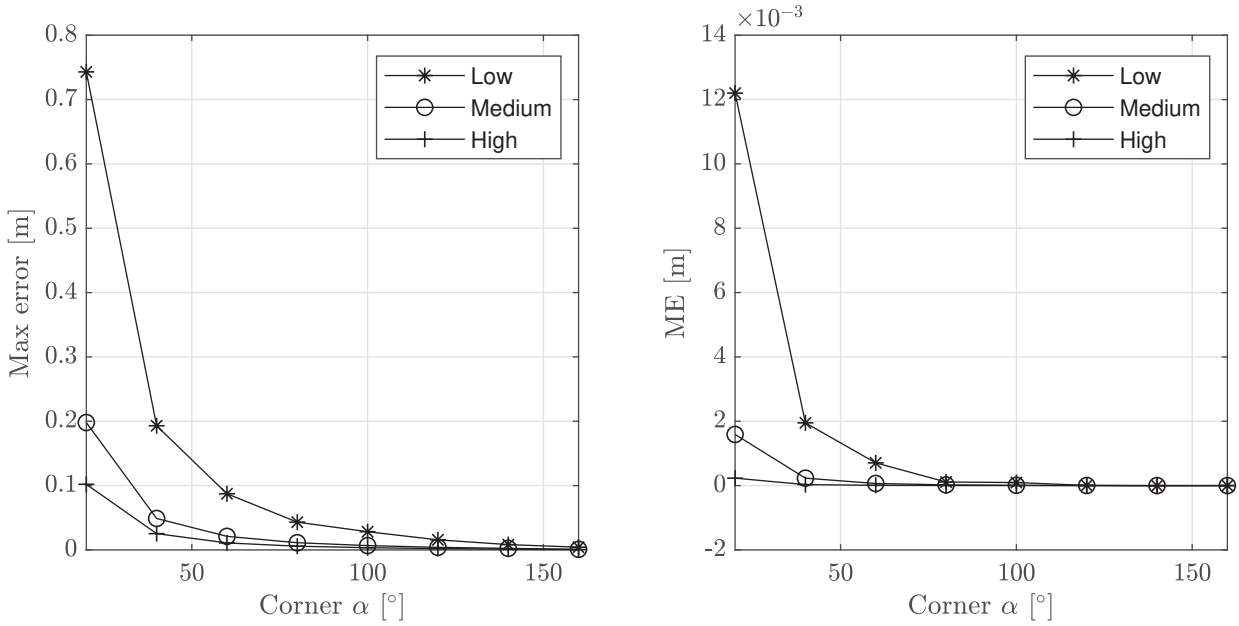

(a) Max error

(b) Mean error

Figure 4.14: Corner angles versus maximum and mean error.

4.1.3 Effect of number of series terms

While testing the equilateral triangle geometry shown in Figure 4.1 the effect of number of series terms used in the mapping was investigated for 10 to 200 terms. This was repeated for 256, 1024 and 4096 samples. In Figure 4.15 the maximum and mean error versus series terms are presented.

When using a too low number of samples, the number of terms will not stabilize the mean error around 0 as it should be for a sinusoidal curve. It also seems that there are only marginal gains going above a certain number of samples, at least when viewing maximum and mean error for 256, 1024 and 4096 samples.

In Figure 4.16 the mapping time versus number of terms is plotted. Except a few bumps in the curve the mapping time seems to be linear against number of terms. The bumps seen could be the result of some program running in the background on the machine that performed the tests.

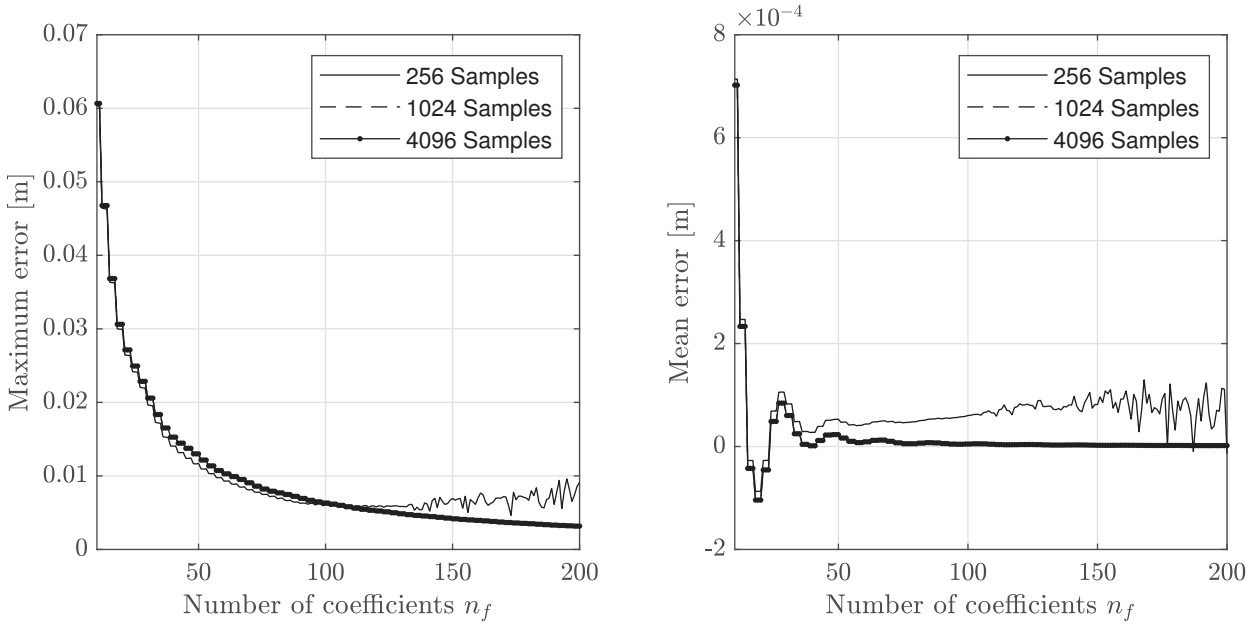

(a) Max error

(b) Mean error

Figure 4.15: Number of series terms versus maximum and mean error. The differences between different number of samples are very small, especially so between 1024 and 4096 samples which make them hard to distinguish between in this Figure. For the Max error in (a), 4096 samples has the largest error at start but the smallest at the end, whilst 256 samples has the lowest error at start and the largest error at the end. For the Mean error in (b), 4096 samples has the lowest mean error throughout the range of series terms and 256 samples the highest mean error.

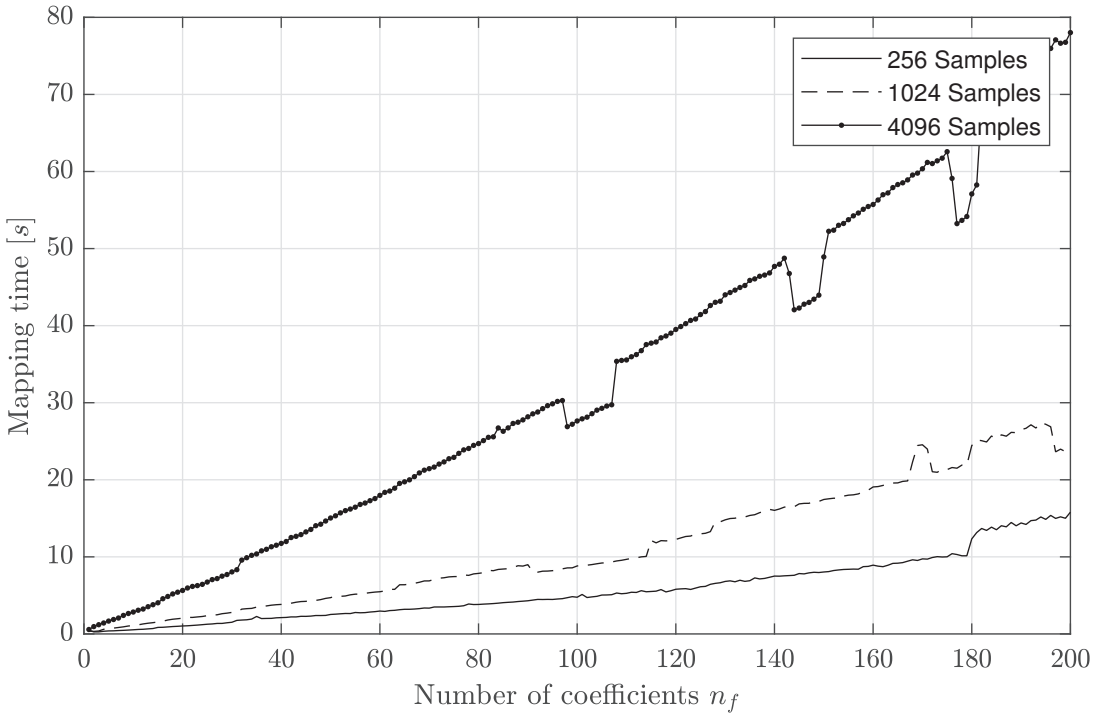

Figure 4.16: Number of series terms versus mapping time.

4.1.4 Effect of number of samples

Similarly to testing the effect of series terms with the equilateral triangle geometry shown in Figure 4.1, the geometry was also used to test the effect of number of samples. Sample sizes to test were chosen as 2^n where $n = 5$ to $n = 12$. This means that the sample numbers range from 32 to 4096. The different sample sizes were tested with series terms of 25, 100 and 200. Again, the maximum and mean error are presented, this time against the number of samples in Figure 4.17.

Generally, error rapidly decline down to a certain point when increasing samples. However, a higher number of series terms requires more samples before the error gain per increased sample is close to zero. Regarding mapping time it is the same as with the number of series terms, mapping time is close to linear when the number of samples increases, see Figure 4.18.

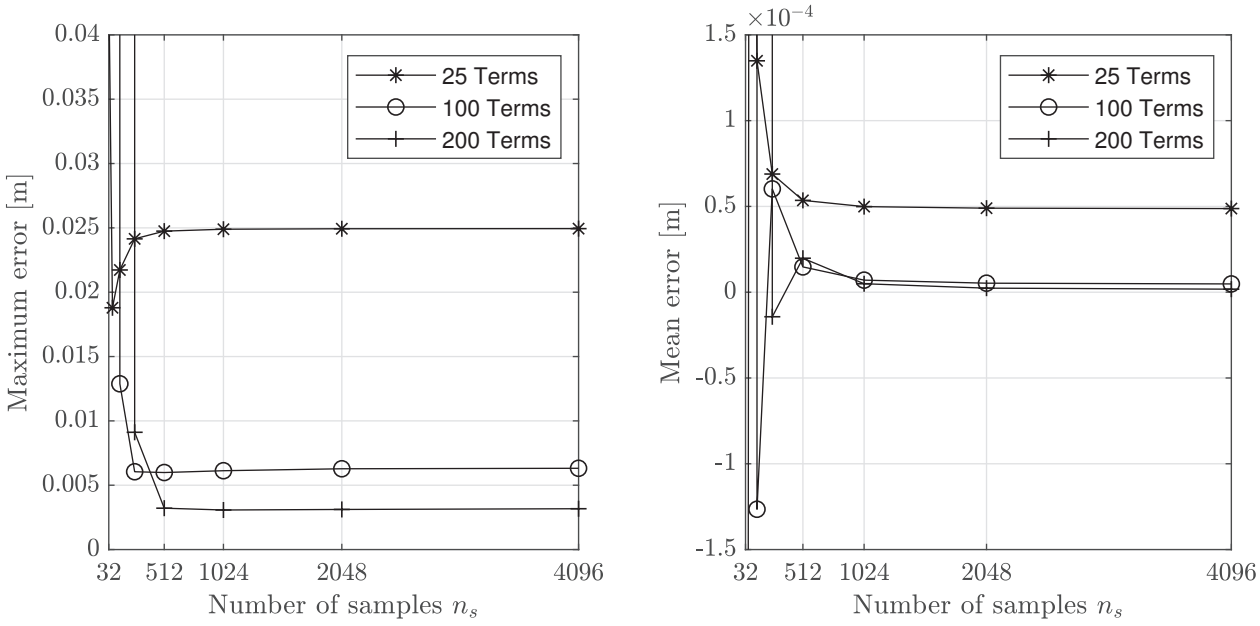

(a) Max error

(b) Mean error

Figure 4.17: Number of samples versus maximum and mean error.

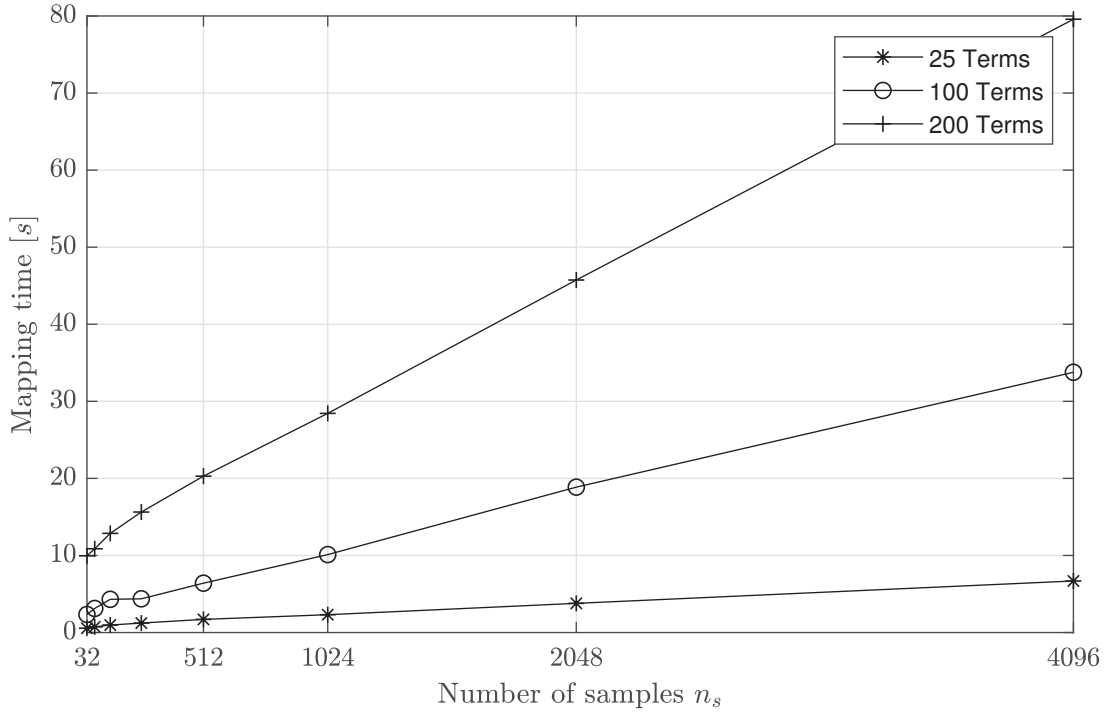

Figure 4.18: Number of samples versus mapping time.

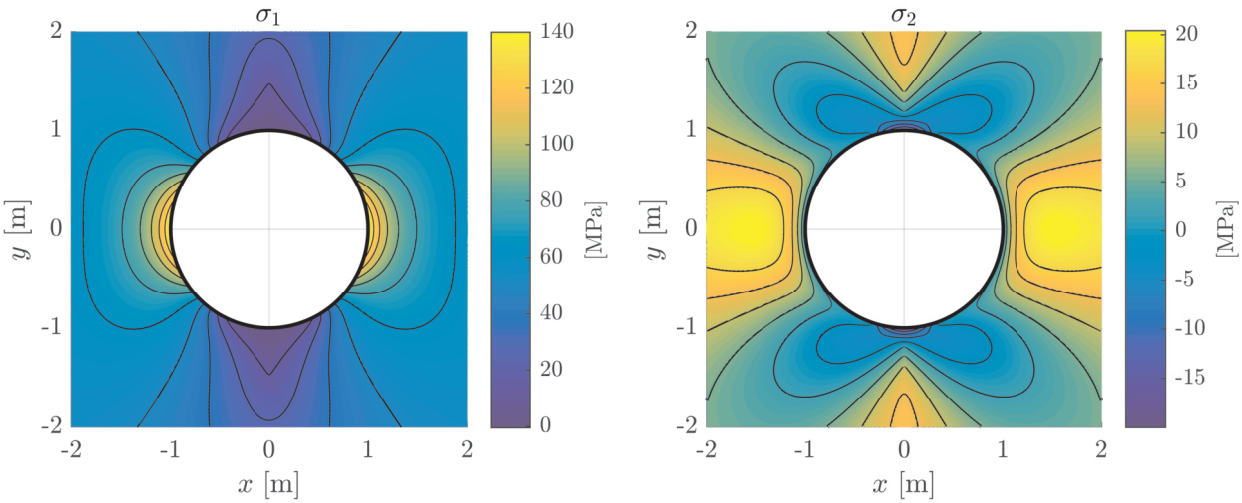

Figure 4.19: Stresses around a borehole with the medium settings.

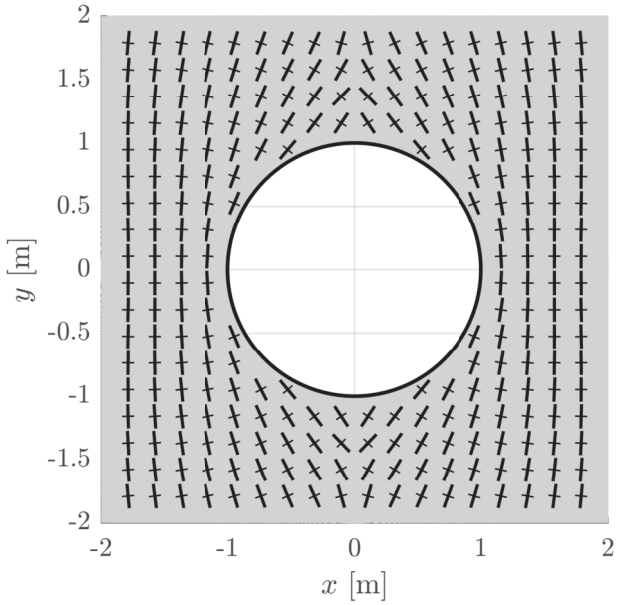

Figure 4.20: Direction of principal stresses around borehole.

4.2 Stress function examples

To evaluate how well the method worked secondary stresses were calculated for a few different geometries and compared to results of other methods. A circular hole was compared to the Kirsch solution and the asymmetric tunnel from the previous section compared to a Finite Element Analysis (FEA).

4.2.1 Borehole comparison to the Kirsch solution

Secondary stresses around a circular borehole were evaluated with the "Medium" mapping settings. When discussing the Kirsch solution, in-situ stresses are set to relate by a factor of 5 as $\sigma_H = 5 \cdot \sigma_h$, where $\sigma_H = 50$ MPa. The resulting principal stresses are shown in Figure 4.19 and the direction of principal stresses shown in Figure 4.20.

When comparing the principal stresses in Figure 4.19 to the ones produced by Kirsch's solution in Figure 2.16 they seem to be almost identical. To verify that the solutions in fact yield the same results, the residual between the principal stresses determined by the conformal mapping method and the ones determined by the Kirsch's solution are calculated. This procedure is repeated for the "Low", "Medium" and "High" mapping settings, see Figures 4.21 to 4.23.

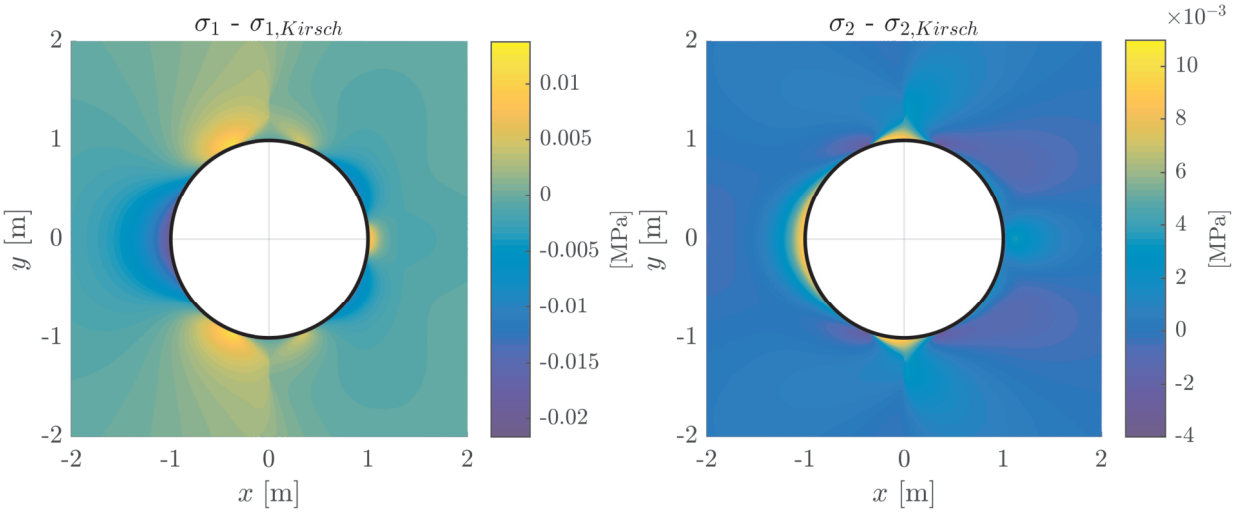

Figure 4.21: Comparing "Low" setting mapping solution to Kirsch for stresses around a circular borehole.

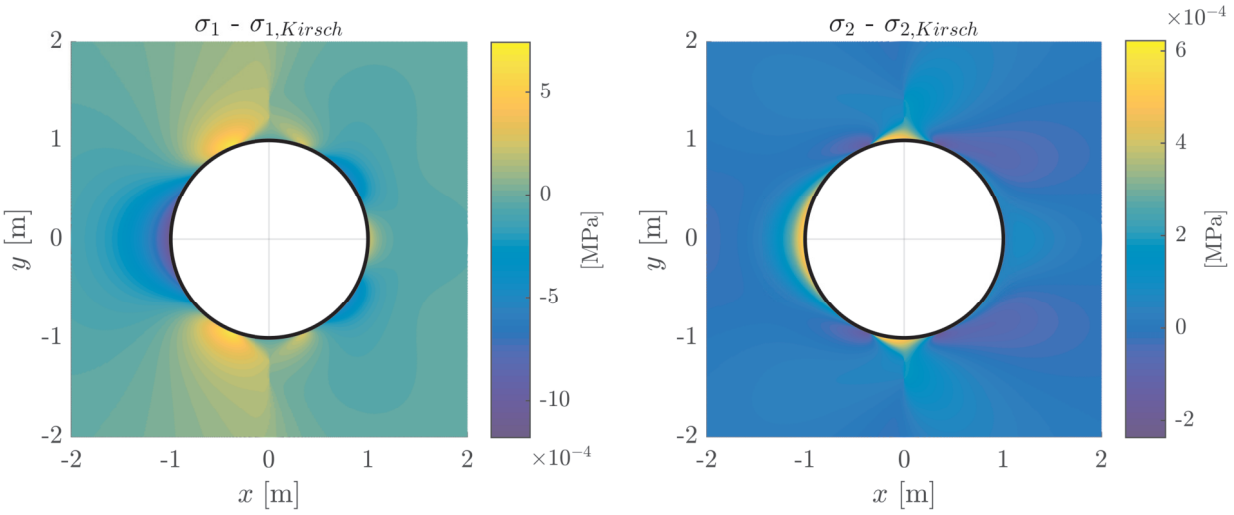

Figure 4.22: Comparing "Medium" setting mapping solution to Kirsch for stresses around a circular borehole.

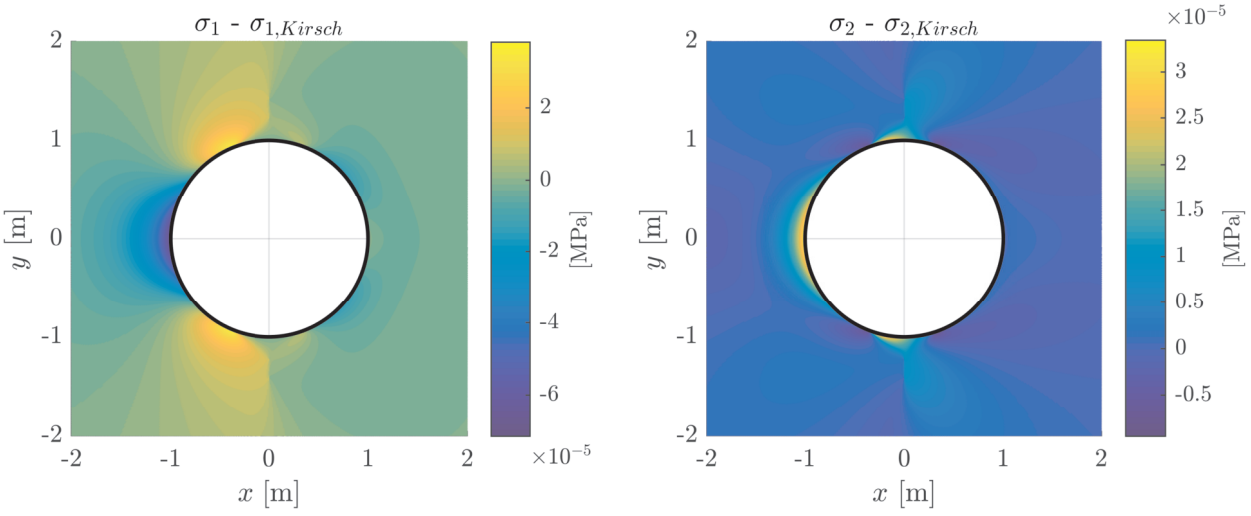

Figure 4.23: Comparing "High" setting mapping solution to Kirsch for stresses around a circular borehole.

4.2.2 Asymmetric tunnel comparison to finite element analysis

To test the method with a more complex geometry, the asymmetric tunnel from the previous section was chosen. The in-situ stresses are again set to relate by a factor of 5 as $\sigma_H = 5 \cdot \sigma_h$, where $\sigma_H = 50$ MPa. In Figure 4.24 the secondary stresses are shown when using the "Low" mapping settings, Figure 4.25 shows the directions of principal stresses. However, it came to attention after these tests that the provided code was not adapted for asymmetric geometries, which explains the large errors the test demonstrated. Nonetheless, the result of the tests are still kept to show what errors might occur if using an asymmetric geometry.

Using the MATLAB® Partial Differential Equation Toolbox™ by MathWorks® (2019) a simple Finite Element Analysis (FEA) was programmed to enable comparison with any arbitrary geometry evaluated in the tool. The Finite Element Model (FEM) was setup as shown in Figure 4.26. Some differences in the results were to be expected since the FEM uses modulus of elasticity and Poisson's ratio for determining strains from which the stress field is derived. The region is also finite and not infinite as in the conformal mapping solution. However, the general idea was to have something to compare against when evaluating arbitrary regions without a simple analytic solution such as the asymmetric tunnel shape.

To verify that the FEM produced somewhat similar results to an analytic solution, it was first compared to the Kirsch's solution of a circular hole. In Figure 4.27 the FEM and Kirsch solutions are compared, the modulus of elasticity was set to 73 GPa and the Poisson's ratio set to 0.

As can be seen in Figure 4.27 the FEM differs about ± 0.04 MPa to the Kirsch solution. The FEM was deemed to be precise enough for using as a comparison to the conformal mapping model results of the asymmetric tunnel. The test was run again, this time comparing the conformal mapping solution of stresses around the asymmetric tunnel and the FEM, see Figure 4.28.

The models differs in the scale of many MPa overall, but in proximity to the corners and the floor there are larger discrepancies where the error reaches well above 10 MPa. Neither the FEM nor the conformal mapping model are good at dealing with corners. The extreme stresses in the corner region do however stem from the conformal mapping solution. When attempting to raise the sampling and mapping settings, fluctuations in the stress surface decrease but the error from the corners is even larger, see Figure 4.29.

Oscillations in the stress surface compared to the FEM are visible in Figure 4.28 and Figure 4.29, to visualize the difference between all three stress surfaces, the hoop stresses were plotted. See Figure 4.30 for the major principal stress and Figure 4.31 for the minor principal stress, both Figures show stresses of the FEM, the "Low" mapping and the "High" mapping solutions plotted against angular location at the boundary.

The comparison visualizes the oscillations, in the "Low" mapping solution it is evident, in the "High" mapping solution it looks more like high frequency noise at this level of zoom. Especially the "High" mapping solution spikes at the corners although the low mapping solution and FEM does so as well. The mapping solutions generally track the FEM quite well, except at a few angular intervals, mainly in the minor principal stresses.

To also investigate if any boundary distortions can account for some of the differences between the models, the test was run again but using the mapped and oscillating boundary in the FEA, see Figure 4.32. This procedure seemed to have no impact on the resulting errors.

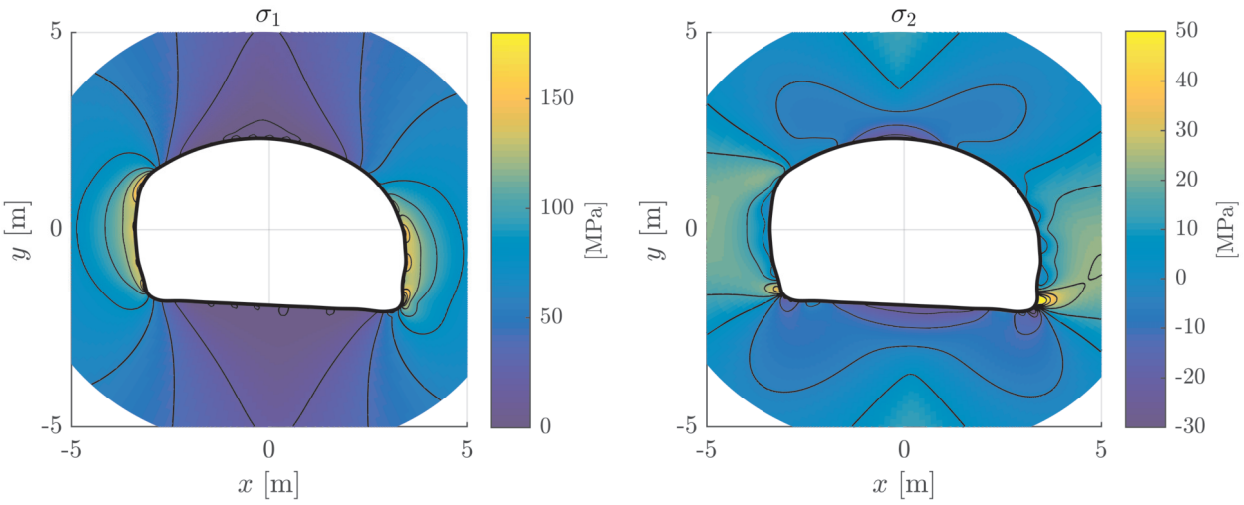

Figure 4.24: Stresses surrounding asymmetric tunnel "Low" settings

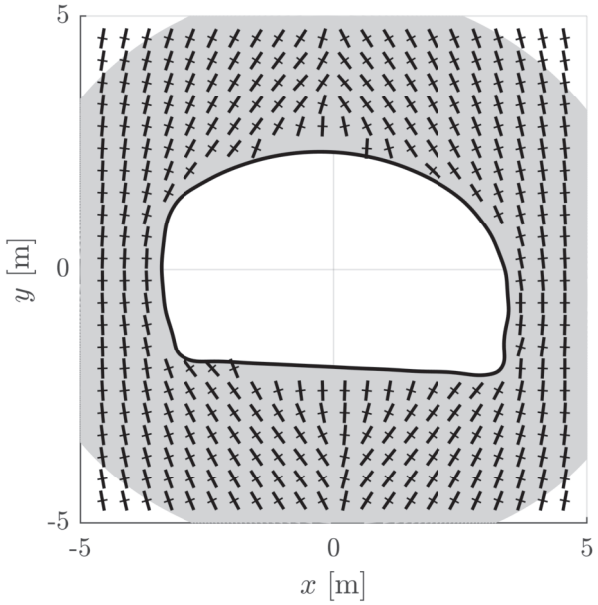

Figure 4.25: Direction of principal stresses surrounding the asymmetric tunnel using the "Low" mapping settings.

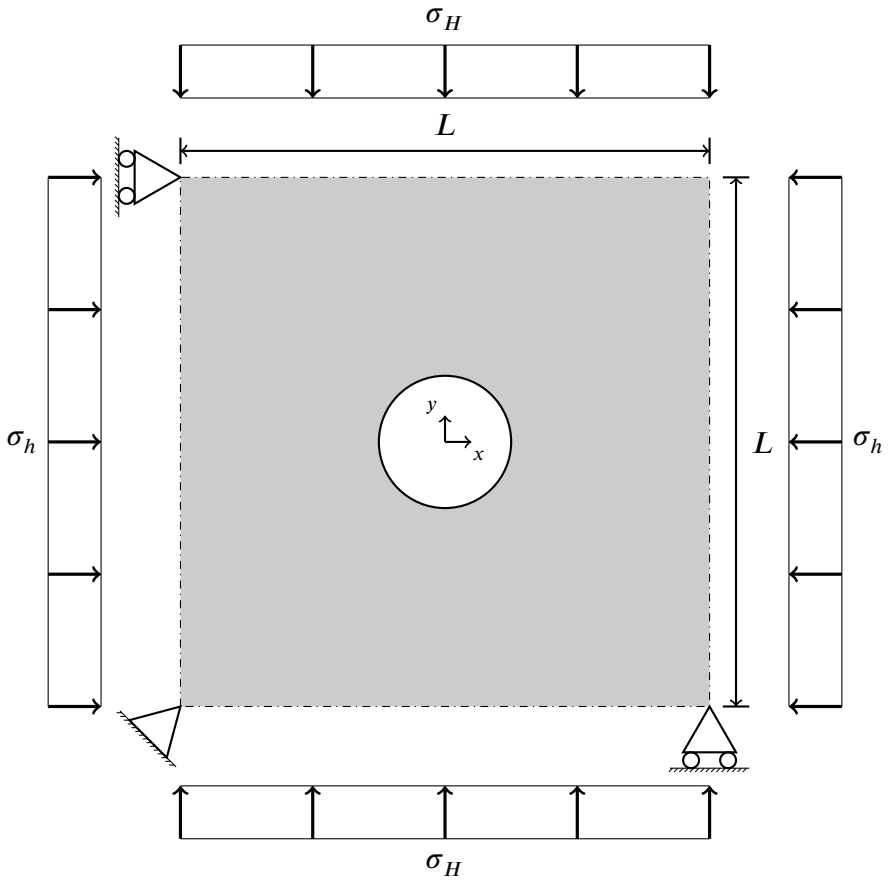

Figure 4.26: Conceptual setup of the finite element model. The length L was set to 160 times the maximum sampled boundary radius.

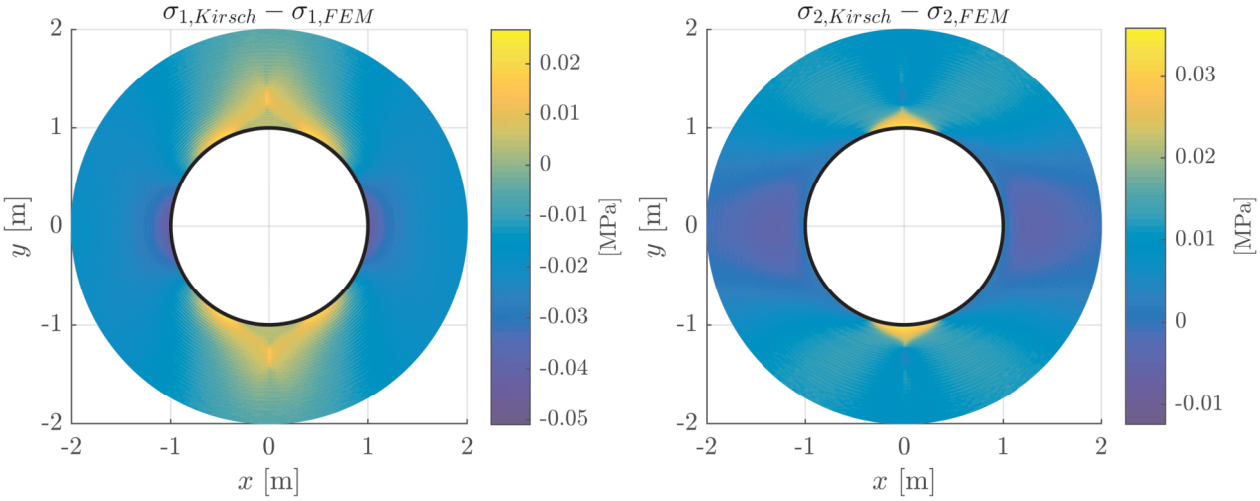

Figure 4.27: Comparing the Kirsch solution to the FEA for stresses around a circular borehole.

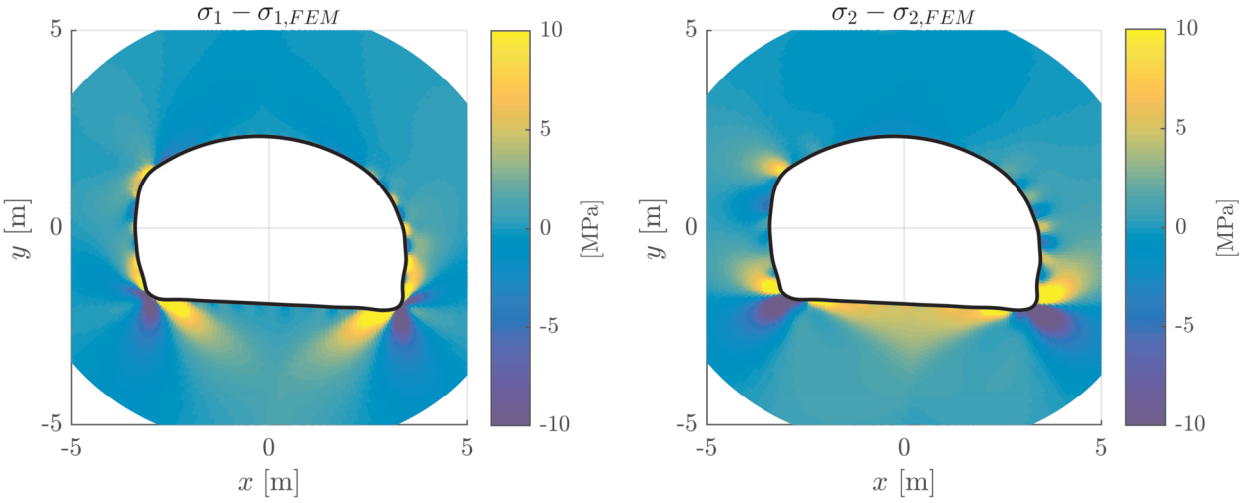

Figure 4.28: Comparing conformal mapping solution with "Low" mapping settings to the FEM for principal stresses around a asymmetric tunnel.

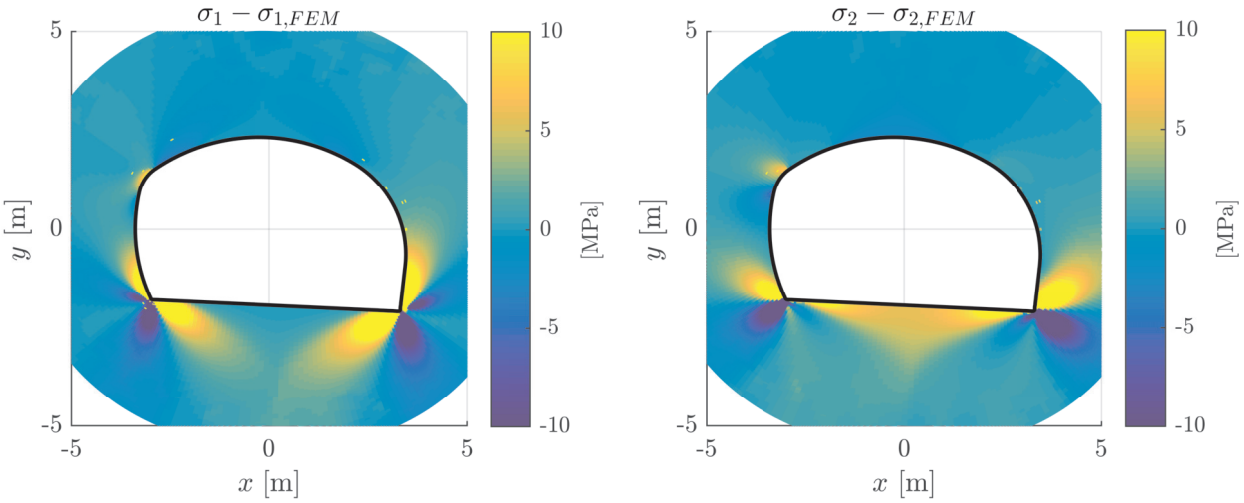

Figure 4.29: Comparing conformal mapping solution with high mapping settings to the FEM for principal stresses around a asymmetric tunnel.

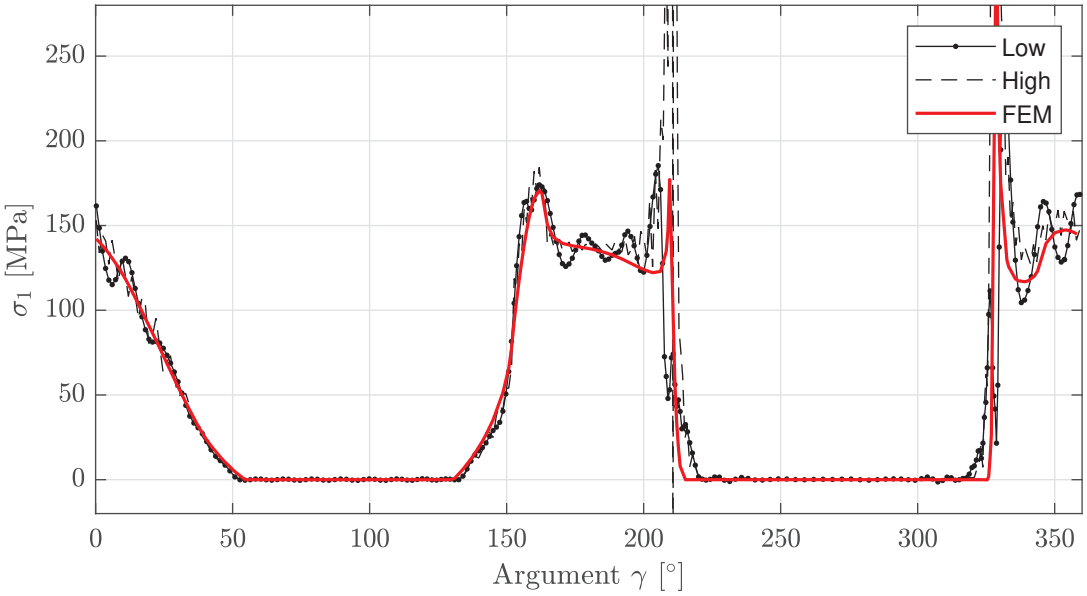

Figure 4.30: Comparing major principal boundary stress between the FEM, "Low" and "High" conformal mapping solutions. The y-axis is cropped to make small oscillations more visible.

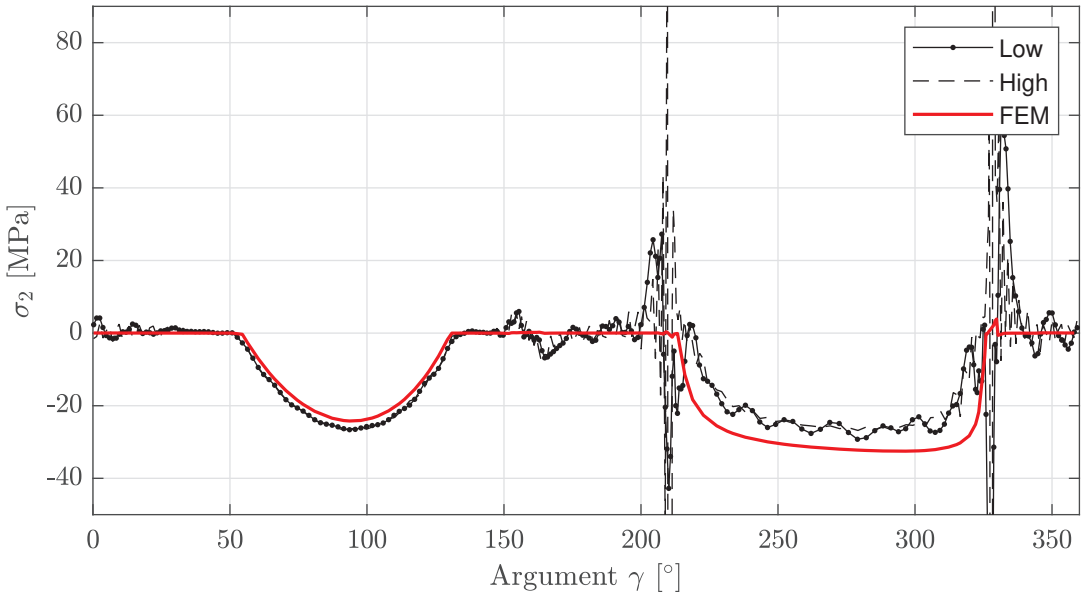

Figure 4.31: Comparing minor principal boundary stress between the FEM, "Low" and "High" conformal mapping solutions. The y-axis is cropped to make small oscillations more visible.

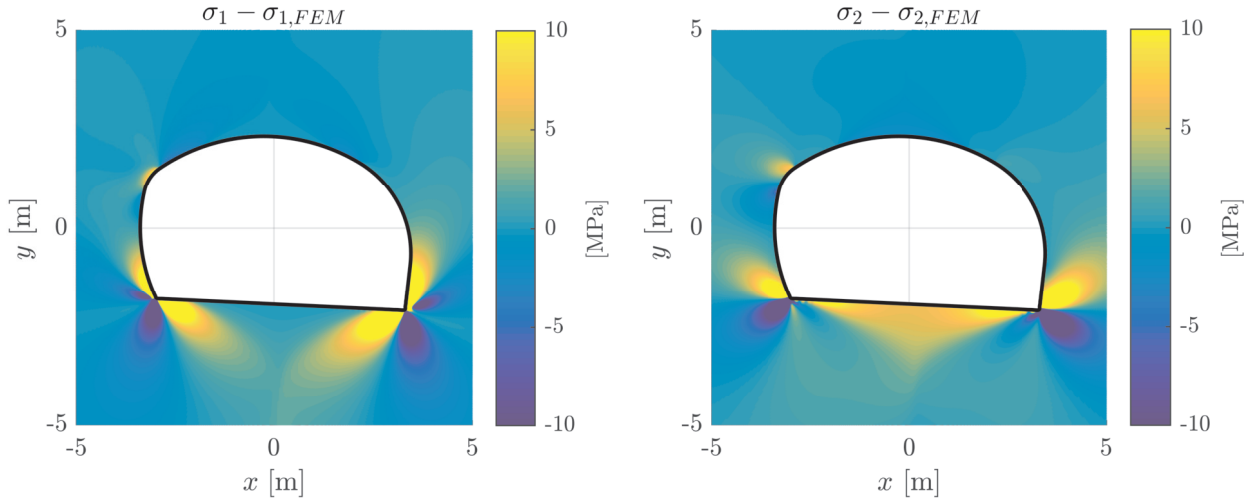

Figure 4.32: Again comparing the conformal mapping solution with "High" mapping settings to the FEM for principal stresses around a asymmetric tunnel. This time the mapped boundary instead of the sampled is used in the FEM model.

4.3 In-situ stress to borehole breakouts

Borehole breakout examples were created with the tool for different in-situ stresses and rock properties. The Hoek-Brown and Mohr-Coulomb failure criteria described in Section 2.3 were used to create breakouts both in the minor (shear failures) and major (tensile/shear failures) in-situ stress directions.

For each different failure mode and criterion 4 examples were created using varying in-situ stress ratios σ_h/σ_H, resulting in a total of 16 different tests. The in-situ stress ratios were selected to adequately match the chosen rock parameters in the failure criterion. Mapping settings for the tensile examples were set at 1024 samples and 100 series terms, in the shear examples settings were increased to 2048 samples and 150 series terms. During the shear examples symmetry was enforced in the mapping.

The discretization for the tensile examples was set at 256 radial nodes and 512 angular nodes. In the shear examples settings were increased to 512 radial nodes and 2048 angular nodes.

The breakouts in the tensile direction were possible to create without using any boundary smoothing, only a stress surface smoothing of 8 nodes radially and 16 angular nodes was used. However, when generating the shear breakouts boundary smoothing was essential for maintaining stability during iteration. To achieve stability when generating shear breakouts the boundary smoothing moving average was set at 128 boundary nodes and the stress surface smoothing set to 32 radial nodes and 64 nodes in the angular direction of the discretization.

Iteration was stopped and results saved either at the end of iteration 20 or if the failure area was below 1‰ of the initial borehole area.

4.3.1 Tensile breakouts

First, breakouts in the tensile direction were created using the Mohr-Coulomb criterion with the cohesion constant c set at 28 MPa, the friction angle ϕ set to 60° and the tensile limit σ_t set to -13.5 MPa, see

Figure 4.33. The minor in-situ stress was set at 10 MPa while increasing the major stress incrementally from 46 MPa up to 70 MPa.

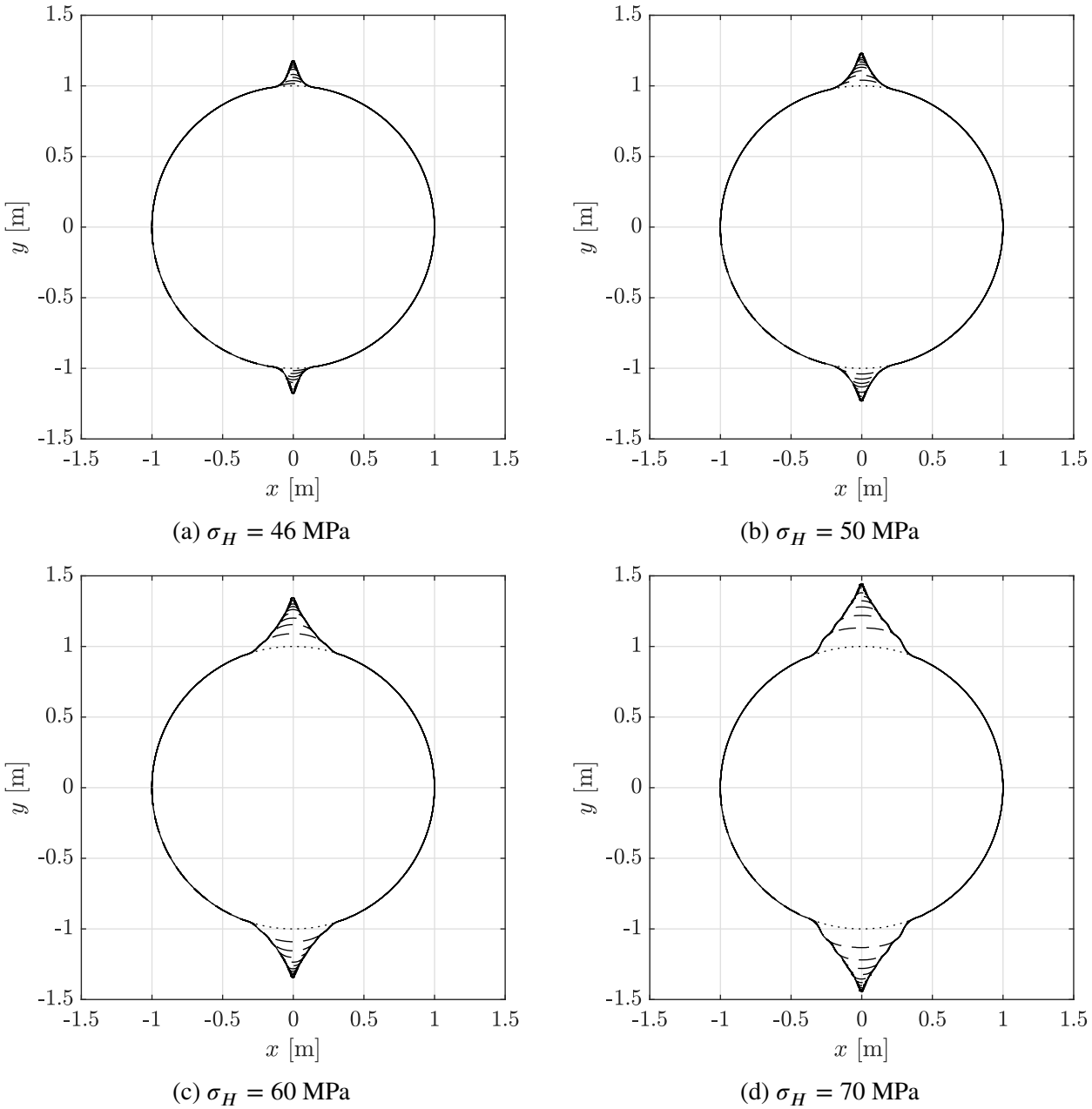

(a) $\sigma_H = 46$ MPa

(b) $\sigma_H = 50$ MPa

(c) $\sigma_H = 60$ MPa

(d) $\sigma_H = 70$ MPa

Figure 4.33: Breakout progressions with the Mohr-Coulomb failure criterion, using a varying major in-situ stress σ_H whilst holding the minor in-situ stress fixed at $\sigma_h = 10$ MPa.

Breakouts in the tensile direction were then created using the Hoek-Brown criterion with the material constant m_i set to 28.6, the uniaxial compressive strength σ_{ci} set to 227 and the tensile limit σ_t set to -13.5 MPa, see Figure 4.33. The minor in-situ stress was again fixed at 10 MPa while increasing the major stress incrementally from 39 MPa up to 60 MPa.

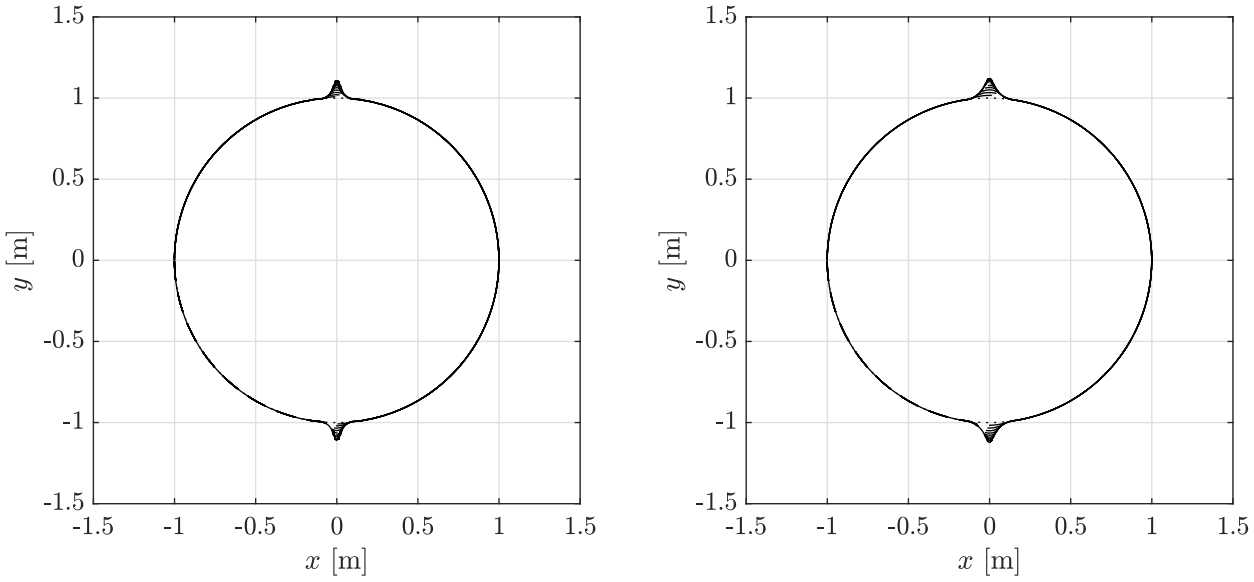

(a) $\sigma_H = 39$ MPa

(b) $\sigma_H = 40$ MPa

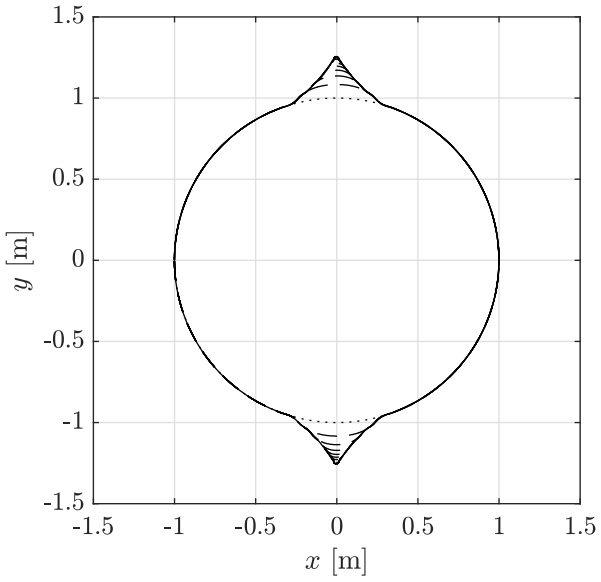

(c) $\sigma_H = 50$ MPa

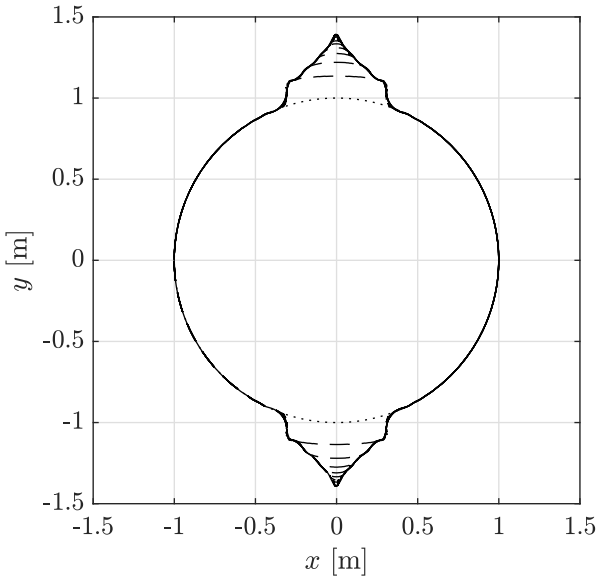

(d) $\sigma_H = 60$ MPa

Figure 4.34: Breakout progressions with the Hoek-Brown failure criterion, using a varying major in-situ stress σ_H whilst holding the minor in-situ stress fixed at $\sigma_h = 10$ MPa.

4.3.2 Shear breakouts

In the shear examples, beginning with the Mohr-Couloumb criterion, the cohesion constant c was set at 15 MPa and the friction angle ϕ set to 55°, see Figure 4.35. The minor in-situ stress was fixed at 20 MPa whilst the major was incrementally increased from 40 up to 60 MPa.

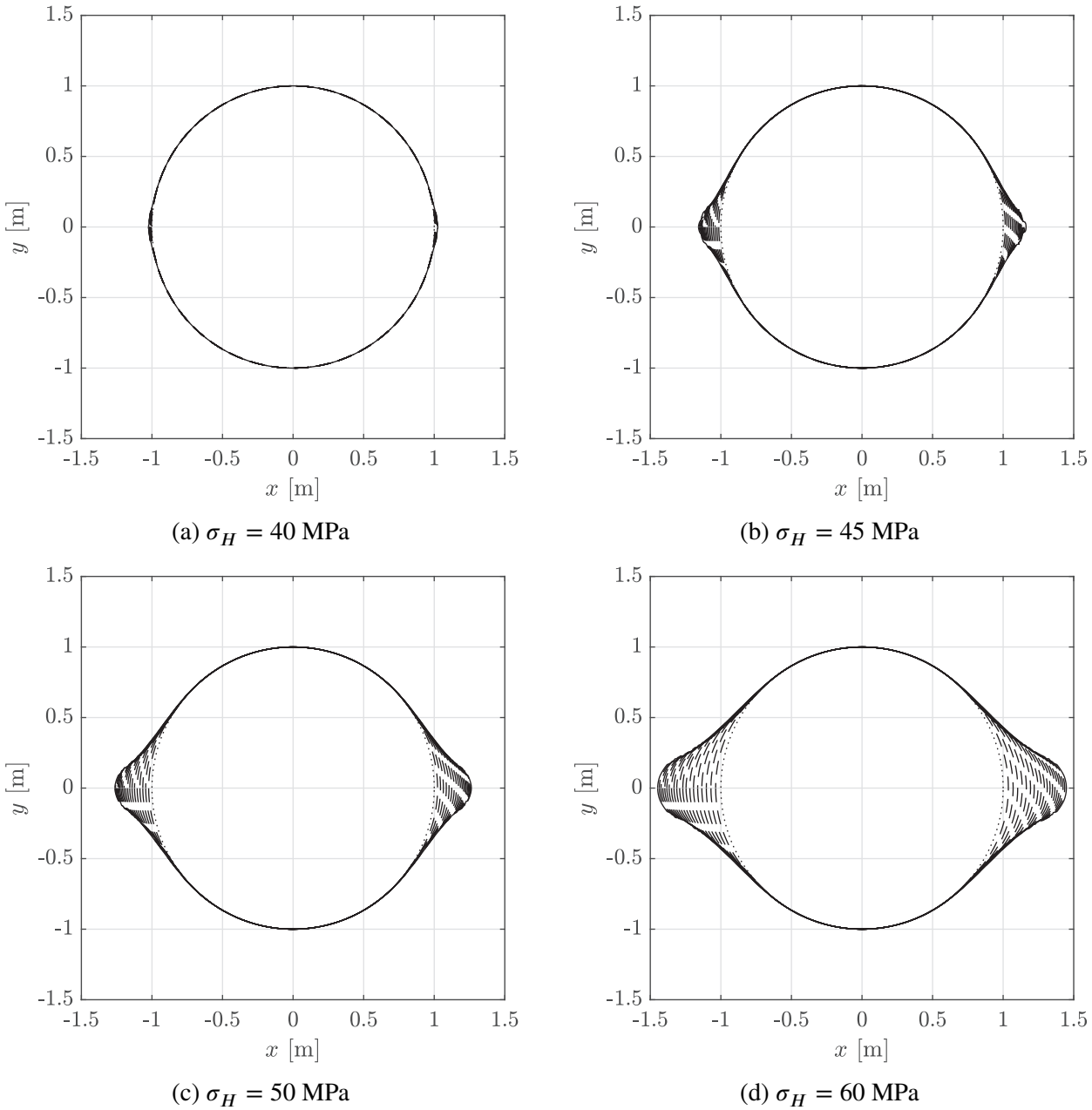

(a) $\sigma_H = 40$ MPa

(b) $\sigma_H = 45$ MPa

(c) $\sigma_H = 50$ MPa

(d) $\sigma_H = 60$ MPa

Figure 4.35: Breakout progressions with the Mohr-Coulomb failure criterion, using a varying major in-situ stress σ_H whilst holding the minor in-situ stress fixed at $\sigma_h = 20$ MPa.

With the Hoek-Brown criterion the material constant m_i was set to 30 and the uniaxial compressive strength σ_{ci} set to 90, see Figure 4.35. As in the previous example, the minor in-situ stress was fixed at

20 MPa whilst the major was incrementally increased from 40 up to 53 MPa.

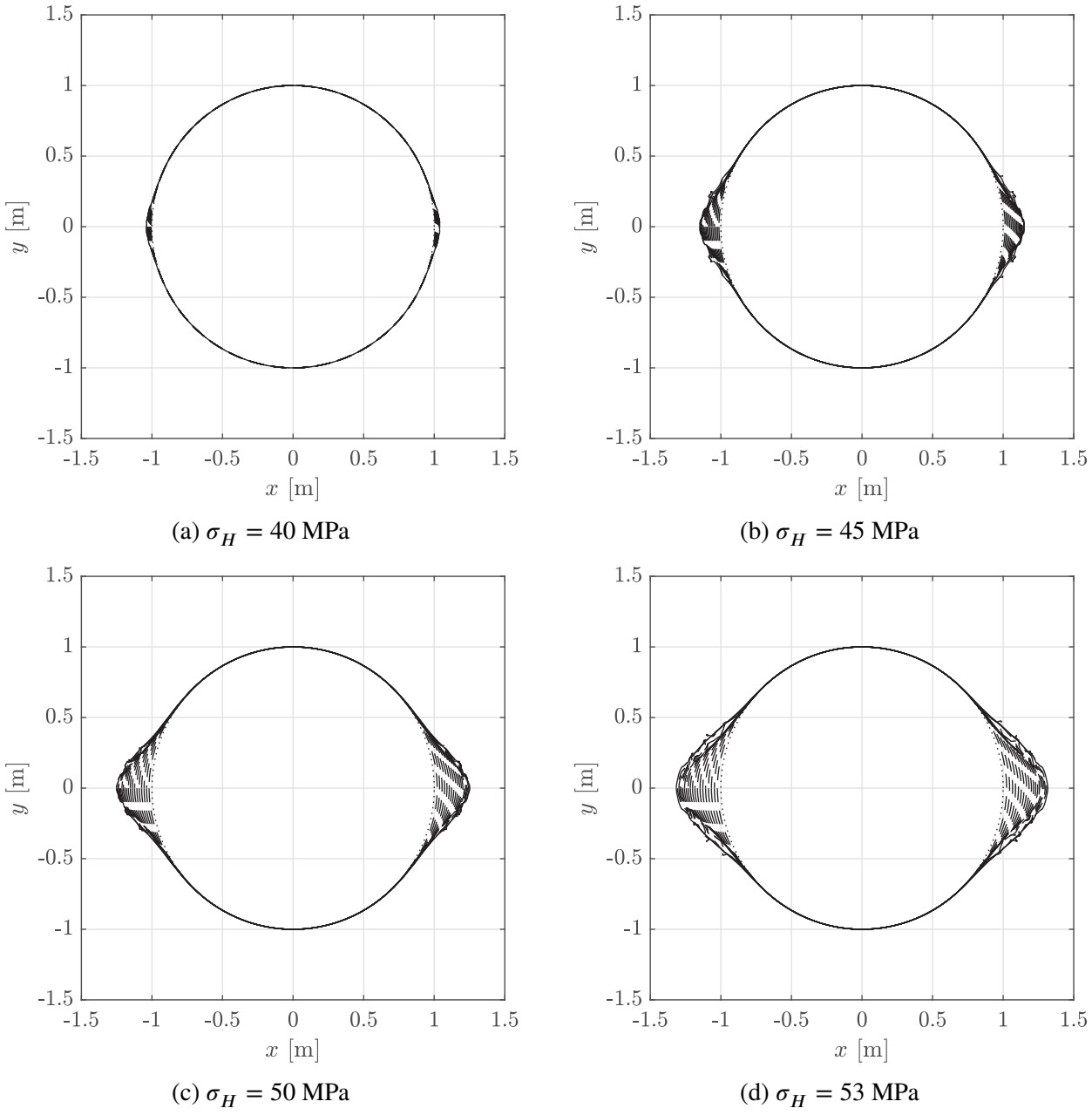

(a) $\sigma_H = 40$ MPa

(b) $\sigma_H = 45$ MPa

(c) $\sigma_H = 50$ MPa

(d) $\sigma_H = 53$ MPa

Figure 4.36: Breakout progressions with the Hoek-Brown failure criterion, using a varying major in-situ stress σ_H whilst holding the minor in-situ stress fixed at $\sigma_h = 20$ MPa.

4.3.3 Depth and width of example breakouts

For all breakout examples, the width of the initial breakout was measured in degrees and the depth of the breakout at the final iteration was measured. The results grouped in tensile and shear breakouts are shown below in Figures 4.37 to 4.40.

Tensile

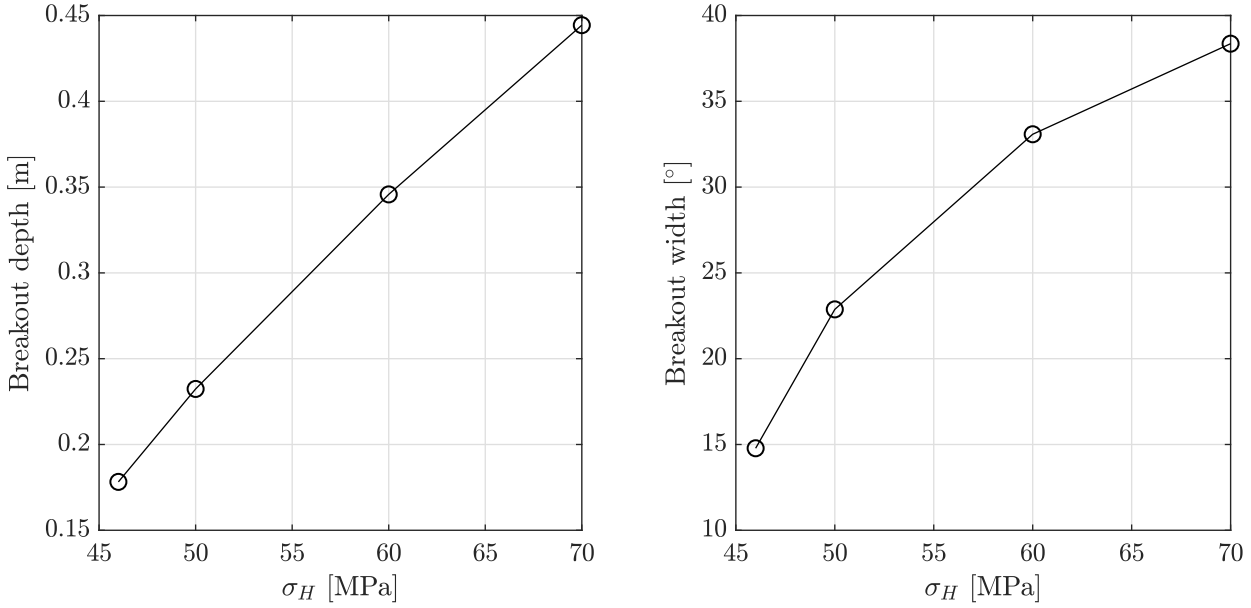

(a) Depth (b) Width

Figure 4.37: Tensile breakout depth (a) and width (b), using the Mohr-Coulomb failure criterion with tensile cutoff. The minor in-situ stress was fixed at $\sigma_h = 10$ MPa whilst varying the major in-situ stress σ_H.

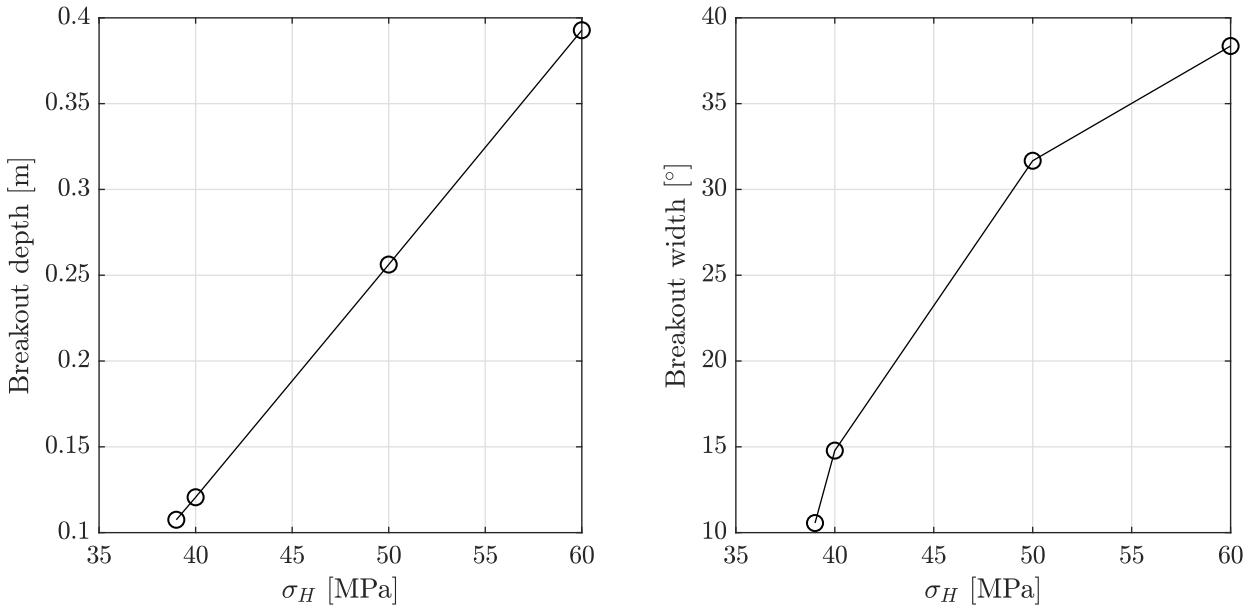

(a) Depth (b) Width

Figure 4.38: Tensile breakout depth (a) and width (b), using the Hoek-Brown failure criterion with tensile cutoff. The minor in-situ stress was fixed at $\sigma_h = 10$ MPa whilst varying the major in-situ stress σ_H.

Shear

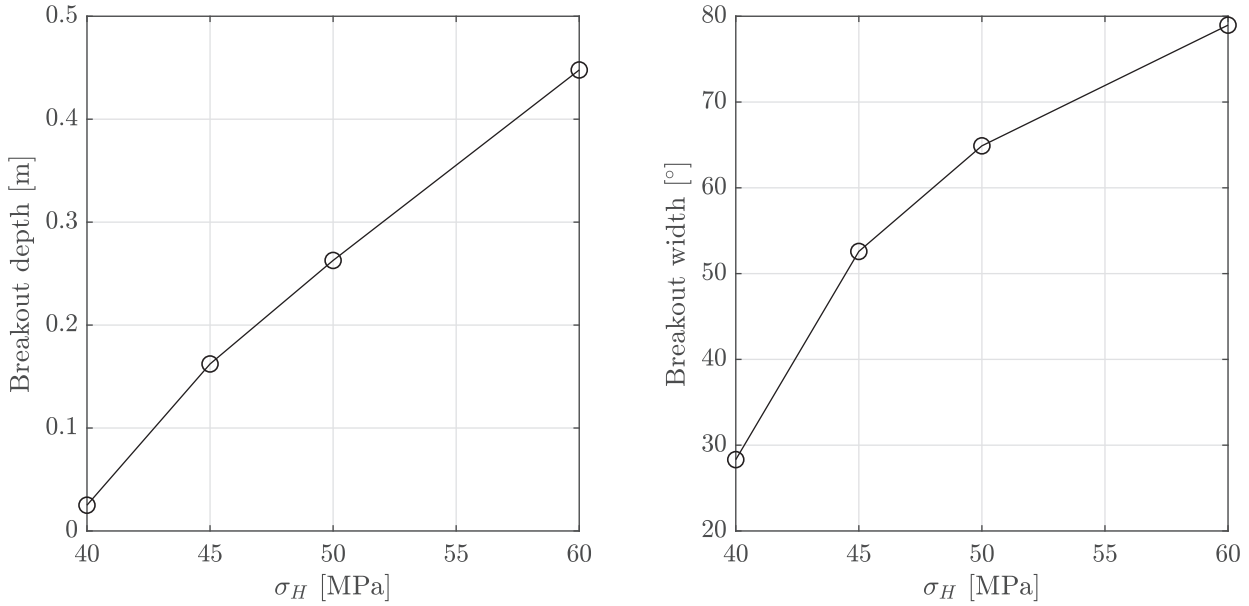

(a) Depth (b) Width

Figure 4.39: Shear breakout depth (a) and width (b), using the Mohr-Coulomb failure criterion. The minor in-situ stress was fixed at $\sigma_h = 20$ MPa whilst varying the major in-situ stress σ_H.

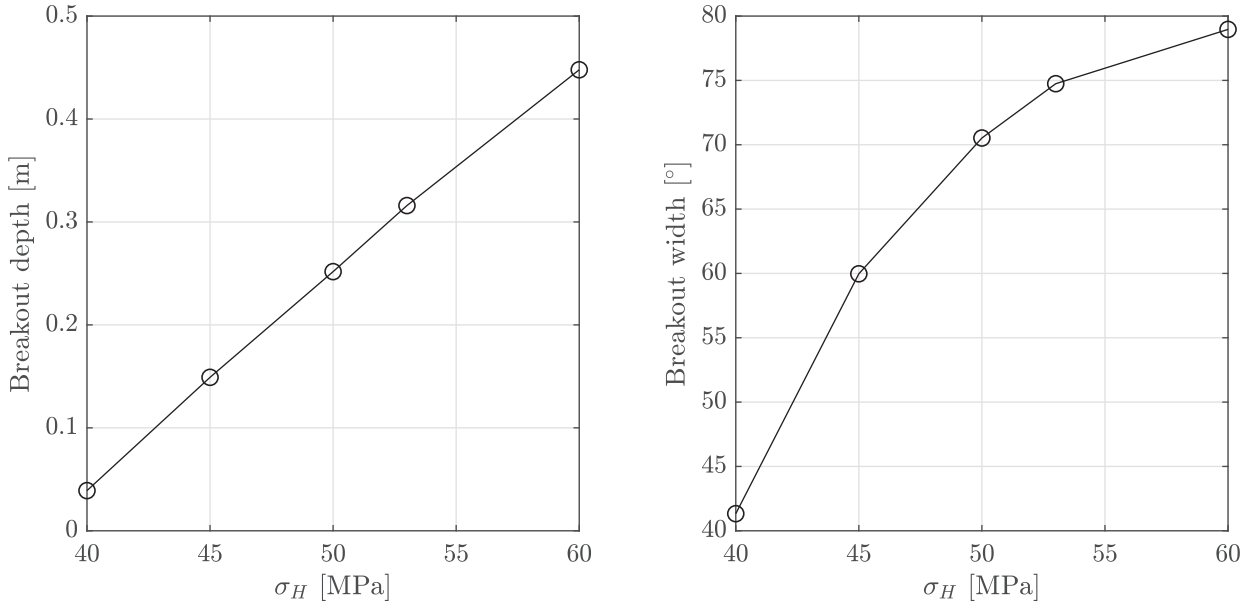

(a) Depth (b) Width

Figure 4.40: Shear breakout depth (a) and width (b), using the Hoek-Brown failure criterion. The minor in-situ stress was fixed at $\sigma_h = 20$ MPa whilst varying the major in-situ stress σ_H.

5 Discussion

This chapter will discuss the examples shown in the previous chapter, mainly observations of how the tool performed, but also the methods used for quantifying the tool performance will be covered. During this process a few possible drawbacks in the analysis and design will be covered, whilst a few ideas of how to improve the tool are suggested.

5.1 Defining a cavity geometry and mapping it

As a way to test the mapping performance several geometries, both symmetric and asymmetric, were designed and mapped. To quantify the performance the error between mapped and initial boundary was compared for different combinations of number of series terms and number of samples. However, there is a potential drawback in how this analysis was performed since a Fourier Series approximation using the same number of series coefficients as the mapping is baked into the mapping algorithm. Although the number of samples mainly is for the FFT, not separating the number of Fourier coefficients and number of mapping series terms means that the mapping review is somewhat biased toward showing how well the FFT performs. Error between the mapped and original geometry took the form of oscillations, where the amplitude of the oscillations concentrated at corners or non continuous changes in the original boundary. This behaviour is similar to how a Fourier series approximation of a function behaves with the Gibbs phenomena when approximating non-continuous functions. The similarity also questions how big of an impact not separating the number of Fourier coefficients and number of series terms for the mapping has. When interpreting the errors shown in Figure 4.15 and Figure 4.17 there is an indication that a balance is needed between number of series terms and number of samples. If a chosen number of samples is used there is not much point of increasing the number of mapping coefficients beyond a certain point and vice versa. This effect is however very small and is in the Figure 4.15 and Figure 4.17 only visible between the lowest used setting of 25 terms with 256 samples and the higher settings. However, a very small difference between the higher settings is also present if comparing them very closely.

The mapping time comparisons show a roughly linear relationship for increasing both samples and number of terms. There are a few dents in the curve, for example see Figure 4.16, this could be related to the computer running some background operations during the mapping calculations.

When mapping corners the error and boundary oscillations increase the sharper the corner. This is no surprise since the method used is stated to work for near circular geometries defined by a continuous curve, which a geometry with a corner is not.

The mapping functions provided were configured to force symmetry, when removing this enforcement mapping of asymmetric regions seemed to work out fine as the mapping examples show. However, when determining stresses around an asymmetric geometry and comparing it to FEM it was no longer certain that this was the case, which will be discussed in the next section regarding the evaluation of secondary stresses.

One drawback of using this mapping method is that a more complex boundary could shadow itself during sampling since there is only one sampled boundary radius allowed per sampled angle. As with the larger error due to corners this is no surprise and is generally not a problem for boreholes with breakouts and most tunnel geometries. For the case of evaluating boundaries that shadow themselves (multiple boundary radii at one sample angle), use of an alternate mapping method could be investigated.

5.2 Evaluating secondary stresses

During comparison to the Kirsch solution around a circular hole, the tool evaluated stresses correctly with very small errors, however, the FEM comparison of the asymmetric tunnel geometry displayed large errors surrounding the floor corners. Corners are problematic with this method, although in theory, evaluating asymmetric regions should be fine. Since the mapping examples show that at least the boundary maps correctly, this could indicate that the problem lies in the evaluation of the stress function power series in the provided code. An additional FEM comparison of a symmetric non-circular region would be suitable to verify that the tool evaluates stresses correctly. It is certain that the base code works for symmetric geometries since Gerolymatou (2019) showed this by comparing stresses surrounding a crack to those produced by an analytic solution. If the provided code that determines stress function series constants was adapted, the tool could be used on more general asymmetric regions. However, it is worth mentioning that the main mission of the tool is to evaluate symmetric geometries such as boreholes with breakouts.

In the example of stress smoothing shown in Figure 3.11, it is also visible how boundary oscillations can effect the secondary stresses. Since a lot of oscillations occur near corners, larger errors in stresses and stress spikes are bound to occur. The boundary oscillations are an effect of the mapping and are not realistic, meaning that the fluctuating stresses near the boundary are not realistic either. Another unrealistic finding are the stress spikes that occur at corners. A peak in stress is to be expected, but stresses spiked extremely in a way that in reality would fracture or yield the material, thus relieving the stress peak.

5.3 Simulating breakouts and the use of smoothing

Both tensile and shear borehole breakouts were produced with the tool. Boundary and subsequent stress oscillations made it necessary to use smoothing for stabilising the otherwise increasingly unstable geometry throughout iteration. If only one iteration is run smoothing is not needed, but since oscillations in the boundary and stress surface propagate and increase for every iteration some sort of measure is required. The boundary smoothing tries to mitigate effects of the mapping. Stress smoothing is a means of filtering the stresses to make them more realistic without spikes and fluctuations near the oscillating boundary. Both methods might distort and produce unrealistic results if set too high. One possible way to limit the influence of unrealistic smoothing operations could be to incorporate some logic that scales the effect of smoothing depending on how much the boundary and stress surface oscillates, or set its influence to depend on how many iterations into the breakout simulation the tool has run.

The current implementation of boundary smoothing in this tool filters the entire 360 degrees of the boundary. Due to this, distortion of the geometry slowly occurs throughout iteration as a side effect of the smoothing. The moving average could be constructed so that it only filters the angular intervals of the geometry that has experienced failure, and reconstruct the intervals of the boundary without failure from the previous iteration. An implementation such as this would resolve some of the boundary distortion that occurs due to smoothing. In the breakout examples shown in this thesis the maximum number of iterations was set to 20. This setting was a trade-off between how much smoothing to use that could potentially distort the results and how many iterations could be run, an improved non-constant smoothing configuration could be helpful in making this trade-off.

There are several notes to make on the stress smoothing that was implemented in this tool. It was implemented quickly as a test to see if it would help stabilizing the process of simulating borehole breakouts, which it did. In hindsight however, there is room for much improvement in its design. The stress smoothing as it is implemented now does not smooth stresses over an area, just over columns and rows in the matrices that define the secondary stresses. The loop that does the moving average filter of rows and columns also does not use the original unfiltered stresses while looping through the nodes, meaning that the smoothing uses stress data that is continuously altered during looping. Another error related to not smoothing over an area, is that the radial nodes are not spaced linearly. Even though these errors were present, the stress smoothing did help in stabilizing the breakout simulation and deal with unrealistic stress peaks near corners.

Although smoothing was used there were in some cases limited stress fluctuations at the boundary that could cause small failures of a only few nodes. As a fail safe for making sure that such small failures would not contribute to the boundary deteriorating and thus producing more boundary oscillations on the next iteration, a limit on how few nodes can fail in a region was included. This was mainly an effect of the mapping distorting the boundary, but in other cases where small failures would occur it could be argued that, a material such as a rock can suffer from small fractures without it necessarily falling apart.

Up until the breakout examples symmetry was not enforced during mapping, but when performing the breakout simulations it was activated since it seemed to increase the stability throughout iteration thus allowing for less smoothing. Therefore it is suggested to enforce symmetry if the geometry being analysed is symmetric.

The failure criterion greatly influences how the borehole breakouts are simulated. Generally, there are many aspects in the failure modelling which were not taken into account in the tool. The failure criteria used are modelled for brittle failures, if the material and in-situ stresses would make the rock yield in the brittle-ductile region or behave in a completely ductile fashion, an entirely different failure modelling would be required. Therefore it is important to identify that the failure criterion properly models the rock not only in a lab but also in the in-situ conditions. For example, the tensile Hoek-Brown breakout examples produced were modelled with in-situ stresses and a failure criterion relatively close to the one described by Martin, Read, and Martino (1997) of the Underground Research Laboratory (URL) test tunnel where brittle spalling was observed. However, in the URL breakouts were produced in the shear direction whilst the tool with similar parameters produced breakouts in the tensile direction. One reason for this is that there are other influences in play in the real world such as gravity, scale effects, excavation induced damages and the excavation not exactly matching the theoretical design. Although gravity should not have a big effect on the breakouts in a vertical borehole or a hole with an internal pressure from mud weight, it might have an influence in a horizontally aligned unsupported borehole or tunnel, a factor that was not considered in the tool. Using the URL as a reference, Cai (2013) showed that irregularities in the excavated boundary could cause concentrations of stress that initiate brittle failure. In the tool the effects of boundary irregularities are not modelled which is contributing to the error. Zhao, Cai, and Cai (2010, 4) investigated with a cohesion weakening and frictional strengthening rock model how rock mass dilation could affect brittle failure in conjunction to tunnel deformation at the URL. The model they used could capture the depth of the brittle failure at the URL that many other conventional rock models could not. Therefore, it is not surprising that there are many differences in the results produced by the tool built during this thesis project and what has been observed in the URL.

When simulating the tensile breakouts, the breakouts rapidly converged with only a few iterations, in contrast, the shear breakouts failed in much smaller increments continuing all the way up to the maximum

iterations limit set at 20. Possibly the shear breakout simulations would require many iterations more before reaching a stable geometry. The limit was chosen as a trade-off for how much smoothing to use, if doing a more clever smoothing implementation as previously mentioned, it should be possible to reach much higher number of iterations without letting the smoothing having a too big influence on the results.

5.4 Designing an inverse model for finding in-situ stress from measured breakouts

Since there are reliable methods to use for determining the minor principal in-situ stress such as hydraulic fracturing and methods to model the rock strength, only the major principal in-situ stress is unknown if constructing an inverse model of the tool. Figure 4.40 shows curves with depth and width for a number of borehole breakouts simulated with a fixed minor principal in-situ stress and a variable major. By matching an inverse function to curves produced by simulating several borehole breakouts the major principal in-situ stress could potentially be obtained from the inverse functions.

One drawback is that all limitations and errors in the breakout simulation translate to the inverse function. For example, due to the failure criterion having a big impact on how the breakouts are generated, a failure criterion not fitted for the in-situ situation also has an impact on any inverse functions created from breakout simulations.

6 Conclusion

The purpose of the thesis was to construct a simple to use computational tool based on conformal mapping that could evaluate secondary stress and simulate borehole breakouts. To achieve this goal a tool was built in MATLAB that could determine stresses around arbitrary symmetric cavity geometries and control them for stability with the Mohr-Coulomb or Hoek-Brown failure criterion. Potential progressive failures around a geometry could be evaluated in the tool by redefining a new boundary after failure, which subsequently was re-evaluated for additional failure. By repeating this process borehole breakouts could be simulated. Another goal was to use simulated breakouts as a reference for determining in-situ stresses around measured borehole breakouts. As an example on how simulated breakouts could be used to create reference tables, width and depth of a few simulated breakouts was presented. However, the task of implementing an inverse model in the tool to calculate major principal in-situ stress from measured borehole breakouts was refrained from.

Review of the mapping was performed by mapping different geometries and analysing residuals between the mapped and original geometry, showing how the number of samples and series coefficients affected precision. Although it can be discussed how much of the review reflects upon the FFT and the actual mapping, there are still some conclusions that can be drawn from the mapping review: sharp corners induce oscillations; there is no reason to use a very high number of series terms if there are too few samples and vice versa; and mapping time has an almost linear relationship to how many samples and series terms are used.

The tool was tested by determining stresses around a circular hole and a tunnel geometry, the circular hole was compared to Kirsch's solution and the tunnel to a FEM solution. Currently the tool works well for evaluating stresses around symmetric regions with few corners such as boreholes with breakouts, but the base functions that calculate the power series for mapping and stress evaluation are not adapted for non-symmetric regions as shown in the FEM comparison. However, the theory supports evaluation of non-symmetric geometries which means that, if the base functions handling the power series for mapping and stress functions are configured for working with non-symmetric regions, the tool is easily updated to also correctly analyze arbitrary regions.

Simulation of borehole breakouts with the tool is possible due to boundary smoothing dealing with unrealistic boundary oscillations and stress surface smoothing taking care of unrealistic stress spikes and stress oscillation artefacts from boundary oscillations. Another aspect of breakout simulation is that modelling of rock with a failure criterion is difficult to get absolutely right, and since the failure criterion is essential to the breakout simulation progress, a good and suitable failure criterion is an extremely important factor in realistic breakout simulation.

If the minor in-situ stress is determined with a method such as hydraulic fracturing and if the rock can be modelled well enough with a failure criterion, the major in-situ stress could potentially be found by simulating a few different borehole breakouts. Simulated breakout depth and width could be fitted to functions of the major in-situ stress in the simulations, the functions of major in-situ stress would be based on the minor in-situ stress and the rock failure criterion. A real world measured breakout could potentially be matched to these functions, thus returning the major in-situ stress.

Excepting the addition of an inverse algorithm to determine the maximum in-situ stress from measured breakouts, there are still many possible improvements to be made if the tool is to be developed further. Adapting the base functions for use on non-symmetric regions would be beneficial for applying the

tool to tunnel geometries. Some of the limitations stated at the introduction could be addressed, time dependency, thermal stresses, rock anisotropy and drilling/excavation induced damages to the rock. Additionally to these limitations also gravity, which has an effect on horizontally aligned cavities, could be included for better results when analysing tunnels. A method of handling in-situ shear is at present not included, although this could be fixed by just rotating the geometry so that it is aligned with principal in-situ stresses. The smoothing implementations could be developed further to minimize smoothing induced errors.

References

Aadnøy, B. S. & Looyeh, R. (2010). *Petroleum rock mechanics: Drilling operations and well design*. Elsevier. (Cited on pages 2, 6, 7, 10, 13, 15–17).

Airy, G. (1862). On the strains in the interior of beams. *Philosophical transactions of the Royal society of London : giving some accompt of the present undertakings, studies, and labours of the ingenious in many considerable parts of the world. 153 (1863)*, 49–71. (Cited on pages 10, 11).

Bourke, P. (1988). Calculating the area and centroid of a polygon. Retrieved August 25, 2019, from https://www.seas.upenn.edu/~sys502/extra_materials/Polygon%20Area%20and%20Centroid.pdf. (Cited on page 32)

Brudy, M., Zoback, M. D., Fuchs, K., Rummel, F., & Baumgärtner, J. (1997). Estimation of the complete stress tensor to 8 km depth in the KTB scientific drill holes: Implications for crustal strength. *Journal of geophysical research*, *102*(B8), 18, 453–18, 475. (Cited on pages 1, 6, 23).

Caenn, R., Darley, H. C. H., & Gray, G. R. (2017). *Composition and properties of drilling and completion fluids* (7th edition). Elsevier. (Cited on pages 1, 13–15).

Cai, M. (2013). Realistic simulation of progressive brittle rock failure near excavation boundary. *Constitutive Modeling of Geomaterials*, 303–312. (Cited on page 77).

Coulomb, C. (1776). *Essai sur une application des règles de maximis et minimis à quelques problèmes de statique, relatifs à l'architecture*. De l'Imprimerie Royale. (Cited on page 15).

Cuss, R. J., Rutter, E. H., & Holloway, R. F. (2003). Experimental observations of the mechanics of borehole failure in porous sandstone. *International Journal of Rock Mechanics and Mining Sciences*, *40*, 747–761. (Cited on page 19).

Erlström, M., Mellqvist, C., Schwarz, G., Gustafsson, M., & Dahlqvist, P. (2016). *Geologisk information för geoenergianläggningar – en översikt* (Number 2016:16). Sveriges geologiska undersökning. (Cited on page 1).

Ewy, R. T. & Cook, N. G. W. (1990). Deformation and fracture around cylindrical openings in rock—ii. initiation, growth and interaction of fractures. *International Journal of Rock Mechanics and Mining Sciences and Geomechanics Abstracts*, *27*, 409–427. (Cited on pages 6, 19, 22).

Ewy, R. T., Kemeny, J. M., Zheng, Z., & Cook, N. G. W. (1987). Generation and analysis of stable excavation shapes under high rock stresses. *Proc. Sixth Int. Congr. on Rock Mech., Montreal,* 875–881. (Cited on page 19).

Exadaktylos, G. E. & Stavropoulou, M. C. (2002). A closed-form elastic solution for stresses and displacements around tunnels. *International Journal of Rock Mechanics and Mining Sciences*, *39*, 905–916. (Cited on page 2).

Fornberg, B. (1980). A numerical method for conformal mappings. *SIAM Journal on Scientific and Statistical Computing*, *1*(3). (Cited on page 2).

Gerolymatou, E. (2019). A novel tool for simulating brittle borehole breakouts. *Computers and Geotechnics*, *107*, 80–88. (Cited on pages i, 3, 31, 36, 39, 76).

Gough, D. I. & Bell, J. S. (1981). Stress orientations from oil-well fractures in alberta and texas. *Canadian Journal of Earth Sciences*, *18*, 638–645. (Cited on pages 1, 19).

Goursat, E. (1898). Sur l'equation $\Delta^2 u = 0$. *Bulletin Soc. Math. France*, *26*, 236–237. (Cited on page 11).

Haimson, B. (2007). Micromechanisms of borehole instability leading to breakouts in rocks. *International Journal of Rock Mechanics and Mining Sciences*, *44*, 157–173. (Cited on pages 19, 20, 52).

Haimson, B. & Lee, H. (2004). Borehole breakouts and compaction bands in two high-porosity sandstones. *International Journal of Rock Mechanics and Mining Sciences*, *41*, 287–301. (Cited on pages 20, 22).

Haimson, B. & Kovacich, J. (2002). Borehole instability in high-porosity berea sandstone and factors affecting dimensions and shape of fracture-like breakouts. *Engineering Geology*, *69*, 219–231. (Cited on pages 20, 21).

Hoek, E. (n.d.). *Practical rock engineering*. (Cited on pages 8, 18).

Hoek, E. & Martin, C. D. (2014). Fracture initiation and propagation in intact rock – a review. *Journal of Rock Mechanics and Geotechnical Engineering*, *6*, 287–300. (Cited on pages 17, 18).

Holtz, R. D. & Kovacs, W. D. (1981). *An introduction to geotechnical engineering*. Prentice Hall. (Cited on page 15).

Kantorovich, L. V. (1933). On some methods of constructing a function effecting a conformal transformation. *Bulletin of the Academy of Sciences of the USSR*, *7*, 229–235. (Cited on page 29).

Kirsch, E. (1898). Die theorie der elastizität und die bedürfnisse der festigkeitslehre. *Zeitschrift des Vereines deutscher Ingenieure*, *42*, 797–807. (Cited on pages i, 2, 3, 10, 23).

Knutsson, O. (2017). Så fungerar sveriges största bergvärmeanläggning. *VVS-Forum*. Retrieved November 9, 2018, from https://www.vvsforum.se/nyheter/2017/mars/sa-fungerar-sveriges-storsta-bergvarmeanlaggning/. (Cited on page 1)

Kythe, P. K. (1998). *Computational conformal mapping*. Birkhäuser, Boston, MA. (Cited on page 2).

Lake, L. W. & Mitchell, R. F. (2006). *Petroleum engineering handbook : Drilling engineering*. Society of Petroleum Engineers. (Cited on page 2).

Lee, M. & Haimson, B. (1993). Laboratory study of borehole breakouts in lac du bonnet granite: A case of extensile failure mechanism. *International Journal of Rock Mechanics and Mining Sciences and Geomechanics Abstracts*, *30*(7), 1039–1045. (Cited on pages 19, 20, 22).

Liu, Z. & Meng, Y. (2015). Key technologies of drilling process with raise boring method. *Journal of Rock Mechanics and Geotechnical Engineering*, *7*, 385–394. (Cited on page 1).

Maleki, S., Moradzadeh, A., Riabi, R. G., & Sadaghzadeh, F. (2014). Comparison of several different methods of in situ stress determination. *International Journal of Rock Mechanics and Mining Sciences*, *71*, 395–404. (Cited on page 6).

Marshak, S. (2011). *Earth: Portrait of a planet* (Fourth). W. W. Norton and Company. (Cited on pages 14, 15).

Martin, C. D., Read, R. S., & Martino, J. B. (1997). Observations of brittle failure around a circular test tunnel. *International Journal of Rock Mechanics and Mining Sciences*, *34*, 1065–1073. (Cited on page 77).

MathWorks®. (2019). Partial differential equation toolbox. Retrieved August 21, 2019, from https://se.mathworks.com/help/pde/index.html. (Cited on page 63)

Meier, T., Rybacki, E., Reinicke, ., & Dresen, G. (2013). Influence of borehole diameter on the formation of borehole breakouts in black shale. *International Journal of Rock Mechanics and Mining Sciences*, *62*, 74–85. (Cited on pages 20, 21).

Meng, F. & Fuh, G.-F. (2013). Wellbore stability evaluation guideline for reducing non-productive time. *International Petroleum Technology Conference*. doi:10.2523/IPTC-16567-MS. (Cited on page 1)

Mohr, C. O. (1900). Welche umstände bedingen die elastizitätsgrenze und den bruch eines materials. *Zeitschrift des Vereins Deutscher Ingenieure*, *46*, 1572–1577. (Cited on page 15).

Muskhelishvili, N. I. (1977). *Some basic problems of the mathematical theory of elasticity*. Springer Netherlands, Dordrecht. (Cited on page 25).
Odén, A. (2013). *Förutsättningar för borrning av och deponering i djupa borrhål*. Svensk Kärnbränslehantering AB. (Cited on page 1).
Paul, B. (1961). A modification of the coulomb-mohr theory of fracture. *Journal of Applied Mechanics*, *28*, 259–268. (Cited on page 16).
Prensky, S. (2015). What's new in well logging and formation evaluation. *World Oil*, *236*(3). (Cited on page 20).
Ren, Y., Wang, Y., Wang, M., Wu, S., & Wei, B. (2014). A measuring system for well logging attitude and a method of sensor calibration. *Sensors*, *14*, 9256–9270. (Cited on page 22).
Sampson, D. (2019). GUI Layout Toolbox. *MATLAB Central File Exchange*. Retrieved August 25, 2019, from https://www.mathworks.com/matlabcentral/fileexchange/47982-gui-layout-toolbox. (Cited on page 33)
Schinzinger, R. & Laura, P. A. A. (1991). *Conformal mapping: Methods and applications*. Elsevier. (Cited on pages 2, 11, 24, 29).
Stüwe, K. (2011). *Geodynamics of the lithosphere* (Second). Springer. (Cited on page 15).
Sun, C. T. & Jin, Z.-H. (2012). *Fracture mechanics*. Elsevier. (Cited on page 2).
U.S. National Committee for Rock Mechanics, Geotechnical Board, and National Research Council. (1993). *Stability, failure, and measurements of boreholes and other circular openings*. National Academic Press. (Cited on pages 19, 22).
Verruijt, A. (1998). Deformations of an elastic half plane with a circular cavity. *International Journal of Solids and Structures*, *35*, 2795–2804. (Cited on page 2).
Waltham, T. (2009). *Foundations of engineering geology* (Third). Spon Press. (Cited on pages 13, 16).
Wegmann, R. (1989). Conformal mapping by the method of alternating projections. *Numerische Mathematik*, *56*, 291–307. (Cited on page 2).
Zhao, X., Cai, M., & Cai, M. (2010). Considerations of rock dilation on modeling failure and deformation of hard rocks—a case study of the mine-by test tunnel in canada. *Journal of Rock Mechanics and Geotechnical Engineering*, *2*, 338–349. (Cited on page 77).
Zhou, H., Kong, G., & Liu, H. (2016). Pressure-controlled elliptical cavity expansion under anisotropic initial stress: Elastic solution and its application. *Science China Technological Sciences. 59*, 1100–1119. (Cited on page 2).
Zoback, M. D., Barton, C. A., Brudy, M., Castillo, D. A., Finkbeiner, T., Grollimund, B. R., … Wiprut, D. J. (2003). Determination of stress orientation and magnitude in deep wells. *International Journal of Rock Mechanics and Mining Sciences*, *40*, 1049–1076. (Cited on pages 2, 6, 19, 20, 22).
Zoback, M. D. (2007). *Reservoir geomechanics*. Cambridge University Press. (Cited on pages 22, 23).

A Complex numbers

In this Appendix a brief overview on complex numbers and some of their useful properties are presented. A complex number z is a representation in 2D as shown in Figure A.1.

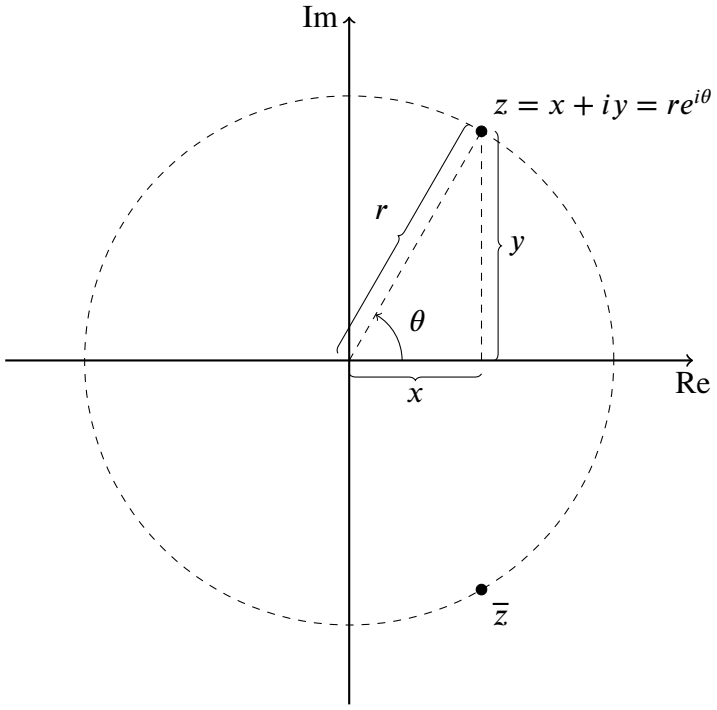

Figure A.1: Representation of complex number in 2D.

$$z = x + iy \tag{A.1}$$

The x and y are real numbers and $i = \sqrt{-1}$. If either the real or imaginary part is referred to the notation in Equation (A.2) can be used

$$\begin{aligned} \mathfrak{R}[z] &= \mathrm{Re}(z) = x \\ \mathfrak{I}[z] &= \mathrm{Im}(z) = y \end{aligned} \tag{A.2}$$

The conjugate of z is denoted $\overline{z}$ and simply means

$$\overline{z} = x - iy \tag{A.3}$$

The modulus or norm of z is denoted $|z|$ and can be calculated as

$$|z| = \sqrt{z\overline{z}} = \sqrt{x^2 + y^2} \tag{A.4}$$

The argument of z is the angle θ in the polar form. Thus it can be computed as

$$\arg(z) = \theta = \arctan\frac{y}{x} \tag{A.5}$$

Both z and $\overline{z}$ can be described in polar and exponential form. In the case below the modulus $|z|$ will simply be equal to r.

$$z = r(\cos\theta + i\sin\theta) = re^{i\theta} \tag{A.6}$$

$$\overline{z} = r(\cos\theta - i\sin\theta) = re^{-i\theta} \tag{A.7}$$

Complex exponents can be written as

$$z^n = r^n(\cos(n\theta) + isin(n\theta) = r^n e^{-in\theta} \tag{A.8}$$